
Adsorptive properties (CO, CO₂, H₂O) of clean
and Au-covered rutile(011)-(2x1) films prepared
by epitaxy on Re(10 $\bar{1}$ 0) surfaces

Dissertation zur Erlangung des akademischen Grades des
Doktors der Naturwissenschaften (Dr. rer. nat.)

eingereicht im Fachbereich Biologie, Chemie, Pharmazie
der Freien Universität Berlin

vorgelegt von

Wilhelmine Kudernatsch

aus Berlin

Mai 2009

-
1. Gutachter: Prof. Dr. K. Christmann
 2. Gutachter: Prof. Dr. E. Illenberger

Disputation am: 19.06.2009

Die vorliegende Arbeit wurde im Zeitraum Juli 2005 bis Mai 2009 am Institut für Chemie und Biochemie – Physikalische und Theoretische Chemie – der Freien Universität Berlin unter der Leitung von Prof. Dr. K. Christmann angefertigt.

Abbreviations

AES	Auger electron spectroscopy
ARUPS	angle resolved ultraviolet photoelectron spectroscopy
DFT	density functional theory
$\Delta\Phi$	work function change
HREELS	high-resolution electron energy loss spectroscopy
HREM	high-resolution electron microscopy
IMFP	inelastic mean free path
L	Langmuir
LEED	low energy electron diffraction
ML	monolayer
MLE	monolayer equivalent(s)
PID	proportional-integral-derivative
STM	scanning tunneling microscope
SXRD	surface x-ray diffraction
TPD	temperature programmed desorption
TD	thermal desorption
UHV	ultra-high vacuum
UPS	ultraviolet photoelectron spectroscopy

Contents

1	Introduction	1
2	Physical and chemical background	5
2.1	Motivation	5
2.1.1	The pressure and materials gap in heterogeneous catalysis	5
2.1.2	Low-temperature CO oxidation	6
2.2	Two-dimensional systems: thin film growth	10
2.2.1	Epitaxy	10
2.2.2	Thermodynamics of thin film growth	12
2.2.3	Thin film growth from a kinetic point of view	13
2.3	Materials and their chemistry	15
2.3.1	Rhenium (Re)	15
2.3.2	The peculiar Re(10 $\bar{1}$ 0) orientation	15
2.3.3	Titanium (Ti)	16
2.3.4	Titanium oxides, chemistry and crystallography	17
2.3.5	Gold (Au)	24
3	The experiments and their set-up	27
3.1	The ultra-high vacuum system	27
3.1.1	The sample holder	29

3.1.2	The titanium evaporator	30
3.1.3	The gold evaporator	31
3.2	Structure determination by low-energy electron diffraction (LEED)	33
3.2.1	Surface structures	33
3.2.2	The origin of the diffraction pattern	34
3.2.3	The reciprocal lattice	35
3.2.4	The LEED-experiment	37
3.3	Scanning tunneling microscopy (STM)	37
3.3.1	STM: theoretical background	37
3.3.2	The STM set-up	39
3.4	Auger electron spectroscopy (AES)	40
3.4.1	The Auger process	40
3.4.2	The intensity of the Auger signal	41
3.4.3	The cylindrical mirror analyzer (CMA)	42
3.5	Temperature-programmed desorption (TPD)	43
3.5.1	The data evaluation	43
3.5.2	The experimental set-up	45
3.6	Adsorbate-induced work function change ($\Delta\Phi$)	49
3.6.1	$\Delta\Phi$ – theoretical background	49
3.6.2	The self-compensating Kelvin probe method	50
4	Structural aspects	53
4.1	The rhenium($10\bar{1}0$) substrate	53
4.2	Preparation and characterization of the oxygen (1×3)- $2O$ super- structure	54
4.3	The ‘art’ of growing $TiO_2(011)$ - (2×1) films; structure and morphol- ogy	58
4.4	Preparation of partially Au-covered rutile $TiO_2(011)$ - (2×1) films .	65

5	Chemical reactivity of rutile(011)-(2x1) films	69
5.1	CO interaction with TiO ₂ (011)-(2x1)	70
5.1.1	TPD of CO from TiO ₂ (011)-(2x1)	71
5.1.2	Influence of the surface roughness on the CO adsorption behaviour	79
5.1.3	The influence of the thermal treatment of the TiO ₂ films on the CO adsorption	81
5.1.4	CO adsorption on rutile(011)-(2x1) films pre-covered with H ₂ O	86
5.1.5	CO-induced work function change ($\Delta\Phi$) on rutile(011)-(2x1)	88
5.1.6	LEED observations	89
5.1.7	Conclusions – CO interaction with epitactic rutile(011)- (2x1) films	89
5.2	Water interaction with TiO ₂ (011)-(2x1)	93
5.2.1	TPD of H ₂ O from TiO ₂ (011)-(2x1)	93
5.2.2	LEED – H ₂ O / TiO ₂ (011)-(2x1)	101
5.2.3	Water-induced work function change on rutile(011)-(2x1) .	104
5.2.4	Conclusions – H ₂ O interaction with epitactic rutile(011)-(2x1) films . . .	108
5.3	Interaction of carbon dioxide with rutile(011)-(2x1) surfaces . . .	112
5.3.1	TPD of CO ₂ from TiO ₂ (011)-(2x1)	112
5.3.2	CO ₂ -induced work function change	116
5.3.3	Conclusions – CO ₂ interaction with epitactic rutile(011)-(2x1) films . . .	119
6	Chemical reactivity of rutile(011)-(2x1) films covered with gold	121
6.1	The interaction of the Au/TiO ₂ films with carbon monoxide . . .	121
6.1.1	TPD of CO from Au/TiO ₂ (011)-(2x1)	121
6.1.2	CO-induced work function change on Au/TiO ₂	129

Contents

6.2	Interaction of water with Au/TiO ₂	132
6.3	CO ₂ interaction with Au/TiO ₂	135
6.4	Conclusions – The influence of gold	138
7	Summary	141
8	Zusammenfassung	143
	Bibliography	147
	List of Figures	157
	List of Tables	165
A	Additional information	167
B	Acknowledgment – Danksagung	169
C	Curriculum Vitae	171
D	Publications	173

1 Introduction

Titanium dioxide is one of the most widely used pigments for the production of white paint as a consequence of its high refractive index [1]. Further applications like the purification of polluted air and contaminated water can be traced back to its photocatalytic activity [2]. In dye-sensitized solar cells, titanium dioxide is used as support material [3].

In 1993, Haruta *et al.* [4] communicated a pioneering discovery: They found that small dispersed gold particles supported on different reducible metal oxide powders showed a high catalytic activity towards the low-temperature CO oxidation with oxygen, although the single components exhibit only sparse or no activity at all [5]. Among the studied oxide supports, titanium dioxide (TiO_2) and iron(III)oxide (Fe_2O_3) were found to be especially active.

These oxide-supported catalysts could be applied, among others, for air purification, selective CO gas sensors and for the removal of CO from the hydrogen gas mixture that is used in fuel cells. This is necessary due to the strong poisoning effect CO has on most catalysts. Whereas the common (Pd and Rh-containing) automotive exhaust catalysts are usually working at temperatures ≥ 500 K, the peculiar activity of Au + TiO_2 catalysts renders catalytic CO oxidation even at room temperature possible.

The findings of Haruta *et al.* have stimulated a wealth of studies, which are concerned with the interaction of real catalysts as well as model systems with the gases (CO, O_2 , CO_2) that play a role in the low-temperature CO oxidation

[6, 7, 8]. Most of the model catalyst studies have been performed on rutile single crystals terminated by the thermodynamically most stable rutile(110) surface. Due to their limited thermal and electrical conductivity, the use of fully oxidized rutile single crystals can lead to difficulties concerning, e.g., charging effects during electron spectroscopy analysis or the accurate measurement of temperatures.

The application of thin oxide films grown on conducting metal single crystal substrates can circumvent these problems. Furthermore, the careful choice of metal surfaces, whose geometry matches well with certain desired adsorbate surfaces, allows some kind of control over the structure of the grown surface via epitaxial (= ordered, aligned) growth [9].

The gas phase deposition of titanium dioxide on Ni(110) [10], W(100) [11], Pt(111) [12], Mo(110) [13], Ru(0001) [14] and Re(0001) [15] led almost exclusively to rutile films with (110) orientation.

Since the lattice vectors of the rhenium($10\bar{1}0$) surface unit cell match with certain titanium dioxide structures, we have employed it previously as a template for the epitaxial growth of titania films. Titanium (Ti) deposition onto the Re($10\bar{1}0$) surface at 900 K substrate temperature in an oxygen atmosphere of 1×10^{-6} mbar results in epitaxial growth of rutile terminated by the (2x1) reconstructed (011) surface [16, 17, 18], whose structure was explored only very recently [19, 20].

Although a variety of investigations dealt with the interaction of the reaction gases with rutile(110) (see, for example, [21, 22, 23, 14, 24, 25, 26]) only few studies were concerned with the adsorptive properties of rutile(011) so far [27, 28, 19].

The objective of the present thesis can be roughly divided into three parts. The first part, which will be presented in chapter 4, covers the structural aspects and preparation of the Re($10\bar{1}0$) surface, the epitaxial rutile films and the Au-covered model catalysts. The interaction of the relevant gases (namely CO, CO₂

and H₂O) with the bare rutile(011)-(2x1) films will be discussed in chapter 5. Finally, chapter 6 considers the influence of gold particles deposited on rutile(011) on the gas interaction.

2 Physical and chemical background

2.1 Motivation

2.1.1 The pressure and materials gap in heterogeneous catalysis

A heterogeneous reaction takes – per definition – place at a phase boundary. Restricting ourselves to the phase boundary solid–gas, the most important elementary reaction steps consist of trapping and sticking, adsorption, reaction and product desorption [29].

While industrially applied catalyzed reactions are often carried out under high pressures (≥ 1 bar), at high temperatures (> 300 K) and on highly dispersed catalysts, which provide a large surface area, the surface scientific approach aims at an analysis of the elementary reaction steps using well defined systems at very low reactant pressures. To obtain a system that can be studied in a controlled way, single crystalline metal surfaces are often employed as substrates at moderate temperatures (< 300 K) and under very low pressures (ultra–high vacuum (UHV), $p < 10^{-7}$ mbar).

The advantage of this procedure is that various (electron) spectroscopic methods can be employed (which require vacuum). The disadvantage, however, is that

these “ideal” studies are far away from the real conditions and disregard the influences of high pressures and temperatures on the surface morphology and the mechanism and energetics of the catalyzed reaction.

More application-oriented studies are close to the realistic conditions but often cannot draw conclusions with regard to mechanisms and kinetics, because a variety of different factors contribute to the experimental result.

These distances between the conditions applied in surface scientific studies and real applications are referred to as *pressure* and *materials gap*, respectively.

2.1.2 Low-temperature CO oxidation

Due to the high relevance of the low-temperature CO oxidation with respect to both industrial applications and fundamental science, plenty of studies about the topic can be found. A very informative review article was published by Meyer *et al.* in 2004 ([30] and the references cited therein).

As mentioned before, Haruta *et al.* discovered in 1993 that small gold particles supported on several reducible metal oxides exhibit a high activity regarding the catalysis of the low-temperature CO oxidation [4].

Several possible reasons for the high activity of the supported gold catalysts have been proposed:

- Small gold particles possess a wealth of low-coordinated adsorption sites, which could serve as adsorption or dissociation centres for adsorbing oxygen molecules.
- For quantum chemical reasons, very small gold particles exhibit special electronic and chemical properties. The only role of the substrate here is to support and to stabilize the small gold particles and prevent them from sintering.

- Charged Au particles, for example Au^+ , act as an active center in the reaction.
- Alternatively, the active center is represented by an *anionic* gold species produced by its interaction with a substrate vacancy. This Au^- species is believed to enable the adsorption and dissociation of O_2 molecules.
- The active center is located at the particle – support interface. It is commonly assumed that CO adsorbs on the gold surface while oxygen either *directly* adsorbs on the interface or – in a two-step mechanism – adsorbs at the substrate and then migrates to the interface.

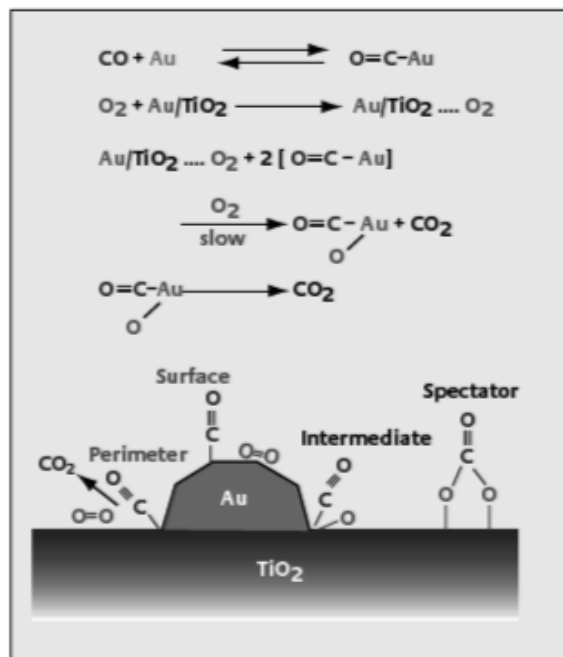


Figure 2.1: Possible reaction pathways for the low-temperature CO oxidation over Au / TiO₂ catalysts. Taken from [30].

While several studies with model catalysts revealed a high activity/particle size dependence, studies with real powder catalysts did not show such clear relationships.

2.1 Motivation

Haruta investigated powder catalysts and found that not the size of the gold particles but their contact with the substrate is the decisive factor. However, due to the wide particle size distribution on powder catalysts and the difficult identification of small particles, the existence of small active particles cannot be excluded.

The influence of geometric effects on the catalytic activity was investigated both theoretically and experimentally. Baiker *et al.* compared the activity of Au / TiO₂ and Au / ZrO₂ catalysts with the same gold particle size [31, 32]. The Au / TiO₂ catalysts showed a considerably higher activity, which was first ascribed to substrate induced effects. HREM (High-resolution electron microscopy) studies revealed that the activity may depend on the particle shape. The Au / TiO₂ catalysts possessed a higher amount of low-coordinated gold atoms, which increased their activity, as already theoretically predicted by Nørskov *et al.* [33, 34].

A common explanation for the high activity of the catalysts is the formation of special adsorption sites at the gold-substrate interface. Since neither pure gold nor pure titanium oxide are very active for the CO oxidation, several groups proposed that the sites created by the interface play a major role in catalysis. Important evidence for this presumption is presented by the studies of Vannice *et al.* [6]. They used “inverse” catalysts, which consisted of titanium dioxide particles deposited on gold powder. These inverse catalysts showed a noticeable catalytic activity, which led the authors to the assumption that the main focus should rather be on the titania-gold interface than on quantum-mechanically caused particle size effects.

Theoretical calculations for the CO oxidation on a magnesia supported gold cluster (34 atoms) by Hammer and Molina revealed that the oxide support apparently serves for the stabilization of the reaction intermediates [35]. They found that the CO adsorption takes place preferably on low-coordinated sites close to

the boundaries of the gold particles. A mechanism with molecular oxygen was favoured due to the high activation energy for the oxygen dissociation. According to the calculations the oxygen molecules adsorb simultaneously on the gold cluster and the substrate and eventually form a CO–O–O complex at the particle boundary.

Apart from the active center the catalytic mechanism itself is not clear either. The following elementary steps are discussed frequently:

- CO reacts with atomic oxygen.
- CO reacts with molecular oxygen.
- Hydroxyl groups take part in the reaction.

Unfortunately, a variety of contradictory results exists also with respect to the reaction mechanism. An insufficient characterization of the real powder catalysts often constitutes a significant problem. Furthermore, the preparation techniques of the different laboratories vary strongly, which does not allow quantitative and most notably comparative statements.

It is therefore important to study well characterized model systems, whose complexity can be increased stepwise. In this way it is also possible to investigate the contributions of certain surface orientations. As several studies reveal that the structure of the catalysts changes under reaction conditions, it is important to apply elevated pressure conditions, i.e., close the pressure gap and study the structure of the model catalysts as well as their activity also at higher pressures.

2.2 Two-dimensional systems: thin film growth

2.2.1 Epitaxy

Epitaxy refers to the method of depositing a monocrystalline film on a monocrystalline substrate. It means that the crystallographic orientation of the grown film is influenced by the crystallography of the substrate as a result of some degree of alignment between the two along the interface. If this leads to oriented overlayers, the deposited film is denoted as epitaxial film or epitaxial layer. The term epitaxy comes from the Greek roots *epi* “above” and *taxis* “in an ordered manner”.

There are three fundamental criteria determining crystal structure, epitaxial relationships and the atomic morphology of the surface:

- The potential energy (E_p) of a chemical bond, which has a sharp minimum at a particular bond length.
- A certain number of bonds corresponding to the “valence“ of the atom to further reduce the overall E_p by filling the outer electron shell.
- Covalently bonded atoms also have an E_p minimum for particular angles between the bonds.

The crystal symmetry provides a bonding environment of minimal E_p for every atom, whereas disorder forces some atoms into bonding environments of higher E_p in polycrystalline or amorphous materials. As any interruption of the crystal symmetry increases E_p , surfaces and interfaces have an excess energy per unit area (γ). Upon film deposition on a single-crystal substrate this interfacial energy is minimized by maximizing the density of bonds of appropriate length and angle across the interface in an attempt to merge the symmetries of the two crystals. This means that it is energetically favourable for the deposited film material to align itself with the substrate in a way that it matches the bonding

symmetry and periodicity of the substrate, which is called epitaxial growth.

Epitaxy occurs for any combination of film and substrate with some degree of matching, if both the substrate symmetry is not masked by interfacial disorder and the temperature is high enough to allow the rearrangement of the deposited atoms into equilibrium positions.

The growth of a material onto itself is called *homoepitaxy*. In this case, the (clean) film/substrate interface vanishes into the bulk material resulting in an interface energy γ_i of zero. Homoepitaxy is applied to grow a more purified film than the substrate and to fabricate layers with different doping levels.

Heteroepitaxy of one material onto another results in $\gamma_i > 0$; the preferred crystallographic orientation of the film is often that which minimizes γ_i and maximizes bonding across the interface. It is applied to grow crystalline films of materials of which single crystals cannot be obtained or to build thin films with a certain surface orientation.

A fundamental criterion for epitaxy is a moderately small mismatch (f) in the atomic periodicities of the two materials along the interface, which is defined by:

$$f = \frac{a_e - a_s}{(a_e + a_s)/2}. \quad (2.1)$$

a_e and a_s represent the atomic spacings along some direction in the film crystal and the substrate surface, respectively. To obtain epitaxy, f needs to be smaller than 0.1, otherwise not enough interfacial bonds are aligned to reduce γ_i significantly [9].

2.2.2 Thermodynamics of thin film growth

The thermodynamic crystal growth on surfaces was, among others, investigated by Bauer [36]. The appearance of a particular growth behaviour is thereby ascribed to the surface energies of the substrate σ_S , the interface σ_G and the adsorbate σ_A . Three cases are distinguished:

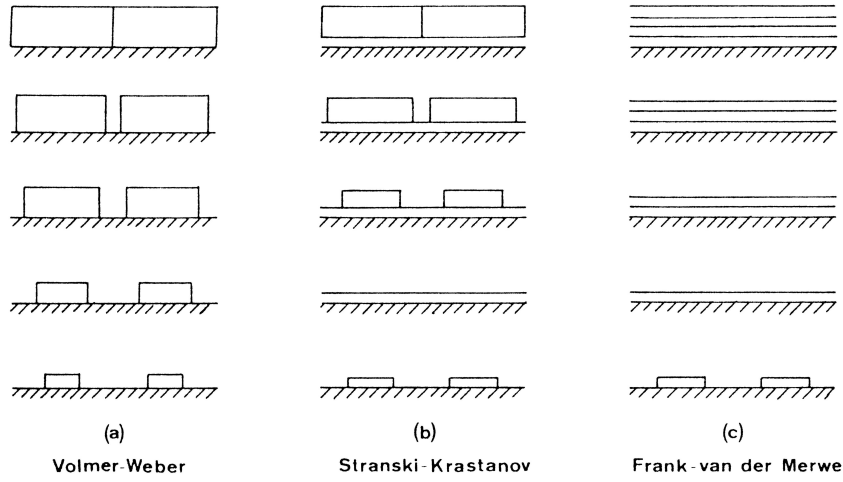


Figure 2.2: The three basic growth mechanisms for thin films deposited from the gas phase [36].

If $\sigma_S < \sigma_A + \sigma_G$, three-dimensional growth occurs to prevent a wetting of the energetically favoured substrate surface (*Volmer-Weber*).

For $\sigma_S \geq \sigma_A + \sigma_G$ a two-dimensional adsorbate layer grows onto the surface. This layer has to be considered for the following growth behaviour: For $\sigma_{(S+L)} > \sigma_A + \sigma_G$, layer by layer growth results (*Frank-van der Merwe*). If the relation changes to $\sigma_{(S+L)} < \sigma_A + \sigma_G$, three-dimensional growth follows on the first layer (*Stranski-Krastanov*).

These three possibilities are illustrated in figure 2.2.

2.2.3 Thin film growth from a kinetic point of view

As most systems are not in thermodynamic equilibrium at room temperature, film growth is often kinetically controlled by processes such as adsorption on substrate terraces, diffusion and desorption of adatoms, leading to homogeneous or heterogeneous nucleation ([37, 38], see figure 2.3).

The mobility of adsorbed atoms or molecules determines if cluster formation or

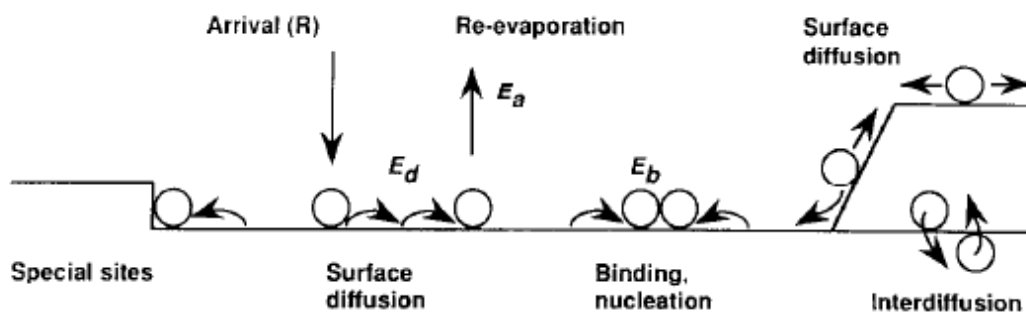


Figure 2.3: Schematic diagram of processes and characteristic energies in nucleation and growth on surfaces. Taken from reference [38].

an attachment at a defect site occurs. Homogeneous nucleation between identical adsorbates on the surface depends on the adsorbate concentration and thus on the deposition rate.

Heterogeneous nucleation occurs preferentially at steps, since the coordination number of the surface atoms is lower than within a layer facilitating the adsorption of atoms or molecules. At the edges a potential minimum exists that decreases the probability of homogeneous nucleation. Additionally a potential barrier might prevent the movement of adatoms across the edges if the activation energy to surmount the edge is higher than the energy required for diffusion along the surface. Consequently, the adsorbates are either captured at the potential minimum or reflected at the potential barrier (Ehrlich–Schwoebel barrier) [39, 40].

2.2 Two-dimensional systems: thin film growth

These barriers also occur at the boundary of homogeneous nuclei leading to three dimensional growth if the barriers cannot be surmounted by the adatoms.

The kinetic control of the film growth is less important at higher temperatures when the barriers can easily be overcome.

2.3 Materials and their chemistry

2.3.1 Rhenium (Re)

In 1925, Walther Noddack and Ida Tacke discovered rhenium in fractions of processed *columbit* (Fe, Mn)[NbO₃]₂ and *tantalit* (Fe, Mn)[TaO₃]₂ by means of x-ray spectroscopy. They called it rhenium after their home, the Rheinland. Rhenium is a very rare metal with a fraction of only 10⁻⁷ % in the earth crust. It is only available scattered and in very low concentrations (< 0.0001 %). Molybdenum ores like MoS₂ (Molybdanglanz) are relatively rich of rhenium. *Columbit* (see above), *gadolinit* Y₂(Fe^{II}, Mn^{II})Be₂O₂[SiO₄]₂ and *alvit* ZrSiO₄ are other minerals, which contain rhenium.

During the calcination of molybdenum sulfide ores Re₂O₇ enriches in the fine dust and dissolves as ReO₄⁻. In order to isolate the Re, it is first precipitated as NH₄ReO₄, from which it is then obtained as grey powder after reduction with hydrogen at 400 – 1000 °C.

Rhenium ist a white–gleaming, hard, air–resistent metal, which is quite similar to platinum. It exhibits the second highest melting point of all metals and dissolves only in oxidizing acids like azotic acid and sulphuric acid [1, 41, 42].

2.3.2 The peculiar Re(10 $\bar{1}0$) orientation

Rhenium crystallizes in the hexagonal close–packed lattice. The dimensions of the volume unit cell are $a = b = 2.761 \text{ \AA}$, $c = 4.456 \text{ \AA}$, $\alpha = \beta = 90^\circ$ and $\gamma = 120^\circ$ [43]. Figure 2.4a shows the rhenium lattice with the primitive unit cell. There are two possibilities to obtain the (10 $\bar{1}0$) surface. The necessary cuts are marked with the two red lines in figure 2.4a. A LEED analysis from Davis and Zehner [44] showed that the less corrugated surface is the more stable configuration that exists in nature (marked by the dotted line in figure 2.4a). A later LEED study by Doll *et al.* resulted in the same finding [45]. In the less corrugated surface, the

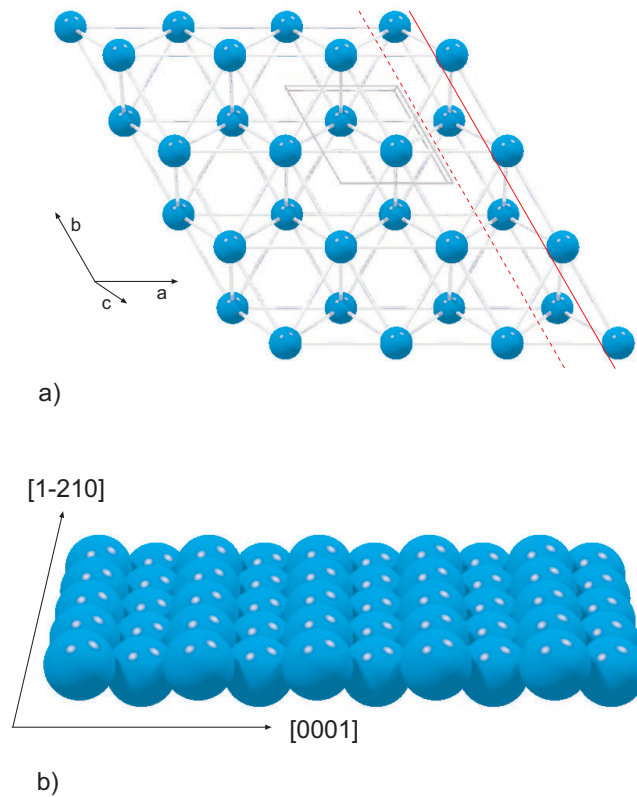


Figure 2.4: a) The rhenium lattice with its primitive unit cell; b) The $\text{Re}(10\bar{1}0)$ surface.

Re atoms have eight instead of six neighbours. Figure 2.4b shows the $\text{Re}(10\bar{1}0)$ surface. The dimensions of the rectangular surface unit cell are $\vec{a}_1 = 2.761 \text{ \AA}$ in $[1\bar{2}10]$ direction and $\vec{a}_2 = 4.456 \text{ \AA}$ in $[0001]$ direction. Hence, the $\text{Re}(10\bar{1}0)$ surface is highly anisotropic providing troughs in $[1\bar{2}10]$ direction.

2.3.3 Titanium (Ti)

Titanium was discovered in the mineral *ilmenite* in 1791 by William Gregor and independently in 1795 by Martin Heinrich Klaproth in the mineral *rutile*. It was named by M.H. Klaproth after the mythologic titans.

Titanium takes part in the earth crust with 0.64% and is thereby among the

ten most common elements. It exists widely spread in the nature only bound as an oxide with the two most important minerals *ilmenite* FeTiO_3 and titanium dioxide TiO_2 .

Due to the formation of carbides and nitrides, titanium cannot be synthesized by reduction with carbon. It is therefore obtained technically via the *Kroll process*. For that purpose, the oxide is first transferred to TiCl_4 by chlorine, which is led over an 800°C hot mixture of coke and TiO_2 . The TiCl_4 is cleaned by fractional distillation and afterwards reduced under argon at $950\text{--}1150^\circ\text{C}$ with a magnesium melt.

Titanium is a silvery white, high-melting, ductile and ignoble metal. It is highly corrosion-resistant due to a thin passivating oxide layer, which is generated on the surface in air. It belongs to the group of light metals, exhibits a high mechanical resistance and a low thermal expansion coefficient [1, 41, 42].

2.3.4 Titanium oxides, chemistry and crystallography

The most important oxide is titanium dioxide (TiO_2). At room temperature it exists in the three modifications rutile, anatase and brookite, rutile being the most common one. Anatase and brookite transform into rutile, when they are heated. Rutile kann be reduced to various non-stoichiometric oxide phases [1].

Rutile

In the rutile structure, the oxygen anions build a slightly distorted hexagonal close-packed structure. The titanium cations occupy every second octahedral hole and thus constitute a body centered tetragonal unit cell with $a = b = 4.584 \text{ \AA}$ and $c = 2.953 \text{ \AA}$ [41, 46].

The octahedra are connected to strands over the edges; the strands are connected to one another over the corners of the octahedra. The oxygen anions are distorted

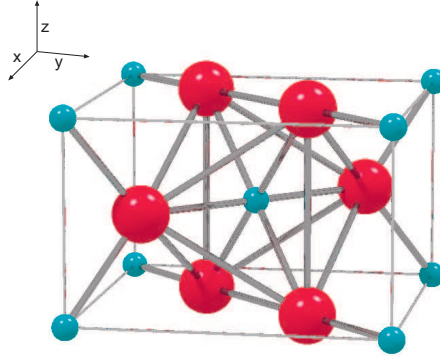


Figure 2.5: The tetragonal unit cell of rutile; red spheres: oxygen atoms, green spheres: titanium atoms.

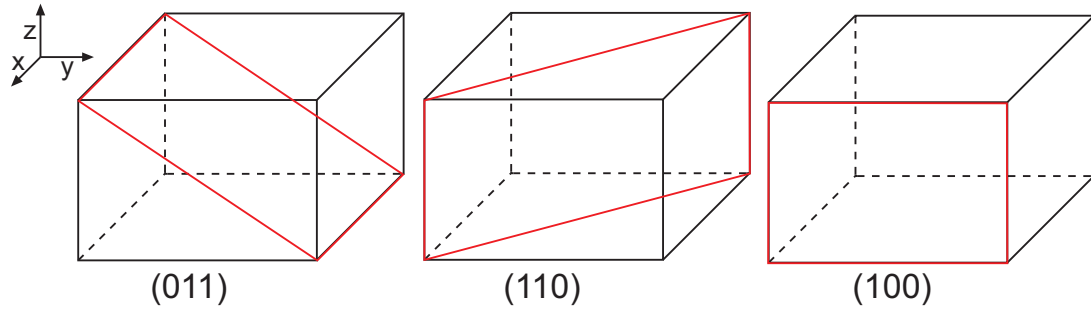


Figure 2.6: The three most stable rutile surfaces.

trigonally coordinated by titanium ions, which are coordinated octahedrally by oxygen ions ($\text{TiO}_{6/3}$) [48, 49]. Ramamoorthy *et al.* calculated the surface energies of different relaxed unreconstructed rutile surfaces [47]. From the calculated energies and the geometric relations of the planes, they determined the equilibrium shape of a rutile crystal via the *Wulff construction* (see figure 2.7). It arose, however, that the (001) surface forms (2×1) reconstructed $\{011\}$ facets when heated to 900 K [50]. Reconstruction processes are lateral changes in the positions of the surface atoms leading to new surface periodicities. The driving force is mostly a lower free surface energy. Therefore, the thermal faceting reveals that the (2×1) reconstructed $\{011\}$ facets have a lower free surface energy than the (001) surface. Referring to figure 2.7, it follows that the $\{011\}$ surfaces grow together and

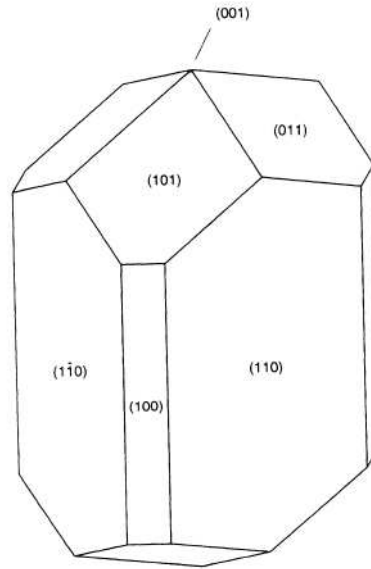


Figure 2.7: Equilibrium shape of a macroscopic rutile crystal [47].

the $\{001\}$ surfaces disappear. The (110) surface is the most stable rutile surface. Figure 2.6 shows how the (110) , (011) and (100) surfaces are located in the rutile unit cell.

Rutile $\text{TiO}_2(110)$

A model of the rutile (110) surface is shown in figure 2.8; the titanium atoms form a centered rectangular surface unit cell. The titanium atoms, which are located

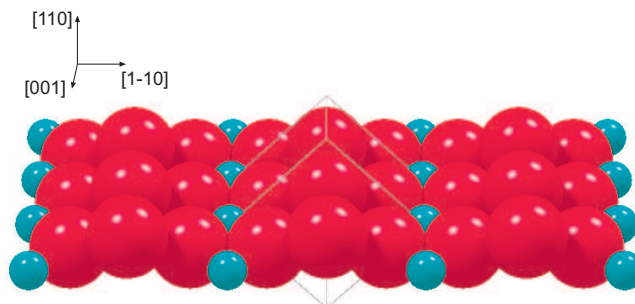


Figure 2.8: Rutile $\text{TiO}_2(110)$; red spheres: oxygen atoms, green spheres: titanium atoms.

at the corners of the unit cell in figure 2.8, are *fivefold*, and the titanium atom in the center of the unit cell is *sixfold* coordinated. The bridging oxygen atoms form chains in $[001]$ direction; they are *twofold* coordinated. Rows of *threefold* coordinated oxygen atoms connect the Ti-chains in the plane. The surface relaxes in $[110]$ direction by moving the undercoordinated O- and Ti-atoms inwards and the other O- and Ti-atoms outwards. More details can be found in the literature [47].

Rutile $\text{TiO}_2(100)$

The rutile(100) surface is more corrugated than the (110) surface. It possesses a rectangular unit mesh along the bulk $[010]$ and $[001]$ directions, which contains one TiO_2 unit. The titanium atoms in the surface are fivefold coordinated with

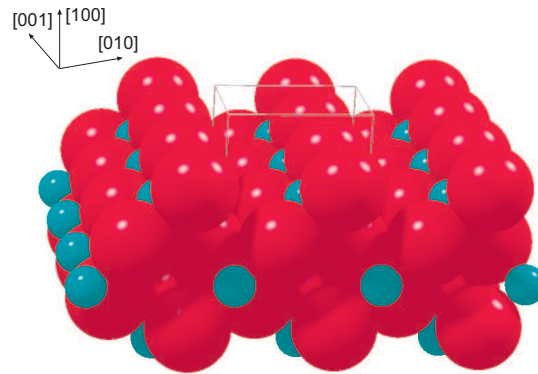


Figure 2.9: Model of the unrelaxed rutile(100) surface; red spheres: oxygen atoms, green spheres: titanium atoms.

truncated oxygen octahedra. In the unrelaxed surface, which is depicted in figure 2.9, the equatorial planes of the octahedra are inclined at 45° with respect to the surface normal. Similar to the (110) surface, the (100) surface exhibits rows of twofold coordinated bridging oxygen atoms. The chains of TiO_2 atoms are rotated by 90° in the second layer, which yields a very corrugated surface with rows and troughs in $[001]$ direction [47].

Rutile $\text{TiO}_2(011)$

The unreconstructed $\text{TiO}_2(011)$ surface is shown in figure 2.10. The dotted line marks a glide mirror plane in $[01\bar{1}]$ -direction. According to the literature [51], the (011) surface exists only (2x1) reconstructed and remains stable after annealing to 850 °C. The structure of the (2x1) reconstructed (011) surface is still under debate. In 2004, Beck *et al.* proposed a surface model for the (2x1) reconstructed surface on the basis of density functional theory (DFT) calculations, STM images and LEED patterns [51]. The peculiarity of this model is the existence of singly-coordinated oxygen atoms on top of the rows, which are bound to the titanium atom via a double bond (titanyl groups). These titanyl groups represent a rather unique structural element for TiO_2 surfaces and were believed to account for the higher photocatalytic activity of the rutile(011)-(2x1) surface. In 2007, however, Kubo *et al.* proposed a ‘microfaceting’ missing-row-type structure for the (2x1) reconstructed rutile(011) surface [52].

Very recently, a third model for the (2x1) reconstructed (011) surface was pre-

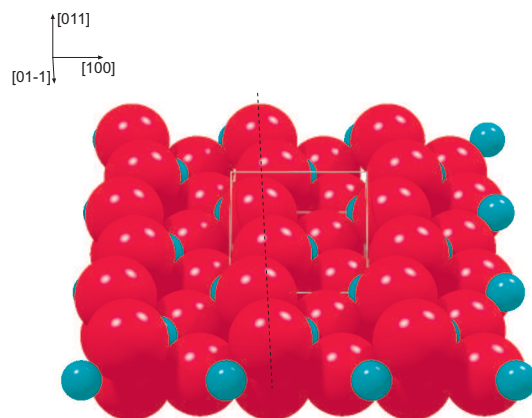


Figure 2.10: Rutile $\text{TiO}_2(011)$ -(1x1); the dotted line marks the glide mirror plane; red spheres: oxygen atoms, green spheres: titanium atoms.

sented [53, 54]. Gong *et al.* and Torrelles *et al.* simultaneously found a new model by means of DFT calculations, surface x-ray diffraction (SXRD) and STM

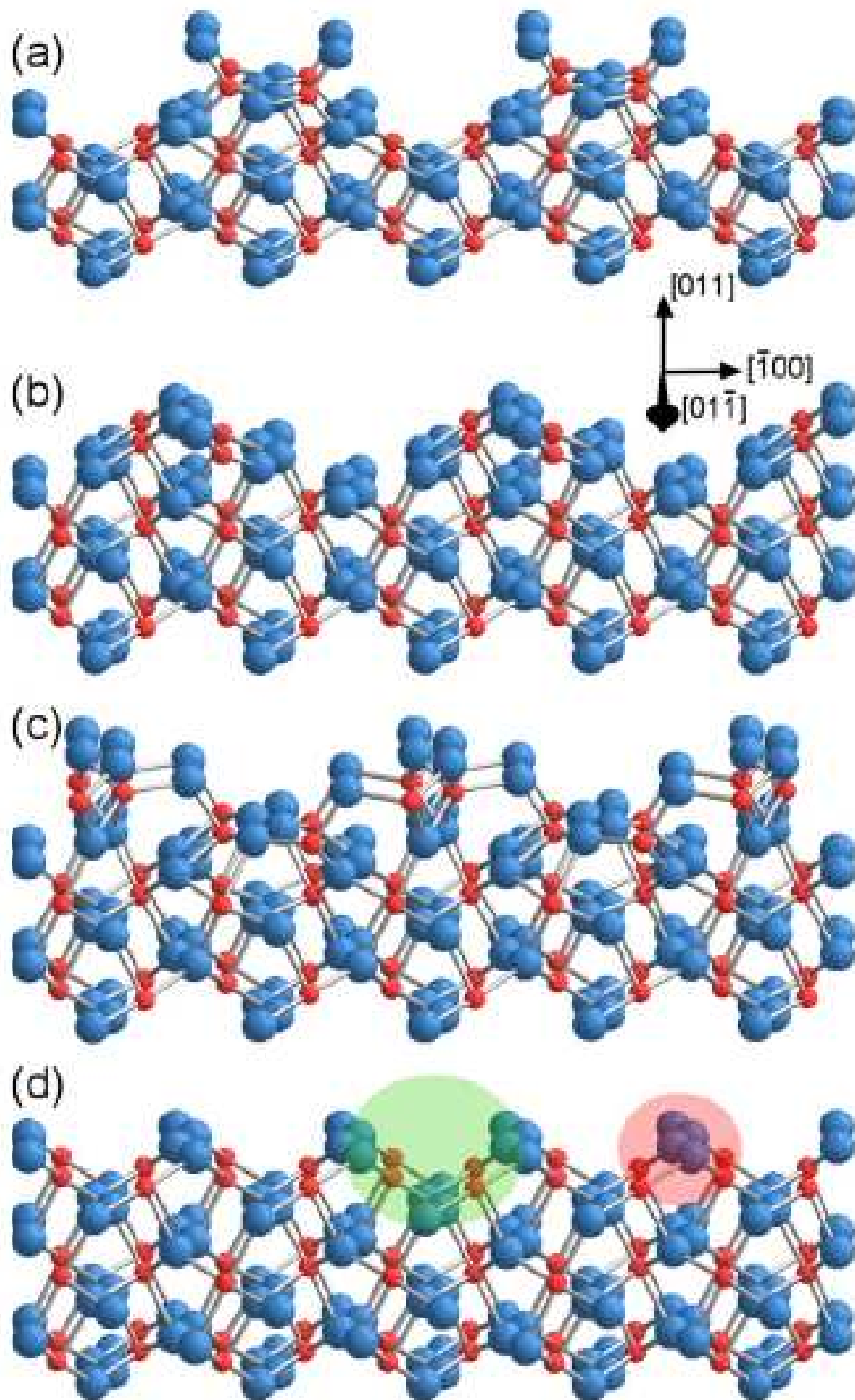


Figure 2.11: Ball and stick models of the rutile $\text{TiO}_2(011)-(2 \times 1)$ surface; blue spheres: oxygen atoms, red spheres: titanium atoms; a) 'titanyl' model from Beck *et al.* [51], b) 'microfaceting' model from Kubo *et al.* [52], c) new 'brookite(001)-like' model [19, 20], d) unreconstructed $\text{TiO}_2(011)$ surface. Taken from reference [20].

[19, 20]. The reason for the new investigations was the high surface energy of the 'titanyl' model (0.85 J/m^2), which is only marginally lower than the one of the unreconstructed (011) surface (0.89 J/m^2) [19]. Ball and stick models of the different proposed models and the unreconstructed (011) surface are depicted in figure 2.11. While the 'titanyl' (fig. 2.11a) and the 'microfaceting' model (figure 2.11b) are both missing-row-type structures, the new model was derived by a rearrangement of all the surface atoms. Due to its similarity to the brookite(001) surface [16] Gong *et al.* named it 'brookite(011)-like' model (calculated surface energy = 0.42 J/m^2). This new model does not contain singly bound oxygen atoms. The topmost layer of the surface exhibits zigzag rows of twofold coordinated oxygen atoms. The oxygen atoms at the sides of the valleys are also twofold coordinated. Furthermore, the surface contains two different types of fivefold coordinated titanium atoms, on the top and in the valleys. In bulk rutile(011), the oxygen atoms are threefold and the titanium atoms sixfold coordinated.

Gong *et al.* expect the surface to be rather inert with respect to the adsorption of small probe molecules, given that the titanium atoms on the top are shielded by oxygen and the Ti atoms in the valleys do not provide a dangling bond towards the vacuum either [19]. Due to preliminary DFT calculations, water is supposed to adsorb via H-bonds with on-top oxygen of the rutile surface, leading to adsorption energies below 0.15 eV ($= 14.5 \text{ kJ/mol}$). The opposed experimental adsorption behaviour of water [28, 27] is explained by defect-mediated processes [19].

Anatase and brookite

Anatase and brookite are both based on a cubic close-packed structure. Half of the octahedral holes is filled with titanium ions in a way that every TiO_6 octahedron has three shared edges with other octahedra in brookite and four in anatase [41].

2.3.5 Gold (Au)

Gold is a very noble metal, which exists in nature mainly in its native state, i.e., in the form of gold-containing *quartz* SiO_2 and *pyrite* FeS_2 , but also bound as *sylvanite* AuAgTe_2 , *nagyagite* $(\text{Pb,Au})(\text{S,Te,Sb})_{1-2}$ and *calaverite* AuTe_2 . The native gold in nature is never chemically pure, but highly contaminated with silver and small amounts of copper, platinum and other metals.

Gold occurs in veins and alluvial deposits and is often separated from rocks and other minerals by sluicing and panning operations. The metal is recovered from its ores by amalgamating, cyaniding and smelting processes. The raw gold can be cleaned from contaminants like silver by treatment with concentrated sulfuric acid, in which the contaminants are dissolved, or by electrolysis.

Pure gold is a reddish yellow soft metal, which melts to a shiny green liquid at 1336 K and boils at 2933 K [41]. The gold vapour consists mainly of gold dimers Au_2 , which have a similar dissociation energy as Cl_2 ($E_{\text{D}}(\text{Au}_2) = 232 \text{ kJ/mol}$, $E_{\text{D}}(\text{Cl}_2) = 244 \text{ kJ/mol}$). The most remarkable property of gold is its high ductility, which beats every other metal. It can be rolled out to $0.1 \mu\text{m}$ thin lamina [55].

Gold dissolves only in strong oxidizing reagents like *aqua regia*¹ and in complex builders like potassium cyanide solution. In Au compounds, which are all quite unstable, Au mainly exhibits the oxidation states +1 and +3.

Gold is used in coinage and is a standard for monetary systems in many countries. Furthermore, it is extensively used for jewelry, decoration, dental work, and for plating.

Gold crystallizes in a face-centered cubic lattice with a lattice constant of 4.078 \AA .

Table 2.1 summarizes some physical properties of rhenium, titanium and gold.

¹*Aqua regia* is a 1:3 mixture of nitric acid (HNO_3) and hydrochloric acid (HCl).

	Rhenium (Re)	Titanium (Ti)	Gold (Au)
Atomic number Z	75	22	79
Electron configuration	[Xe]4f ¹⁴ 5d ⁵ 6s ²	[Ar]3d ² 4s ²	[Xe]4f ¹⁴ 5d ¹⁰ 6s ¹
Relative atom mass	186.207	47.867	196.966
Isotopes (natural abundance)	185 (37.4 %), 187 (62.6 %)	46 (8.3 %), 47 (7.4 %), 48 (73.7 %)	196.966 (100 %)
Electronegativity (Allred and Rochow)	1.5	1.3	1.42
Density / g cm ⁻³ at 20°C	21.03	4.51	19.32
Melting point / K	3453	1933	1337
Boiling point / K	6143	3535	2933 (3129)
Oxidation numbers	7 , 6, 4, 2, -1	4 , 3	5, 3 , 2, 1 , -1
Atom radius / pm	137.1	144.8	144.2
Ion radii / pm			
Me ⁵⁺			71 (c.n. = 6, o)
Me ⁴⁺		61 (c.n. = 6)	
Me ³⁺		67	82 (c.n. = 4, sp)
Me ³⁺			99 (c.n. = 6, o)
Me ¹⁺			151 (c.n. = 6, o)
1 st ionization energy / eV	7.88	6.82	9.23
2 nd ionization energy / eV		13.6	20.5
3 rd ionization energy / eV		27.5	30.1
4 th ionization energy / eV		43.2	43.5
4 th ionization energy / eV			58.0

Table 2.1: Physical properties of rhenium, titanium and gold; o = octahedral, sp = square-planar. Data taken from [42, 56, 41, 57, 58].

3 The experiments and their set-up

3.1 The ultra-high vacuum system (combined LEED, AES, TDS and $\Delta\Phi$ machine)

Most of the experiments were carried out in an ultra-high vacuum recipient made from stainless steel. The recipient is depicted in figure 3.1. It is equipped with a cylindrical mirror analyzer with an implemented electron gun for Auger-electron spectroscopy (*Physical Electronics Industries*), a reverse-view retarding field LEED optics (*Omicron Spectaleed*), a Kelvin probe for work function change measurements, a differentially pumped quadrupole mass spectrometer (*Balzers Prisma, QME 200*) for residual gas analysis and temperature-programmed desorption (TPD) and an ion gun for sputtering (*LH*). Furthermore, two evaporation sources are attached, one commercial UHV evaporator (*Omicron, EFM3*) for titanium and one home-made evaporator for gold. The recipient is pumped by one 180 litre/s turbomolecular pump backed by a four-stage membrane pump (*ABM*) as rough pump, one ion getter pump (*Varian*), one titanium sublimation pump and one 60 litre/s turbomolecular pump (*Pfeiffer TMU071P*) for the differential pumping of the mass spectrometer chamber.

The argon gas for the sputtering is directly attached to the ion gun via a bakeable leak-valve while the rest of the gases (CO, CO₂, O₂, H₂) is connected to a gas inlet system made from *Swagelok* fittings and tubes, which is pumped by a rotary pump and passed into the recipient via a separate leak-valve. The purity

3.1 The ultra-high vacuum system

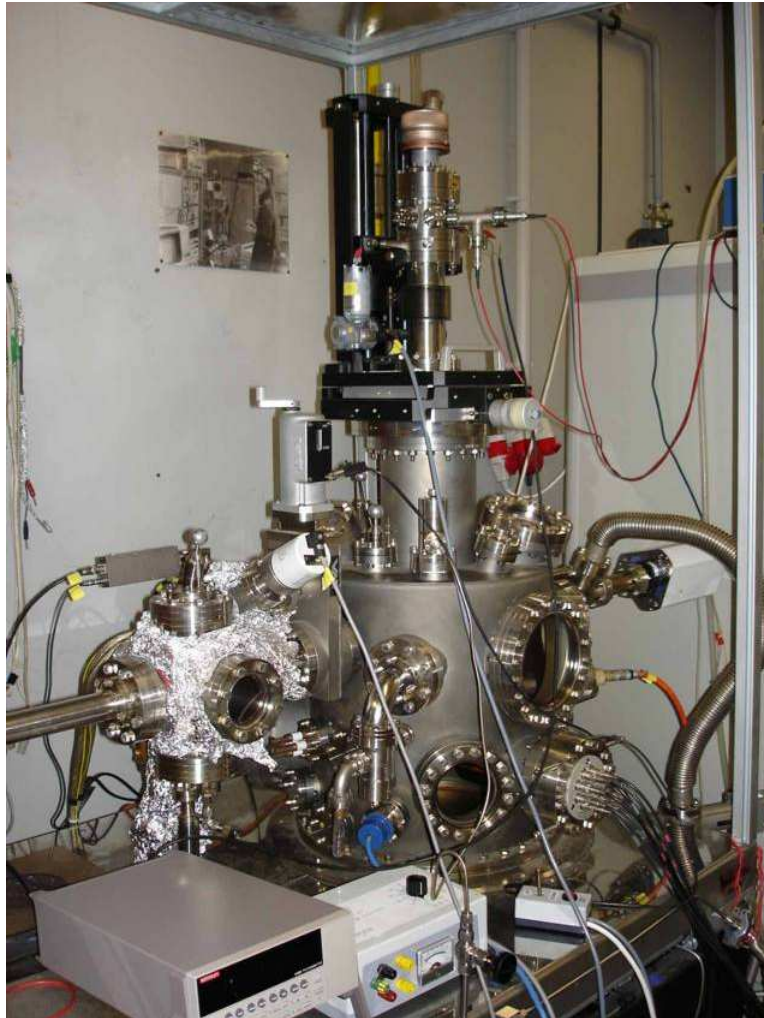


Figure 3.1: The ultra-high vacuum recipient used in the present thesis.

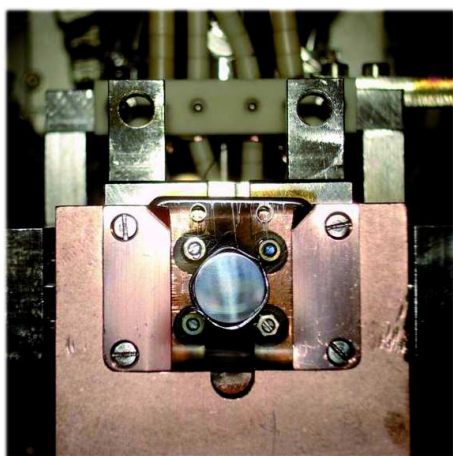
of the gases that were used for cleaning and measurements (Ar, CO, CO₂, O₂) was checked regularly by means of mass spectrometry.

In order to remove adsorbed molecules (especially H₂O) from the walls of the recipient, the chamber was baked out regularly for 60 hours at 125°C. Thereby, a base pressure of $p = 2 \times 10^{-10}$ mbar was obtained. A detailed description of the vacuum system can be found in reference [59]¹.

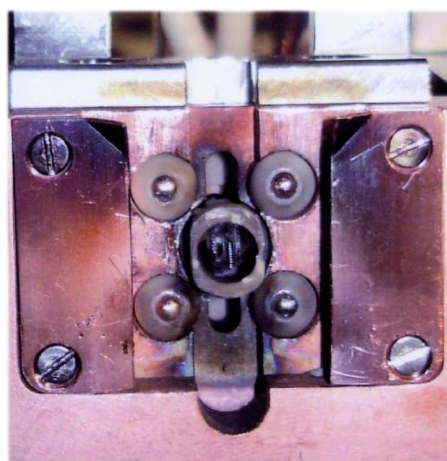
¹Our used equipment deviates from the one described in reference [59].

3.1.1 The sample holder

The rhenium crystal is mounted on an off-axis sample holder, which is depicted in figure 3.2a. The sample holder consists of a sapphire plate, which is slid behind



(a) Sample holder with sapphire plate and mounted rhenium crystal.



(b) Sample holder without sapphire plate. The tungsten filament behind the sample is visible.

Figure 3.2: Image of the off-axis sample holder at the end of the manipulator.

two small copper plates. The crystal is mounted onto the sapphire plate with a rhenium wire (diameter = 0.5 mm), which is fixed onto the plate via small stainless steel screws that connect the crystal to steel contacts, which provides an electrical connection. Type K thermocouple wires are spot-welded to the rim of the crystal and connected to the manipulator via screws made from the same thermocouple material. The high thermal stability and the low thermal conductivity of sapphire ($\alpha\text{-Al}_2\text{O}_3$) at high temperatures allow sample heating without an intense warm-up of the environment whereas fast sample cooling can be achieved due to the high thermal conductivity of sapphire at low temperatures. The sample holder is mounted at the end of the manipulator, which enables the movement of the sample in x-, y- (both ± 17 mm) and z-direction, 360° rotations

3.1 The ultra-high vacuum system

around the manipulator axis and tilting of the sample perpendicular to the surface normal.

The sample can be heated both resistively through the electronic contacts and via electron bombardment from the back side of the crystal. In the present thesis, the crystal was almost exclusively heated by electron bombardment. The electrons are produced by a tungsten filament attached to the sample holder (see figure 3.2b) and accelerated onto the crystal by a negative high voltage of $U \leq 1000$ V, which is applied to the filament. The distance between the filament and the back of the crystal is smaller than 1 mm.

Cooling of the sample to about 100 K can be achieved via liquid nitrogen, which is pumped to the sample holder and back through flexible stainless steel pipes.

3.1.2 The titanium evaporator

Titanium was evaporated with a commercial UHV-evaporator (*EFM3-Omicron*), which works similar to an electron bombardment heating. The main parts are a titanium rod (*Goodfellow*, $d = 2$ mm, purity $> 99.99\%$) and a spiral-wound thoriated tungsten filament. They are both surrounded by a water-cooled Cu body that can be baked out independently and minimizes degassing during the Ti evaporation. A high voltage (≈ 1000 V) is applied between the filament and the Ti rod, which accelerates the emitted electrons onto the Ti rod and eventually melts and vapourizes the titanium in the top of the rod. The Ti atoms are focussed onto the crystal by a nozzle. A small amount of the atoms is ionized by collisions with the electrons. The ions that hit the inner surface of the nozzle induce a small current, which is displayed at the flux monitor. The ratio of evaporated/ionized titanium atoms is unknown, but was found to be constant at a certain Ti flux (in the present work a flux of 50 nA was used).

In order to achieve a homogeneous titanium distribution on the crystal surface,

the position of the crystal was optimized. For this purpose, the sample current, which consists of electrons and titanium cations from the evaporator, was measured with a picoampèremeter and maximized by varying the crystal position ($I_{max} \approx 0.9 \text{ nA}$).

3.1.3 The gold evaporator

A gold evaporator was designed² and built for the preparation of the Au/rutile/Re model catalysts. A picture of the interior and therefore the important parts is displayed in figure 3.3. The principle is straightforward. A very thin ($\varnothing_{out} \approx$



Figure 3.3: Picture of the inner parts of the gold evaporator that was used in the present thesis.

1.5 mm) two-hole ceramic tube is inserted 3 mm wide into a slightly thicker one-hole ceramic tube ($\varnothing_{in} \approx 1.5 \text{ mm}$). The two wires of a type D thermocouple (W-3% Re/W-25% Re) are passed some millimeters deep into the one-hole ceramics through the two holes of the thinner ceramics. The welding spot of the thermocouple is located in the one-hole-ceramic, which also takes up the gold wire. The outer ceramics is surrounded by a spiralled tungsten filament; the ends are connected to two independent copper electrodes, which also serve as a frame for the evaporator. The tungsten filament heats the ceramics and eventu-

²The principle was adopted from reference [17].

3.1 *The ultra-high vacuum system*

ally melts the Au³. The Cu electrodes as well as the thermocouple wires are fed through CF flanges. During the Au deposition the temperature of the Au was measured and held constant by regulating the heating current⁴. The orifice of the evaporator can be closed by a rotatable shutter (the shutter is not mounted in the picture) thereby allowing an exact control of the deposition time.

³The applied voltage and current were around 15 V and 4 A, respectively.

⁴To achieve a proper temperature measurement, a cold junction (ice-water mixture) was used before the thermoelectric voltage was read into the AD-board of the PC.

3.2 Structure determination by low-energy electron diffraction (LEED)

3.2.1 Surface structures

In order to describe surface structures, the 14 three-dimensional Bravais lattices are replaced by five two-dimensional ones (see figure 3.4). According to the

$$T = h' \cdot a_1 + k' \cdot a_2 \quad (h', k' = \text{integers}) .$$

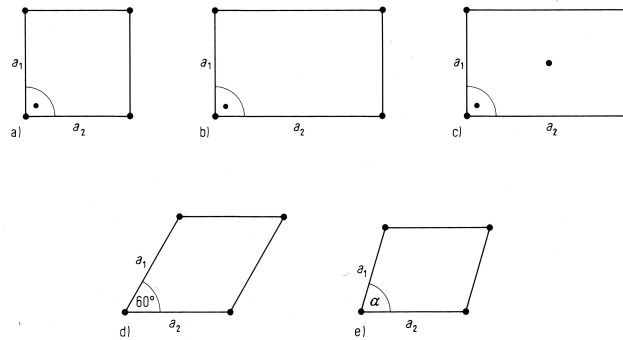


Figure 3.4: The five surface Bravais lattices: a) square, $a_1 = a_2$, $\alpha = 90^\circ$; b) primitive rectangular, $a_1 \neq a_2$, $\alpha = 90^\circ$; c) centered rectangular, $a_1 \neq a_2$, $\alpha = 90^\circ$; d) hexagonal, $a_1 = a_2$, $\alpha = 60^\circ$; e) oblique, $a_1 \neq a_2$, $\alpha \neq 90^\circ$ [60].

conventions of x-ray crystallography, the indices of the lattice vectors are chosen in a way that $|\vec{a}_1| \leq |\vec{a}_2|$.

Ordered adsorbate layers can yield changes in the surface periodicity. For thin adsorbate layers, the diffraction pattern exhibits both substrate and adsorbate reflexes. The expression of the relation between the surface lattice (\vec{b}_1, \vec{b}_2) and the substrate lattice (\vec{a}_1, \vec{a}_2) contains the ratio of the lengths of the vectors b_1/a_1 and b_2/a_2 and the angle of rotation ϑ between the two lattices (*Wood nomenclature* [60]). The surface unit cell can be either primitive (p) or centered (c) (s. Abb. 3.5).

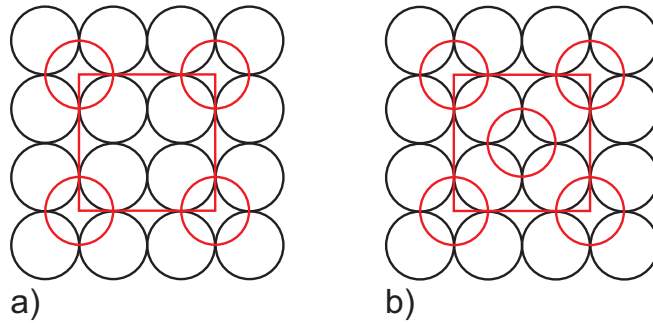


Figure 3.5: Examples for adsorbate superstructures; a) (2×2) , b) $c(2 \times 2)$ and $(\sqrt{2} \times \sqrt{2})R 45^\circ$, respectively; black circles: substrate atoms, red circles: adsorbate atoms/molecules.

3.2.2 The origin of the diffraction pattern

During a LEED experiment the surface is irradiated with electrons of a certain wavelength. The diffraction pattern of the electrons is then observed on a fluorescent screen. The wavelength of an electron is given by the *de Broglie* equation:

$$\lambda = \frac{h}{m \cdot v} . \quad (3.1)$$

For a two-dimensional lattice, interference occurs in the following directions:

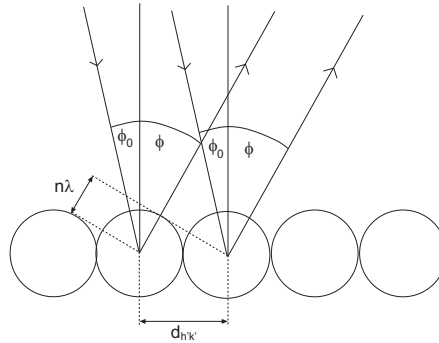


Figure 3.6: Scattering of electrons on a one-dimensional chain of atoms.

$$n \cdot \lambda = d_{h'k'} (\sin \varphi - \sin \varphi_0) \quad (3.2)$$

with the order of diffraction n , the wavelength of the electrons λ , the angle of incidence φ_0 and the angle of reflection φ . In an ensemble of parallel rows of

scatterers with directions h' and k' (*Miller indices*), $d_{h'k'}$ denotes the distance of the rows. Presuming the LEED experiment is carried out with perpendicular incidence of the electron beam ($\varphi_0 = 0$), equation [3.2] simplifies to:

$$\sin\varphi = \frac{n \cdot \lambda}{d_{h'k'}}. \quad (3.3)$$

Mostly, the order of diffraction is included in the *Miller indices* yielding $h = n \cdot h'$ and $k = n \cdot k'$. Each reflex appears the first time at an electron energy of $U = 1.5/d_{hk}^2$ and moves into the direction of the (00) reflex (direct reflection), when the electron energy is increased. The distances d_{hk} can be deduced from the LEED patterns, thus revealing the geometry of the surface unit cell. The *position* of the reflexes does not allow conclusions concerning the arrangement of the atoms in the unit cell. This can only be achieved by analysing the beam *intensities*.

3.2.3 The reciprocal lattice

The elastic interaction of electrons with a surface is treated like the scattering of waves on a two-dimensional lattice. This approach neglects both the finite thickness of the surface region and the intrusion of electrons into deeper layers.

The surface unit cell with the base vectors \vec{a}_1 and \vec{a}_2 is the smallest parallelogram, from which the lattice can be constructed by translation operations. The base vectors \vec{a}_1^* and \vec{a}_2^* of the reciprocal lattice have to fulfil the following conditions:

$$\vec{a}_i \cdot \vec{a}_j^* = \delta_{ij} \quad (3.4)$$

with the *Kronecker*-symbol $\delta_{ij} = 0$ for $i \neq j$ and $\delta_{ij} = 1$ for $i = j$ and $i, j = 1, 2$. For the construction of the reciprocal lattice from the real lattice, the following relations result:

$$\vec{a}_1^* = \frac{1}{\vec{a}_1 \cdot \sin \gamma} \quad (3.5)$$

$$\vec{a}_2^* = \frac{1}{\vec{a}_2 \cdot \sin \gamma}. \quad (3.6)$$

3.2 Structure determination by low-energy electron diffraction (LEED)

The angle γ^* between \vec{a}_1^* und \vec{a}_2^* is given by:

$$\gamma^* = \gamma + 2 \left(\frac{\pi}{2} - \gamma \right) = \pi - \gamma, \quad (3.7)$$

yielding $\sin \gamma^* = \sin \gamma$. The areas of the real space and the reciprocal space unit cell are:

$$A = a_1 a_2 \sin \gamma = | \vec{a}_1 \times \vec{a}_2 | \quad (3.8)$$

$$A^* = a_1^* a_2^* \sin \gamma^* = | \vec{a}_1^* \times \vec{a}_2^* | . \quad (3.9)$$

If an adsorbate structure with the base vectors \vec{b}_1 and \vec{b}_2 is present on the substrate lattice, the two lattices \vec{a} and \vec{b} are connected by $\vec{b} = M\vec{a}$, that is:

$$\vec{b}_1 = m_{11}\vec{a}_1 + m_{12}\vec{a}_2 \quad (3.10)$$

$$\vec{b}_2 = m_{21}\vec{a}_1 + m_{22}\vec{a}_2. \quad (3.11)$$

The same applies to the reciprocal lattice. m_{ij}^* can be deduced from the diffraction pattern.

The Ewald construction

The principle of a LEED experiment is shown in figure 3.7. The radius of the *Ewald* circle is $1/\lambda$. Lines are drawn through the points of the reciprocal lattice perpendicular to the surface leading to lattice rods. The intersection points of the rods with the Ewald circle determine the directions of the scattered beams. The direction of the incident beam is characterised by the unit vector \vec{k}_0 and the directions of the interference maxima by the unit vectors \vec{k} , which can be determined by the *Laue* conditions:

$$\vec{a}_1 \cdot (\vec{k} - \vec{k}_0) = h_1 \lambda \quad (3.12)$$

$$\vec{a}_2 \cdot (\vec{k} - \vec{k}_0) = h_2 \lambda \quad (3.13)$$

with $(h_1, h_2) = \text{integer}$.

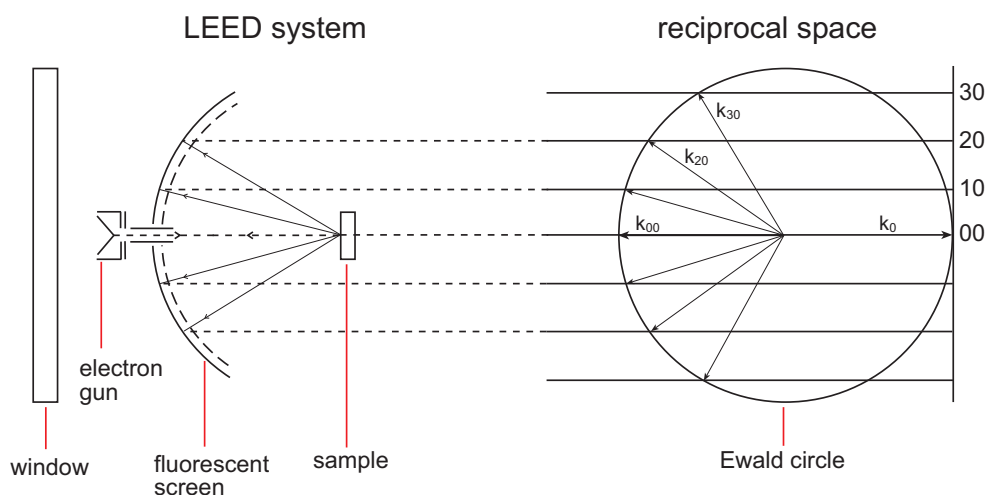


Figure 3.7: Scheme of the relationship between LEED pattern and K space.

3.2.4 The LEED-experiment

A LEED system consists of two components: an electron gun for the formation of a parallel and monoenergetic electron beam with energies from 5 to 500 eV and a detector for the elastically scattered electrons. A reverse view four-grid LEED optics with a fluorescent screen serves as a detector. The pictures of the LEED patterns were taken with a digital camera and handled with common image editing software (*Adobe Photoshop CS, Paint Shop Pro 7*).

3.3 Scanning tunneling microscopy (STM)

3.3.1 STM: theoretical background

The invention of the scanning tunneling microscope by Binnig and Rohrer in 1983 was awarded with the Nobel prize in physics in 1986. Since then, the number of STM investigations in various fields, such as surface science, biology and lithography, has increased exponentially.

The scanning tunneling microscope produces 3-dimensional images of surfaces

3.3 Scanning tunneling microscopy (STM)

and is able to resolve single atoms. The principle is rather straightforward and makes use of the tunneling effect; a fine metal tip is approached to the surface until the tunnel current starts to flow (surface–tip distance ≤ 1 nm). The tip is then moved over the surface in x- and y-direction by means of a piezoelectric drive, whereas the tunnel current and thereby the distance between STM tip and surface is kept constant (constant current mode). The modulator signal yields a direct image of the surface. The scanning tunneling microscope can even be used in the liquid phase, when the surface–tip distance is chosen smaller than the size of the liquid–molecules. Apart from the topography of the surface, information about the electron density distribution and the work function is contained in the images.

The physical basis of the STM is the quantum mechanical tunneling effect; it occurs between the STM tip and the sample, which are separated by a potential barrier. An approximation with $eV \ll \Phi$ yields the following relation for the current density j :

$$j \sim \frac{\sqrt{\Phi}}{s} \cdot V \cdot \exp(-k\sqrt{\Phi} \cdot s) \quad (3.14)$$

with the effective work function $\Phi = \frac{1}{2}(\Phi_1 + \Phi_2)$, the applied Voltage V , the tunneling distance s and a constant k . The current density j depends strongly on the distance s and the work function ϕ . A change in the distance of $\Delta s = 0.1$ nm induces an increase of the tunnel current by a factor of 10. Typical working parameters for metal surfaces are: $V = 0.1$ V, $I = 1$ nA at $\Phi = 4$ eV.

STM images can be recorded in two different modes:

- The tip distance is changed during the scanning process in order to keep the current j constant (*constant current mode*).
- The tip distance is held constant and the change in the tunnel current is recorded (*constant height mode*). This mode can only be used for very flat surfaces.

Figure 3.8 shows a schematic that illustrates the basic principle and the primary components of a scanning tunneling microscope.

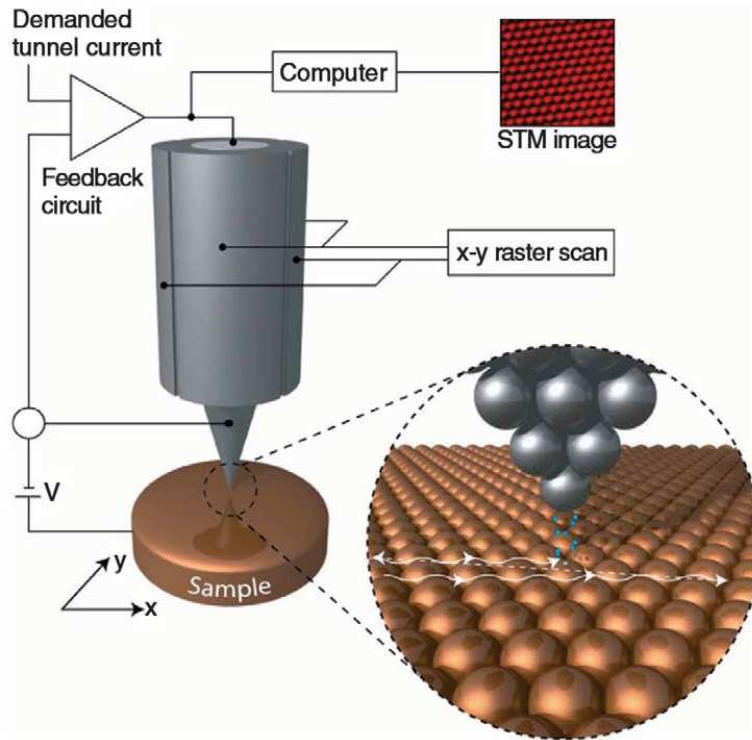


Figure 3.8: Schematics illustrating the basic operational principle and the primary components of an STM. Taken from reference [61].

3.3.2 The STM set-up

The STM images, which are presented in this thesis, were recorded within the scope of S. Schwede's diploma thesis [62]. The experiments were performed in a second UHV recipient equipped with a scanning tunneling microscope from *Danish Micro Engineering (DME)* and (Pt70/Ir30) tips were used. The presented images were taken in the constant current mode.

3.4 Surface chemical composition studied by Auger electron spectroscopy (AES)

3.4.1 The Auger process

If a solid is irradiated with an electron beam having energies from 1 keV to 10 keV, the atoms can be ionized due to the excitation of electrons from inner shells. The ion may relax by filling the hole with an electron of higher energy, followed by different processes:

- The excess energy is emitted in the form of electromagnetic radiation ($\Delta E = h \cdot \nu$).
- The excess energy is transmitted in a radiationless process to another electron, which then leaves the atom with a characteristic kinetic energy E_{kin} (*Auger effect*).

The Auger process is dominated by electrostatic forces, which are induced by the interaction of the electron cloud with the electron hole close to the core. The kinetic energies of Auger transitions are characteristic for a given atom. Three electronic states take part in the Auger process. At first, an inner shell is ionised, followed by an internal transfer of an outer electron to fill the hole. The resulting energy is then transmitted to the Auger electron. All three electronic states therefore contribute to the kinetic energy of the Auger electron.

$$E_{kin} = E_1 - E_2 - E_3 \quad (3.15)$$

with E_1 = binding energy of the core electron prior to ionisation, E_2 = binding energy of the outer electron and E_3 = binding energy of the Auger electron. For a quantitative analysis of the energies, also the work function of the analyzer has to be taken into account.

If an Auger process is induced in a solid, the Auger electrons are emitted from

the valence band. In this case, the work function of the solid has to be applied additionally to the ionisation energy of the electron. For atoms with high atomic numbers Z , many different Auger transitions are possible. They are named after the shells, from which the three electrons originate (KLL, LMM, MNN etc.).

The excitation probability for an Auger transition depends, among other things, on the atomic number of the atom. As the emission of an Auger electron competes with the emission of x-rays, the following equation results for the Auger yield:

$$Y_A = \frac{P_A}{P_A + P_x} \quad (3.16)$$

with P_A : probability for the emission of an Auger electron and P_x : probability for the emission of x-rays. For light atoms, the Auger process dominates while the x-ray process gains importance for heavier atoms ($Z > 32$). The cross section of the Auger emission is roughly proportional to $3 \cdot E_1$. In this work, a primary electron energy of $E_p = 2500 \text{ eV}$ was used.

3.4.2 The intensity of the Auger signal

The number of emitted Auger electrons is directly proportional to the Auger intensity. As electrons are also emitted from deeper layers, the mean free path of the electrons in the solid has to be considered. For a homogeneous adsorbate layer with the thickness d , the following correlation applies for the decrease of the substrate Auger signal:

$$I_S(d) = I_S^0 \cdot \exp\left(-\frac{d}{\lambda_A \cdot \cos \alpha}\right). \quad (3.17)$$

with I_S^0 = intensity of the substrate transition prior to adsorption, d = thickness of the adsorbate layer, λ = mean free path in the adsorbate layer and α = angle between the surface normal of the crystal and the analyzer. The increase of the adsorbate signal follows:

$$I_A(d) = I_A^0 \cdot \left(1 - \exp\left(-\frac{d}{\lambda_A \cdot \cos \alpha}\right)\right). \quad (3.18)$$

In solids, the scattered electrons also contribute to the excitation of Auger transitions and therefore increase the cross-section. The inelastic mean free path can be calculated via the equation of Tanuma, Powell and Penn [63, 64].

By recording Auger spectra during the preparation of an adsorbate film on a surface and plotting the signal intensities against the time or against each other (with constant preparation conditions), one can, for example, obtain information on the growth mechanism of the film:

Frank-van der Merwe-growth yields linear plots for the substrate and the adsorbate signal. The gradient changes strongly with the completion of each layer due to the abrupt change of the inelastic mean free path (IMFP): The graph exhibits kinks.

Three-dimensional growth (Volmer-Weber) leads to lower and gradually beginning changes in the substrate signal due to the weaker shielding. The graph complies with a decreasing exponential function.

Stranski-Krastanov growth shows a linear intensity/time correlation in the beginning and changes to an exponential progression as the transition to three-dimensional growth sets in[37].

3.4.3 The cylindrical mirror analyzer (CMA)

In our experiments, mostly a cylindrical mirror analyzer was used for the Auger measurements. The CMA is an energy-dispersive analyzer. An electrical field of cylindrical symmetry is created by a potential U_a , which is applied between the two coaxial cylindrical electrodes. The inner cylinder is usually grounded, while the outer one is held at a negative potential. The electrons enter the analyzer through the circular entrance and are deflected towards the inner cylinder depending on their kinetic energy. Electrons with an energy $e \times U_e$ pass through

the exit slit onto the collector. U_e/U_a is usually between 1.5 and 2 and remains constant over a relatively wide range of energies. In our set-up, Lock-in technology was used to obtain derivated spectra, which were then fed into the computer via a measuring board and recorded by means of a LabView program. The energy range was calibrated according to the known Auger energies from NIST [65] and reference [66]. The spectra were taken in the centre of the crystal (beam diameter ≈ 3 mm); test measurements on other spots did not show differences in the spectra.

3.5 Temperature-programmed desorption (TPD)

3.5.1 The data evaluation

Temperature-programmed desorption provides information about the binding state of adsorbate molecules on surfaces. Measured physical properties are the activation energy for desorption⁵ ΔE_{des}^* , the frequency factor ν and the desorption order n . From the TPD peak area, in addition the adsorbate-uptake of the surface can be deduced.

Desorption processes can be described by the usual equations of reaction kinetics. The rate law of a desorption reaction is:

$$-\frac{d[A]}{dt} = k \cdot [A]^n \quad (3.19)$$

with the adsorbate concentration on the surface $[A]$ and the rate constant k . The temperature dependence of the rate constant k is described by the *Arrhenius* equation:

$$k = k_0 \cdot \exp\left(-\frac{\Delta E_{des}^*}{RT}\right). \quad (3.20)$$

⁵The activation energy for desorption is also called desorption energy in the following.

3.5 Temperature-programmed desorption (TPD)

A replacement of the surface concentration $[A]$ with σ and the frequency factor k_0 with ν results in the *Wigner–Polanyi* equation for the desorption rate:

$$-\frac{d\sigma_i}{dt} = \nu_n \cdot \sigma_i^n \cdot \exp\left(-\frac{\Delta E_{des}^*}{RT}\right). \quad (3.21)$$

The derivative of the rate with respect to the temperature is zero at the temperature of the desorption maximum (T_{max}):

$$\frac{d\left(-\frac{d\sigma_i}{dt}\right)}{dT} = 0 \quad \text{for} \quad T = T_{max}, \quad (3.22)$$

which results in the following relation (derived from the *Wigner–Polanyi* equation):

$$\frac{\Delta E_{des}^*}{RT_{max}^2} = \frac{n \cdot \nu_n}{\beta} \cdot \sigma_i^{n-1} \cdot \exp\left(-\frac{\Delta E_{des}^*}{RT_{max}}\right) \quad (3.23)$$

with the heating rate β . ΔE_{des}^* , n , and ν are assumed to be coverage (σ_i) independent. For first-order desorption ($n = 1$) results:

$$\frac{\Delta E_{des}^*}{RT_{max}^2} = \frac{\nu_n}{\beta} \cdot \exp\left(-\frac{\Delta E_{des}^*}{RT_{max}}\right). \quad (3.24)$$

T_{max} is coverage-independent for first-order desorption. The activation energy of desorption ΔE_{des}^* can be calculated directly from T_{max} by the *Redhead* approximation [67]:

$$\Delta E_{des}^* = RT_{max} \left(\ln \frac{\nu_1 \cdot T_{max}}{\beta} - 3.64 \right). \quad (3.25)$$

Here, the frequency factor is usually chosen as $\nu_1 = 10^{13} \text{ s}^{-1}$.

Several methods for the determination of the frequency factor, the desorption energy and the desorption order have been developed. A comparison can be found in an article by de Jong [68].

Information about the desorption order can also be gained from the shape of the desorption peak. First-order desorption signifies molecular (associative) desorption, the rate-determining step is the cleavage of the adsorbate–substrate–bond. The desorption peak is asymmetric and the desorption temperature depends on

the heating rate.

Dissociative adsorption yields associative desorption with the recombination of the individual particles as the rate-determining step. The desorption reaction is therefore of second-order and the desorption peak is symmetric. The desorption temperature decreases with increasing coverages in a characteristic manner.

Desorption from multilayers ($n = 0$) results desorption peaks with a common rising edge (zero-order desorption).

3.5.2 The experimental set-up

During a desorption experiment gas desorbs also from the rear of the crystal, the walls of the UHV system and the other system parts that get warm, especially the sample holder. In order to eliminate these background contributions, the crystal was positioned closely in front of a small nozzle ($\varnothing \approx 1.5$ mm) prior to the desorption experiment. The desorbing molecules pass the nozzle and enter a small separate chamber, which contains the quadrupole mass spectrometer (QME200, *Balzers*) and is differentially pumped by a turbomolecular pump backed by a diaphragm pump. A constant nozzle-crystal distance was used for all TPD experiments ($d < 0.1$ mm). The crystal was positioned further apart from the nozzle during the gas exposition time to avoid shielding of the surface⁶.

A type C thermocouple (W-5%Re/W-26%Re) was applied for the temperature measurement in our previous experiments on the same system [18]. Although the type C thermocouple enables the measurement of temperatures up to 2593 K and is therefore very useful for the preparation of the high-melting rhenium substrate, it is not applicable for the accurate measurement of temperatures below 300 K. Furthermore, the derivative of the thermoelectric voltage with respect to the temperature (*Seebeck* coefficient) is very low compared to the commonly used

⁶Blank experiments revealed that a significant amount of gas molecules ($\approx 60\%$) is blocked by the nozzle.

3.5 Temperature-programmed desorption (TPD)

type K thermocouple (Ni/Cr-Ni/Al).

Figure 3.9 compares the two thermocouples regarding the electromotive volt-

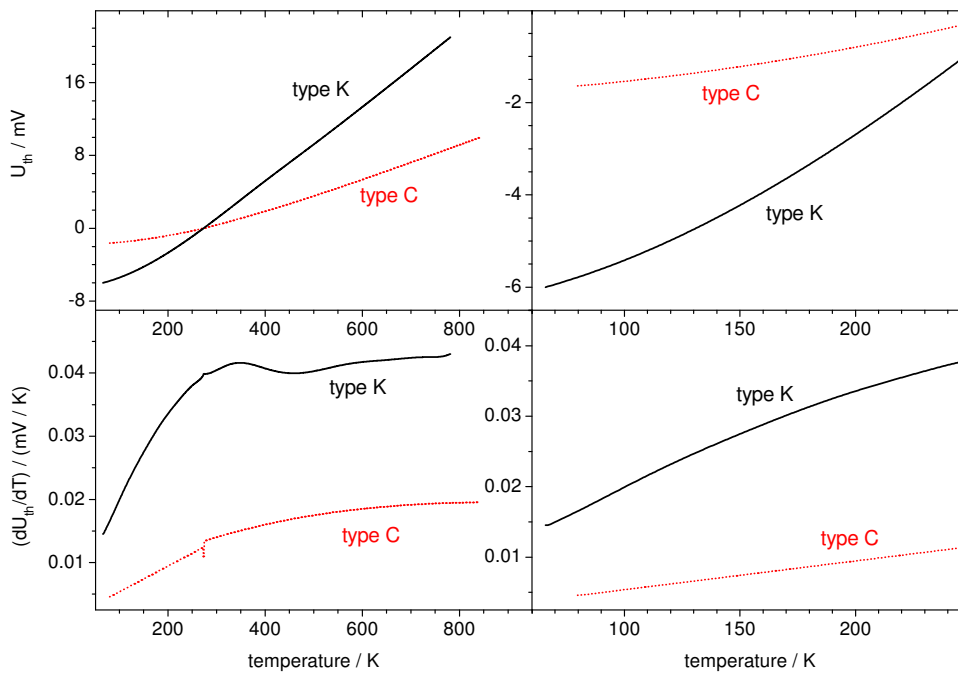


Figure 3.9: Comparison of the thermoelectric voltage (upper plots) and the *Seebeck*-coefficient (lower plots) of type K and type C thermocouples [65, 69].

age and the *Seebeck* coefficient (dU_{th}/dT). Because of the comparatively high temperature uncertainty due to the low *Seebeck* coefficient of the type C thermocouple (especially below 300 K), the preparation of the $\text{Re}(10\bar{1}0)$ surface was adapted such that only temperatures suitable for the use of a type K thermocouple ($T < 1645 \text{ K}$) were applied. The preparation of the Re surface at around 1300 K left a small amount of oxygen residuals on the surface. These traces were negligible for the rutile film preparation, because in this case the Re surface is exposed to more than 100 L O_2 in the first step anyway⁷. The film growth was

⁷Details about the rutile film preparation will be discussed in chapter 4.

not affected by the lower annealing temperature for the Re crystal preparation.

TPD spectra can only be evaluated correctly with respect to the desorption temperature and the peak intensities, if a constant heating rate is applied. Although the thermoelectric voltage versus temperature function is almost linear for the type K thermocouple above 300 K, it deviates significantly from linearity below 300 K. The *Seebeck* coefficient doubles from 60 to 300 K (see figure 3.9). It is therefore essential to directly regulate the temperature instead of the thermoelectric voltage. Figure 3.10 shows the resulting temperature and thermoelectric voltage plots of a regulation of the thermoelectric voltage (figure 3.10a) and a direct regulation of the temperature (figure 3.10b), respectively. An ice-water mixture was used as a cold junction reference point. The corrected thermoelectric voltage was then read into the PC with an analogue–digital input board (*Keithley*) with internal amplifier. The thermoelectric voltage was transferred into the respective temperature by means of a LabView program [65] and a proportional voltage was fed into an analogue PID⁸ controller (*Hertz–Regler*), which controlled the high–voltage of the electron bombardment heating. The underlying controlling equation for a PID regulation is:

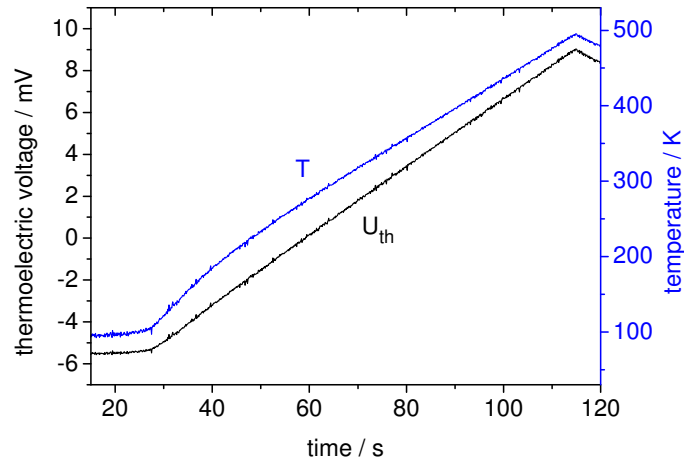
$$U_{out} = U_{out,0} + \alpha_P \Delta T + \alpha_I \sum \Delta T + \alpha_D \Delta(\Delta T) \quad (3.26)$$

with the output voltage of the controller U_{out} , the initial output voltage $U_{out,0}$, the empirically chosen control factors α and the temperature difference ΔT between the measured temperature and the desired temperature.

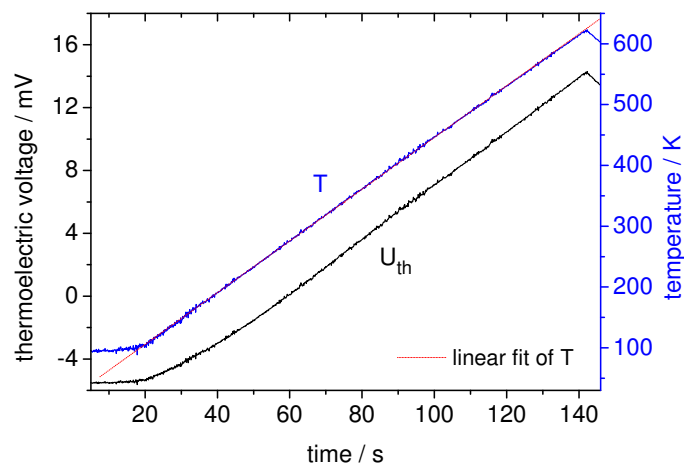
The displayed TPD spectra in this thesis were neither smoothed nor background subtracted or changed otherwise. The mass spectrometer signal was fed into a 16bit analogue–digital board and saved together with the thermoelectric voltage, the measured temperature and the background pressure. The gas exposure in the present thesis is defined in the unit L = Langmuir with $1 \text{ L} = 1 \times 10^{-6} \text{ mbar} \cdot \text{s}$ in

⁸PID: proportional–integral–derivative.

3.5 Temperature-programmed desorption (TPD)



(a) Plot of the substrate temperature T and the thermoelectric voltage U_{th} versus the time when the thermoelectric voltage is controlled.



(b) Plot of the substrate temperature and the thermoelectric voltage versus the time when a direct temperature regulation is applied.

Figure 3.10: Comparison between the heating rate when the thermoelectric voltage U_{th} (a) and the temperature T (b) is controlled, respectively.

contrast to the common definition of $1 \text{ L} = 1 \times 10^{-6} \text{ Torr} \cdot \text{s}$.

3.6 Adsorbate-induced work function change ($\Delta\Phi$)

3.6.1 $\Delta\Phi$ – Theoretical Background

The work function of a metal is defined as the minimum energy that is required to remove one electron from the metal to a distance of $\approx 10^{-6} \text{ m}$ outside the metal, where the image potential has declined to zero.

The total work function can be split into a surface and a bulk dependent part. The surface dependent part is induced by the asymmetric forces in the surface region, which lead to a spill-out of the electron gas and therefore an asymmetric charge distribution on the surface (*dipole layer*). The surface charge can be compensated within a few atomic distances in metals, which provide a high density of mobile charges. In semiconductors and insulators, which possess a lower amount of free charges, the dipole layer gets thicker (1 – 1000 nm for semiconductors and the whole sample diameter for insulators).

The work function can be expressed as:

$$\Phi = E_{vac} - (E_N - E_{N-1}) = E_{vac} - E_F \quad (3.27)$$

with the Fermi energy E_F , the energy of the system in the initial state with N electrons E_N , the energy of the system in the final state with $N-1$ electrons E_{N-1} and the energy of the vacuum level far from the surface E_{vac} . For semiconductors, this equation changes to:

$$\Phi = E_{vac} - E_F = \chi + (E_C - E_F)_{bulk} - e\Delta V_s \quad (3.28)$$

$$= I - (E_F - E_V)_{bulk} - e\Delta V_s \quad (3.29)$$

with the electron affinity χ as distance between conduction band and vacuum level, the ionisation energy I as distance between valence band and vacuum level,

3.6 Adsorbate-induced work function change ($\Delta\Phi$)

the band bending ($e\Delta V_s$) and the energies of the band edges E_C (conduction band) and E_V (valence band).

Adsorption and desorption of molecules as well as defect formation (especially on semiconductors) lead to a change in the charge distribution on the surface, which consequently yields a change in the work function. This work function change $\Delta\Phi = \Phi_{ad} - \Phi_0$ with the work function of the covered surface Φ_{ad} and the work function of the bare surface prior to adsorption Φ_0 depends on the dipole moment μ_{ad} , the number of adsorbed molecules N_{ad} and the coverage Θ and can be expressed by the *Helmholtz* equation:

$$\Delta\Phi = 4\pi \cdot \mu_{ad} \cdot N_{ad} \cdot \Theta \cdot \frac{1}{4\pi\epsilon_0}. \quad (3.30)$$

The work function change can be positive or negative depending on the adsorption site, the dipole direction and the charge transfer.

3.6.2 The self-compensating Kelvin probe method

The adsorbate induced work function change was studied by means of the self-compensating Kelvin probe method. This method makes use of the electric field that exists between two materials with different work functions in thermal equilibrium and can be measured when the distance between the materials is very small. For the Kelvin method, the distance is changed periodically and thereby modulates the capacity C between the studied material and an inert electrode, which yields a modulation of the charge Q_{in} :

$$Q_{in} = C \cdot \Delta V_{12}. \quad (3.31)$$

This charge variation can be measured as alternating current via a Lock-in-amplifier. If an additional direct voltage V_{Bias} is applied, the current can be zeroed for $V_{Bias} = \Delta V_{12}$:

$$I = \frac{dQ_{in}}{dt} = \frac{dC}{dt} \cdot (\Delta V_{12} - V_{Bias}). \quad (3.32)$$

This enables the determination of ΔV_{12} via V_{Bias} . If a self-compensating Lock-in technology is applied, the work function change during adsorption can be directly recorded.

3.6 Adsorbate-induced work function change ($\Delta\Phi$)

4 Structural aspects

4.1 The rhenium($10\bar{1}0$) substrate

In the present work, a rhenium crystal with a ($10\bar{1}0$) surface served as an electrically and thermally conducting substrate. The crystal was cylindrically shaped with a diameter of 10 mm and a thickness of 1.5 mm. Prior to the preparation of titania films, the crystal was cleaned by sputtering with argon ions (1000 V, $I_{\text{sample}} = 5 \mu\text{A}$). Subsequent to the sputtering, the surface was annealed to 1400 K to heal out defects. A higher temperature could not be applied due to the use of a type K thermocouple (see section 3.5). Sputtering and subsequent annealing to 1400 K for 30 minutes resulted in a surface that stills contains traces of oxygen. However, in the first step of the following titania film preparation, an oxygen superstructure is intentionally produced by exposure of the rhenium crystal to 120 L of oxygen, which makes the initial oxygen traces certainly acceptable.

Figure 4.1a shows a LEED pattern of the freshly prepared Re($10\bar{1}0$) surface prior to the generation of the oxygen superstructure. An STM image of the clean rhenium surface is displayed in figure 4.1b. In both figures, the rectangular unit mesh of the Re($10\bar{1}0$) surface is clearly visible. The LEED patterns as well as the STM images were calibrated using the known lattice parameters of Re($10\bar{1}0$) [43]. Auger electron spectra were routinely taken after the cleaning procedure to ensure the chemical purity of the surface (figure 4.4 may serve as an example).

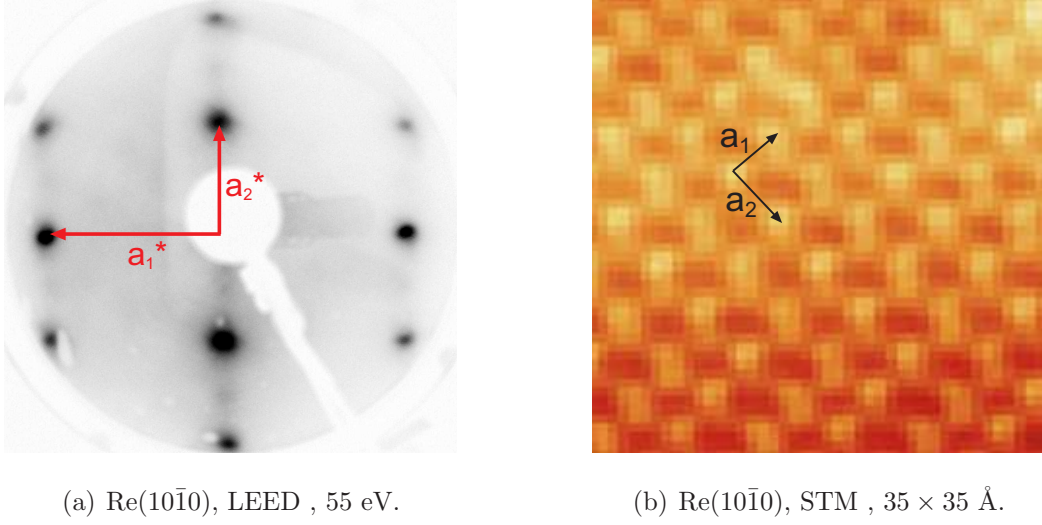


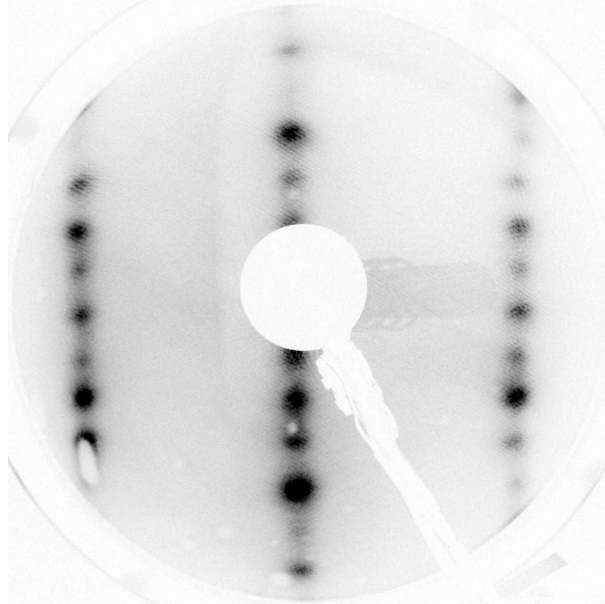
Figure 4.1: LEED pattern (55 eV) and STM picture ($I = 0.1 \text{ nA}$, $U = 0.021 \text{ V}$) of the clean rhenium($10\bar{1}0$) surface.

4.2 Preparation and characterization of the oxygen $(1 \times 3)\text{-}2\text{O}$ superstructure

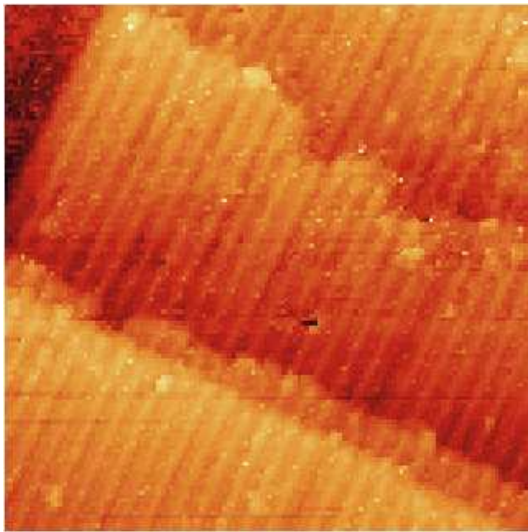
Oxygen induces different coverage-dependent superstructures on the Re($10\bar{1}0$) surface. The $(1 \times 3)2\text{O}$ structure represents the saturation structure and forms at oxygen coverages larger than $2/3$. Lenz *et al.* studied the O/Re($10\bar{1}0$) system by means of LEED, oxygen TPD, $\Delta\Phi$, ARUPS (angle resolved ultraviolet photoelectron spectroscopy) and HREELS (high-resolution electron energy loss spectroscopy) [70].

In order to prepare the $(1 \times 3)2\text{O}$ structure, the rhenium crystal was annealed to 900 K in an oxygen atmosphere of 2×10^{-6} mbar for 60 s. The oxygen flux was turned off when the crystal had cooled down to 500 K. A LEED pattern of the $(1 \times 3)2\text{O}$ superstructure is shown in figure 4.2a, the associated STM images in figures 4.2b,c [62]. Figure 4.4 shows an Auger spectrum of the $(1 \times 3)2\text{O}$ phase.

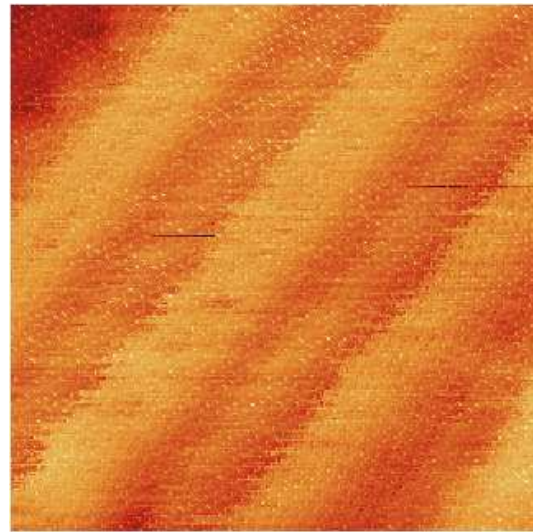
At the time of the first study by Lenz *et al.* [70] STM images were not available



(a) $(1 \times 3)2O$, LEED, 55 eV.



(b) $(1 \times 3)2O$, STM, $300 \times 300 \text{ \AA}$.



(c) $(1 \times 3)2O$, STM, $35 \times 35 \text{ \AA}$.

Figure 4.2: LEED pattern (electron energy = 55 eV) and STM images ($I = 0.3 \text{ nA}$, $U = 0.5 \text{ V}$) of the $(1 \times 3)2O$ superstructure on $\text{Re}(10\bar{1}0)$.

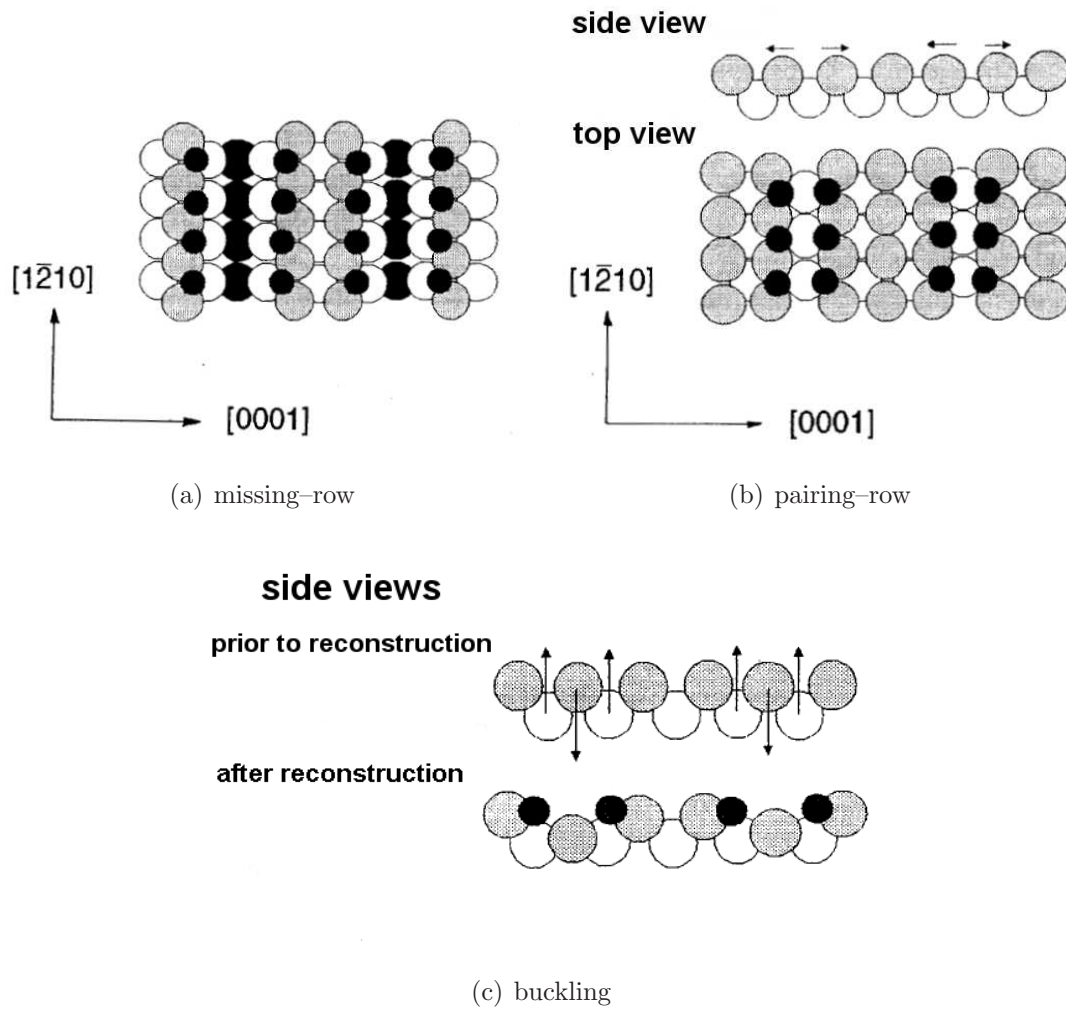


Figure 4.3: Schemes of the three proposed surface models for the (1×3) oxygen superstructure on $\text{Re}(10\bar{1}0)$ taken from Jörg Lenz' PhD Thesis [71]; grey and white circles = rhenium atoms, black circles = oxygen atoms.

and the structure of the (1x3) oxygen phase could not be ultimately resolved. However, the results of the LEED and $\Delta\Phi$ studies clearly indicated that oxygen induces a reconstruction of the $\text{Re}(10\bar{1}0)$ surface. The (1x3) periodicity followed from the LEED patterns. Oxygen TPD experiments provided information about the associated oxygen coverage, and ARUPS proved, that the adsorbate geometry within the unit mesh was of C_{2v} -symmetry, with two oxygen atoms per unit cell. HREELS yielded a C_s or C_1 adsorption site for the O atoms.

Based on these facts, three different structure models were suggested [71], namely the ‘missing-row’ reconstruction, the ‘pairing-row’ reconstruction and the ‘surface buckling’ model (these models are illustrated in figure 4.3). In the ‘missing-row’ model (Fig. 4.3a), every third Re row of the topmost layer is missing. The oxygen adsorption site has C_s -symmetry. The ‘pairing-row’ reconstruction shows a lateral displacement of the Re atoms in $[0001]$ direction (figure 4.3b). A deep corrugation of the surface results from the ‘buckling’ model (figure 4.3c).

Considering in addition the recently obtained STM images [62] in figure 4.2b,c, the ‘missing-row’ model can apparently be excluded. The STM pictures exhibit bright and dark lines in $[1\bar{2}10]$ -direction. At a first glance, all three reconstruction models could apply. However, a closer inspection of the STM images reveals thin bright lines in the middle of the thick dark lines (see figure 4.2c), which indicate the existence of protrusions in the middle of the trenches. The ‘missing-row’ reconstruction should show even darker features in the middle of the dark lines, hence we can exclude this type of reconstruction. According to reference [72], oxygen is usually imaged as a depression in STM. This behaviour is believed to be due to the low density of states near the Fermi level around the oxygen atom, compared to a metal atom.

The ‘pairing-row’ reconstruction would only comply with the STM images, if the oxygen atoms were imaged as protrusions. Furthermore, the ‘pairing-row’ model

is unfavourable from an energetic point of view, because it would lead to strong repulsive interactions between the adjacent oxygen atoms, which makes it very implausible, especially for reconstructions with low oxygen coverages (e.g. (1×4) , (1×5)).

The ‘buckling’ model, on the other hand, seems to be entirely consistent with the STM pictures, because it can explain both features, the oxygen atoms being not imaged at all and being imaged as a depression (compare figures 4.2c and 4.3c).

Altogether, we suppose that the $(1 \times 3)2\text{O}$ superstructure, which is induced by oxygen on the $\text{Re}(10\bar{1}0)$ surface under the preparation conditions, reflects a reconstruction of the surface of the buckling type. This very surface is henceforth used as a template for growing the titania films described in the following.

4.3 The ‘art’ of growing $\text{TiO}_2(011)-(2 \times 1)$ films; structure and morphology

The rutile films were prepared onto the $(1 \times 3)2\text{O}$ superstructure described above by physical vapour deposition of titanium in an oxygen atmosphere of 1×10^{-6} mbar at a sample temperature of 900 K. The shutter of the EFM3 Ti evaporator was opened for 5 minutes at a flux of 50 nA followed by 3 minutes of annealing in oxygen at 900 K with a closed shutter. The process was then repeated as often as necessary to achieve the desired film thickness. After the last deposition run, the film was annealed for another 8 minutes in oxygen ($p(\text{O}_2) = 1 \times 10^{-6}$ mbar) at 900 K before the heating was switched off. The crystal was then allowed to cool down to 400 K before the oxygen supply was closed¹. The Ti flux was kept constant and calibrated by means of Auger electron–spectroscopy. Figure 4.4 shows Auger electron–spectra of the pure $\text{Re}(10\bar{1}0)$ surface, the $(1 \times 3)2\text{O}$ phase

¹This recipe was successfully introduced by D. Rosenthal [16, 17].

and a 24 MLE thick titania film².

As mentioned in section 4.5, the plot of the differentiated Auger signal intensities

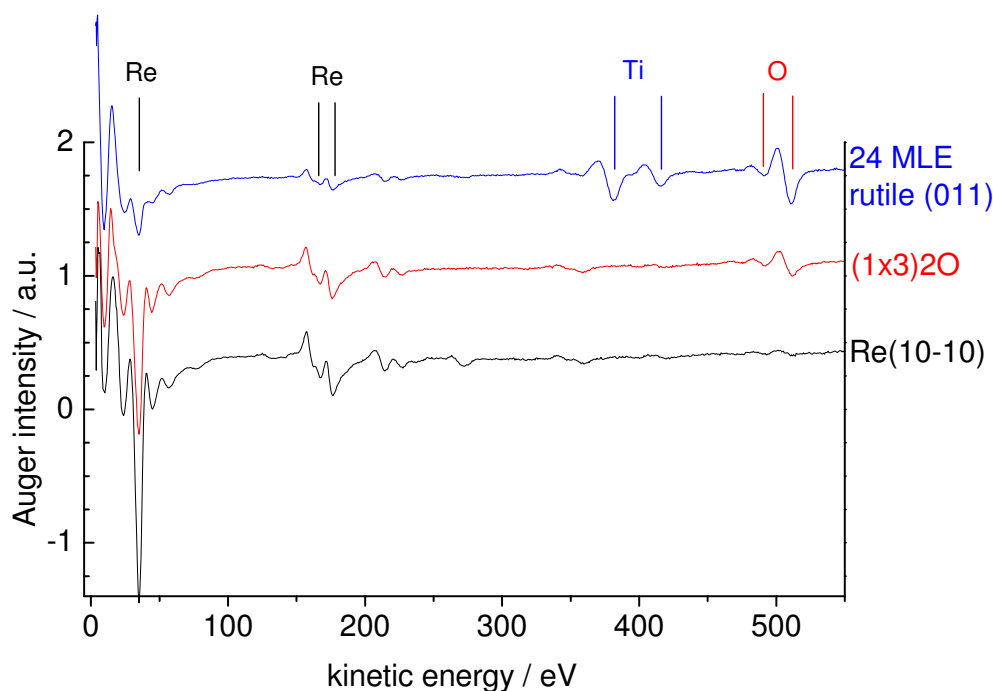


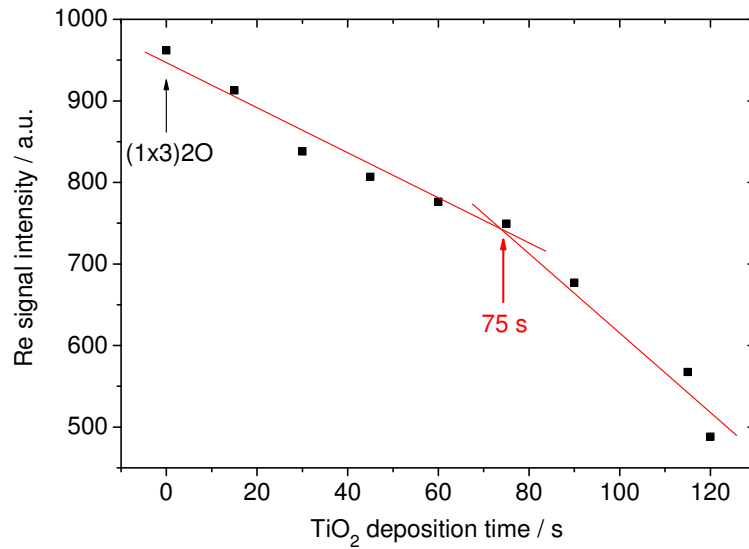
Figure 4.4: Auger electron–spectra of the bare rhenium($10\bar{1}0$) surface, the (1×3) oxygen phase and a 24 MLE thick rutile(011)- (2×1) film. The observed Auger signals can be assigned to rhenium (33, 168, 176 eV), oxygen (488, 510 eV) and titanium (386, 417 eV).

for the substrate and the adsorbate against the adsorbate deposition time exhibits information about the growth mechanism as well as the completion of a closed layer (= monolayer). Figure 4.5 presents such plots for the rhenium Auger signal at 33 eV (a) and the oxygen signal at 510 eV (b). The titanium signals are not intense enough to allow reliable conclusions in the submonolayer coverage range. The Re signal at 33 eV is the most intense Re signal and also the most surface sensitive one³. The starting point of the plot is the $(1\times 3)2O$ phase (0 s). Initially, the Re intensity decreases only slowly until a deposition time of 75 s is reached.

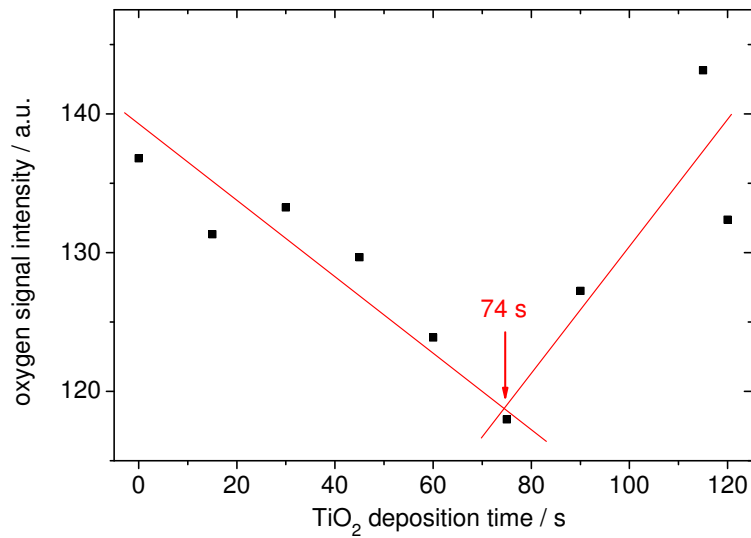
²Please refer to page 61 for an explanation of the abbreviation “MLE”.

³The mean inelastic free path of the Auger electrons depends on their kinetic energy [63, 64].

4.3 The 'art' of growing $\text{TiO}_2(011)-(2 \times 1)$ films; structure and morphology



(a) Plot of the rhenium Auger-intensity at 33 eV against the TiO_2 deposition time.



(b) Plot of the oxygen Auger-intensity at 510 eV versus the TiO_2 deposition time.

Figure 4.5: Development of the Auger intensities of the Re (33 eV) and the oxygen (510 eV) signal with increasing titania deposition time. Both plots exhibit breaks after a deposition time of ≈ 75 s.

Thereafter, the Re intensity drops faster with increasing TiO₂ deposition. This behaviour cannot easily be rationalized, because every additional adsorbate layer should yield a reduced decrease in the substrate (Re) signal. However, we have to keep in mind that the titania layer is deposited on top of the oxygen (1x3) structure, which itself induces a strong reduction of the Re Auger intensity prior to the film growth. Apparently, the oxygen structure is ‘filled’ with titanium atoms in a first step, prior to the growth of titania onto this first layer. This assumption is supported by the development of the oxygen Auger signal, which decreases first until ≈ 75 s and increases afterwards, suggesting that the oxygen structure is partly covered in the first layer. Only when the titania growth onto this first layer proceeds, the oxygen signal intensity rises again, because more oxygen is bound onto the surface in the form of titanium dioxide. From these considerations, a deposition time of 75 ± 5 s is derived for the completion of the first layer. This time interval is now defined as a monolayer (ML). The thickness of the titania films will henceforth be given in monolayer equivalents (MLE), which is the ratio of the deposition time and the time that is required to complete the first layer (75 s).

In figure 4.6c, the LEED pattern of a rutile film is shown, which was prepared by 30 minutes Ti evaporation (+ 23 minutes annealing) and has a thickness of about 24 MLE⁴. LEED patterns of the clean Re(10 $\bar{1}$ 0) surface (in this case with a faint c(2x4) oxygen superstructure, c.f. the remarks in section 4.1, first paragraph) and the (1x3)2O substructure are shown at the same electron energy (40 eV) for comparison. The LEED pattern of the titania film shows a pg(2x2) structure (related to the Re pattern). Accordingly, the area of the unit mesh in real space is four times the area of the Re(10 $\bar{1}$ 0) unit mesh. One further notes that the $(\pm\frac{1}{2}, 0)$ reflexes are missing. LEED patterns of higher electron energies demonstrate

⁴MLE (monolayer equivalent) is here defined as the amount of titanium dioxide that would correspond to one layer of rutile(011)-(2x1), if layer by layer growth conditions apply.

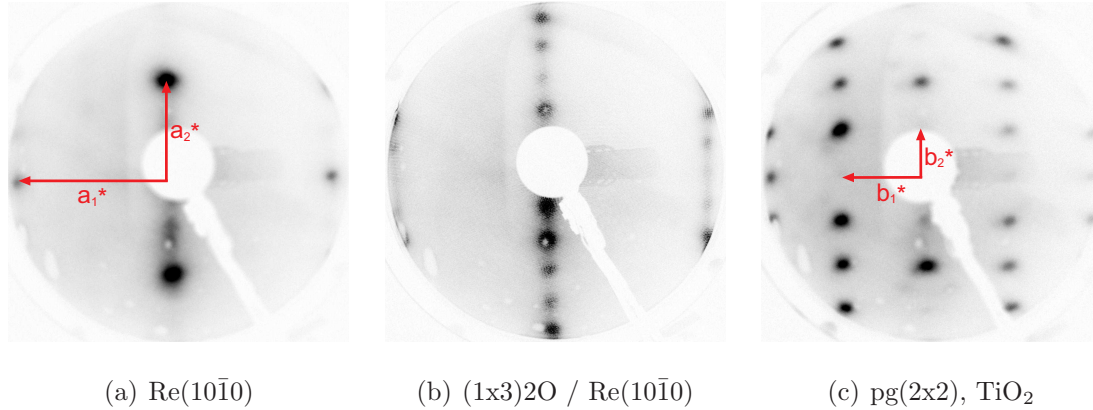


Figure 4.6: LEED patterns of the clean $\text{Re}(10\bar{1}0)$ surface, the $(1 \times 3)2\text{O}$ superstructure and the epitaxially grown TiO_2 film (thickness ≈ 24 MLE) taken at 40 eV.

that all $(n \pm \frac{1}{2}, 0)$ reflexes are systematically extinguished. According to the kinematic diffraction theory [73, 74, 75], these missing spots indicate the presence of a glide mirror plane in the surface. As far as the type of TiO_2 is concerned, it is worth mentioning, that additional, so called ‘running’, LEED spots appear for certain film thickness conditions thereby indicating facet formation. An analysis of the respective faceting features by D. Rosenthal [16, 17] revealed that two rutile(011)-(2x1) domains grow epitaxially on the $\text{Re}(10\bar{1}0)$ surface with two (2x1)-reconstructed facets. The other two facets of the islands consist of rutile (110) surfaces. This conclusion was confirmed by an X-ray diffraction experiment at the Berlin synchrotron facility BESSY [16] which also revealed that the films contain additional traces of (001) surface orientations. A detailed description of the respective structure analyses of our thin films can be found in previous publications [16, 17, 18].

As pointed out above, facet formation has been deduced from the LEED features of the thin TiO_2 films. The $\text{pg}(2 \times 2)$ structure is visible for the first time after deposition of about 3 MLE of rutile(011). After the growth of 12 MLE, the running LEED spots that are indicative of faceted surfaces, exhibit their maximum

intensity. Thereafter the respective intensity decreases with increasing film thickness, until the facet spots disappear after ca. 35 MLE. Consequently, thin films (thickness ≈ 12 MLE) are rough compared to thicker ones. Figure 4.7 presents STM images of a thin rutile film (12 MLE)(a,b) and a 24 MLE thick rutile film (c,d), measured by S. Schwede [62]. In 4.7d, the zig-zag structure on top of the rows is clearly visible and confirms the glide mirror symmetry of the film surface. The surface unit cell vectors in real space have a size of $\vec{b}_1 = 5.13 \pm 0.51 \text{ \AA}$ and $\vec{b}_2 = 9.28 \pm 0.93 \text{ \AA}$. Diebold *et al.* determined them to $\vec{b}_1 = 5.453 \text{ \AA}$ ($197.5\% \times \vec{a}_1(\text{Re})$) and $\vec{b}_2 = 9.168 \text{ \AA}$ ($205.7\% \times \vec{a}_2(\text{Re})$) [51]. The mismatch (f)⁵ adds up to $f(2a_1, b_1) = -0.01$ and $f(2a_2, b_2) = 0.03$, respectively, and remains well within the limits for epitaxy ($f \leq 0.1$).

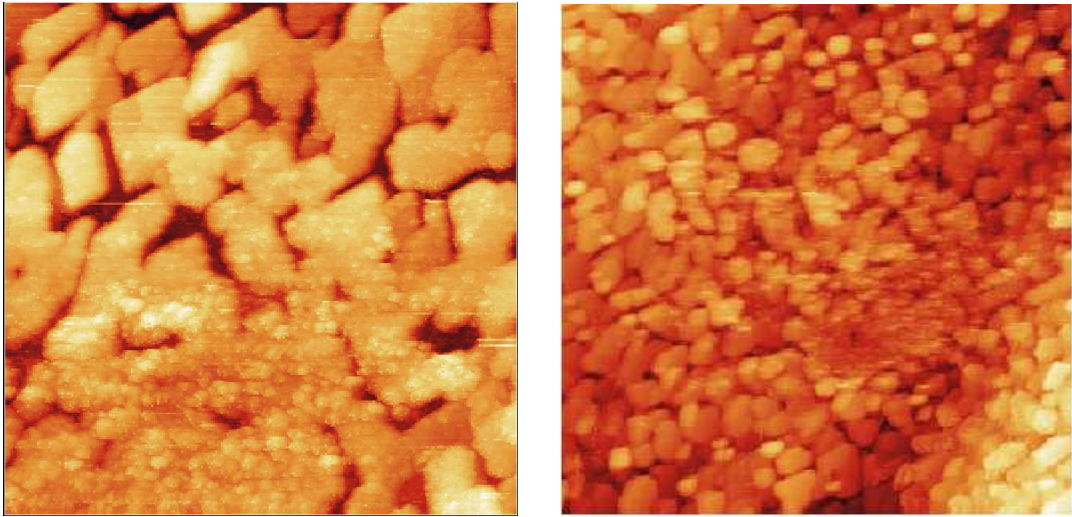
The STM images of the two different titania films clearly support the Stranski-Krastanov growth mechanism, which means that layer growth occurs for the first layer and is then followed by 3-dimensional island growth (see, for example, figure 4.7b). Please refer to S. Schwede's diploma thesis for further information about the STM pictures [62].

As mentioned above, the 'running' LEED spots, which can be used as a simple monitor of the surface roughness, indicate that thin films are rougher than thick ones. A comparison of the STM scans of the two films in figure 4.7 reveals that the islands agglomerate with increasing thickness thereby leading to a decrease of the associated facet spot intensities. Please note that the facet LEED spots disappear completely only when the films have reached a thickness of ca. 35 MLE. The thicker film in figure 4.7 is only 24 MLE thick and therefore still shows facet spots in LEED.

To summarize at this point, the film thickness can be taken as a straightforward monitor to prepare titania films and model catalysts with a defined roughness.

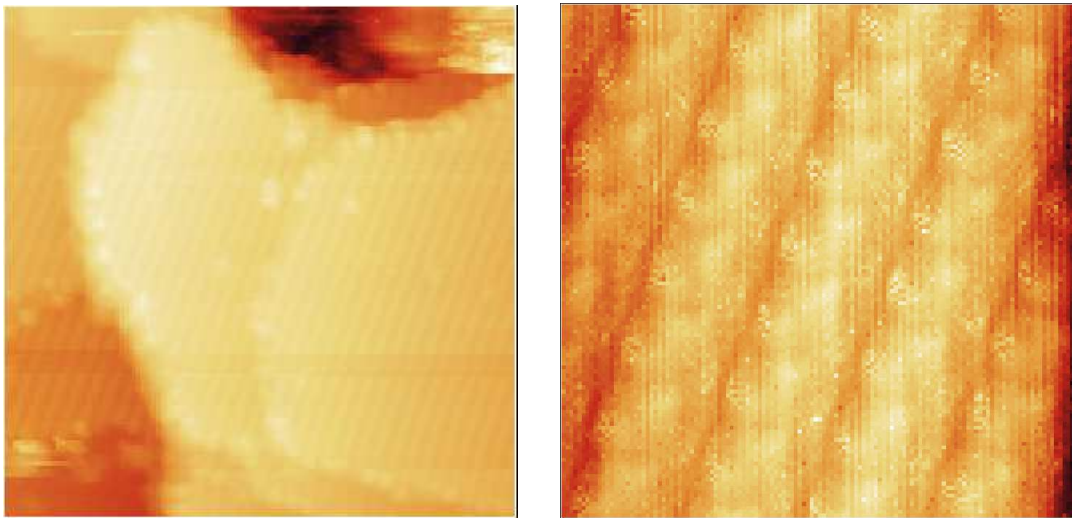
⁵The mismatch f can be calculated via $f = \frac{a_e - a_s}{(a_e + a_s)/2}$; see subsection 2.2.1.

4.3 The ‘art’ of growing $\text{TiO}_2(011)-(2 \times 1)$ films; structure and morphology



(a) $2000 \times 2000 \text{ \AA}$, thickness $\approx 12 \text{ MLE}$.

(b) $5000 \times 5000 \text{ \AA}$, thickness $\approx 12 \text{ MLE}$.



(c) $300 \times 300 \text{ \AA}$, thickness $\approx 24 \text{ MLE}$.

(d) $35 \times 35 \text{ \AA}$, thickness $\approx 24 \text{ MLE}$.

Figure 4.7: STM images of a ‘thin’ (a,b, $I = 0.3 \text{ nA}$, $U = 1 \text{ V}$) and a ‘thicker’ (c,d, $I = 2 \text{ nA}$, $U = 2 \text{ V}$) rutile $\text{TiO}_2(011)-(2 \times 1)$ film; a,b: thickness $\approx 12 \text{ MLE}$; c,d: thickness $\approx 24 \text{ MLE}$.

Films of this kind constitute an intermediate stage between flat rutile single crystal surfaces and polycrystalline titania powder. In this sense, studies on titania thin films possibly provide a means to close the “materials gap” in heterogeneous catalysis.

4.4 Preparation of partially Au-covered rutile $\text{TiO}_2(011)-(2 \times 1)$ films

The gold (Au) containing “model catalysts” were prepared by physical vapour deposition of Au onto 24 MLE thick rutile(011)-(2x1) films. A preparation scheme for the Au/rutile(011)-(2x1)/Re(10 $\bar{1}$ 0) samples is shown in figure 4.9. The gold evaporation was achieved via a home-made gold evaporator, which is described in section 3.3. The Au flux was kept constant by a temperature-dependent control of the heating current. The Au was deposited onto the rutile substrate at room temperature (= substrate temperature). For the CO/ Au/ rutile(011)-(2x1) TPD spectra that will be presented in section 6.1.1 the Au was accumulatively deposited onto the Au/rutile sample that was used before

Figure 4.8 shows Auger spectra of a bare (24 MLE thick) and a Au-covered rutile film (Au deposition time = 1200 s). Preliminary experiments with a quartz microbalance and Auger electron-spectroscopy, respectively, revealed that the Au deposition rate adds up to about 0.5 MLE per minute. One MLE is here defined as the amount of gold, whose weight is attributed to one layer of gold(111) by the quartz microbalance and which induces a sudden change in the slope of the Auger progression for Au deposition on Re(10 $\bar{1}$ 0). The Auger spectrum, which was obtained from a rutile(011)-(2x1) film with a Au coverage that corresponds to 1200 s deposition time (see figure 4.8), still shows clearly visible titanium and

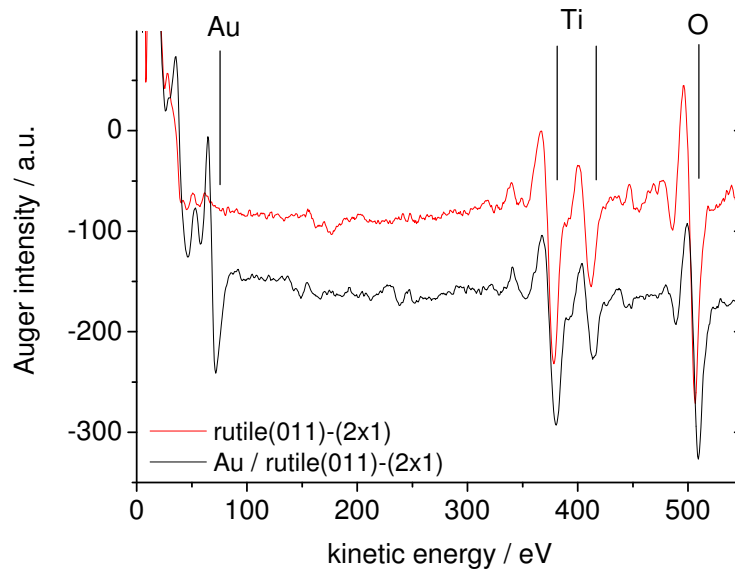


Figure 4.8: Auger electron-spectra of a bare rutile(011)-(2x1) film (thickness ≈ 24 MLE) and a partially gold-covered film (Au deposition time = 1200 s ≈ 10 MLE).

oxygen signals, although the nominal Au Coverage amounts to 10 MLE. This finding highly suggests a three-dimensional growth mode (Volmer-Weber) for the gold particles and is consistent with the current literature (see, for example, [76]).

The LEED patterns of the gold covered rutile films support the 3-dimensional growth mode, in that they reveal a high diffuse background, but visible TiO_2 reflexes for Au coverages up to 5 MLE. Preliminary STM images of high Au-coverage exhibit the growth of clusters as well (refer to figure .2 in the appendix for examples).

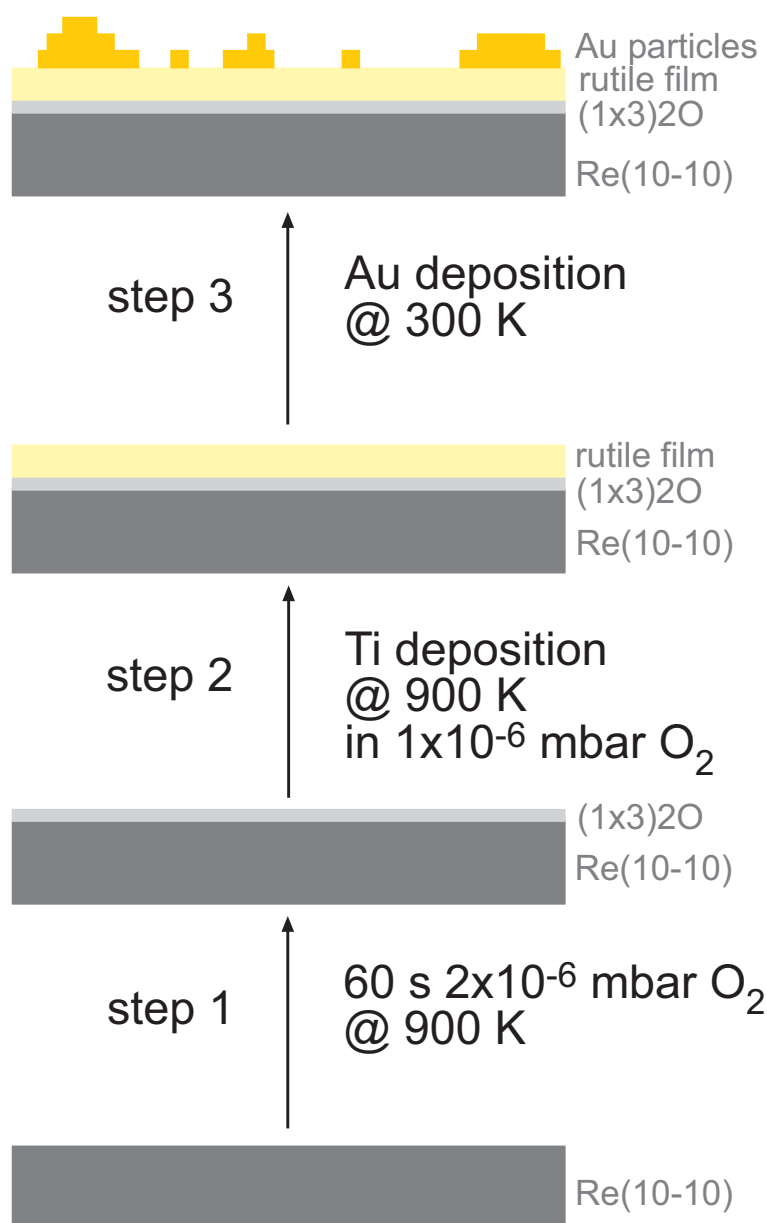


Figure 4.9: Scheme of the preparation procedure for the Au/rutile(011)-(2x1)/Re(10 $\bar{1}$ 0) model catalysts that were prepared and studied in the present thesis.

4.4 Preparation of partially Au-covered rutile $\text{TiO}_2(011)-(2 \times 1)$ films

5 Chemical reactivity of rutile

(011)-(2x1) films:

Adsorption of CO, CO₂ and H₂O

In the present thesis pure and gold-covered epitaxial rutile(011)-(2x1) films are explored from a catalytical point of view. In this respect, the chemical reactivity of the rutile films themselves is of particular interest: first, there is interest in the nature of the nucleation sites of subsequent gold deposition, and second, one would like to know the binding sites and binding strengths of the adsorbates that play a role in the photocatalytic activity of titanium dioxide. Third, the role of the binary system TiO₂ plus Au in the catalytic low-temperature CO oxidation deserves major attention. The adsorbates of interest are CO, O₂, CO₂ and H₂O. Since pure TiO₂ does not show any catalytic activity in the low-temperature CO oxidation, it is very important to know the differences in gas adsorption of the reaction educts and products between pure and Au covered films. Finally, CO is a well-studied molecule making it an appropriate candidate to probe the chemical behaviour of TiO₂ surfaces.

Although a lot of research has been performed on the rutile(110) surface, only very few articles have dealt with the interaction of molecules with the rutile(011)-(2x1) surface [28, 27, 19]. The structure of the reconstructed (2x1) surface was explored only very recently [19, 20], which has an important impact on the interpretation

of the gas adsorption experiments described in the following sections.

5.1 CO interaction with $\text{TiO}_2(011)-(2 \times 1)$

While the interaction of CO with metal surfaces has been studied extensively over decades, oxides represent much more challenging systems. Apart from inherent cleanliness problems (note, for example, the difficulties in detecting and characterizing adsorbed water or hydroxyl groups [77]), one has to be very careful to avoid the accidental reduction of the surface or the subsurface region. Insulating and semiconducting oxides can yield problems due to charging effects during analysis, which may also lead to the (partial) reduction of the surface [78]. Furthermore, the low thermal conductivity has to be considered with respect to both accurate temperature measurements and uniformity of heating.

A well established route to circumvent several of these problems is to perform experiments with thin oxide films grown epitaxially on conducting bulk metal crystals. H.J. Freund and coworkers were one of the first groups using this procedure successfully in CO adsorption studies on NiO surfaces [79, 80]. By using thin rutile films on a rhenium single crystal (film thickness $\approx 5 - 35$ MLE), some of these problems can already be avoided, namely charging during electron spectroscopy, STM and LEED and the low thermal conductivity. Nevertheless, possible impurities and reduction effects of the surface, which became especially apparent during the CO TPD experiments, must still be considered. Note that during previous experiments it appeared that the annealing process to about 600 K during the TPD experiments leads to a reduced rutile surface [18], while inversely water molecules can occupy a considerable amount of CO adsorption sites up to 400 K even under UHV conditions with a base pressure of 2×10^{-10} mbar.

The following two subsections (5.1.1 and 5.1.2) describe CO TPD experiments, in which the rutile film was heated up to 430 K in every TPD run. The heating

was then switched off and the film was cooled down to 100 K within 15 minutes by means of liquid nitrogen. These conditions were found to avoid both the reduction of the oxide surface and the presence of water on the surface.

In subsection 5.1.3 several experiments are described that deal with the influence of the thermal treatment of the rutile films and the role of spurious water contaminations on the CO adsorption behaviour. From these experiments we could infer a suitable limiting temperature T_{limit} for the TPD experiments (430 K). Additionally, the results contributed significantly to the analysis of the CO TPD states.

5.1.1 TPD of CO from $\text{TiO}_2(011)-(2 \times 1)$

In this section, the completely oxidized surface of a 24 MLE thick rutile (011) film¹ was exposed to increasing CO doses at 100 K. The sample was then positioned in front of the mass spectrometer and heated with a constant rate of 4.3 K/s. The maximum temperature of the sample (T_{limit}) was chosen as 430 K in order to both remove other molecules like water, which adsorb at the surface at room temperature and to avoid a reduction of the surface above 430 K, as found in previous experiments [18]. Several blank measurements were carried out to make sure that no CO desorption took place at temperatures above 430 K.

A series of CO TPD spectra (28 amu) is displayed in figure 5.1a. It exhibits two desorption states (β_2 , β_1) at 150 K and 116 K, respectively, reflecting similar desorption energies. Desorption is complete below 180 K. The temperature of the β_2 peak maximum decreases slightly with increasing CO coverage (from 169 K at 0 L to 150 K at 0.5 L).

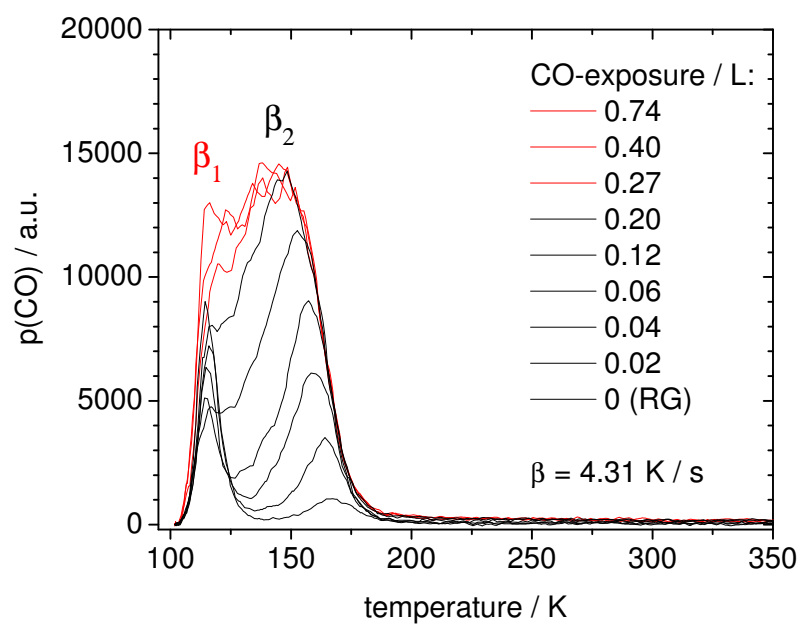
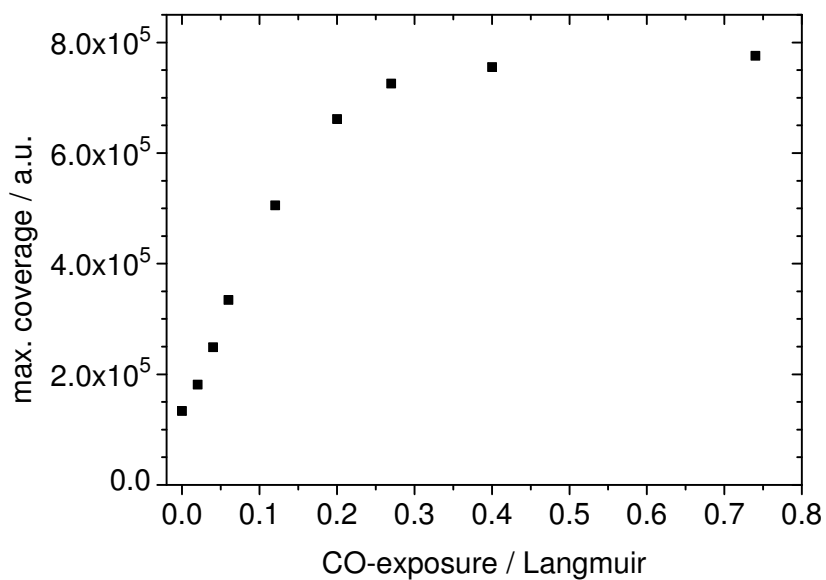
¹As discussed on page 63 in section 4.3, a film thickness of 24 MLE corresponds to a rutile film, which consists of rutile islands that have mostly grown together. However, the facet reflexes in LEED disappear completely only at a film thickness of 35 MLE. Hence, the 24 MLE film still provides facets, but is considerably smoother than a 12 MLE film.

The β_1 state already coexists in the “0 L spectrum”² and has its maximum at 116 K. The intensity of the β_1 state initially decreases with increasing CO coverage, however, it increases after exposures ≥ 0.15 L. This behaviour could be caused, e.g., by background desorption from the sample holder due to turning on the heating. In this work, however, background desorption can be safely excluded, since a β_1 state was never observed in any of the frequent adsorption studies except in the CO TPD series on the rutile film. Neither CO_2 and H_2O TPD spectra from rutile (011) nor CO spectra from $\text{Re}(10\bar{1}0)$ showed desorption right at the onset of heating. Furthermore, the intensity of the β_1 state should increase with increasing CO exposure, if it reflects background desorption.

Instead, the intensity of the β_1 state depends strongly on the chemical properties of the rutile surface, as will be discussed in more detail in section 5.1.3. By assuming a similar behaviour as the β_2 peak maximum for β_1 , namely the decrease of T_{max} with increasing CO exposure ($\Delta T_{max}(\beta_2) = -19$ K from 0 L to 0.5 L), the β_1 maximum would shift to lower temperatures and consequently (further) below the observed temperature range. At low exposures, this would result in a decrease of the peak intensity in the observed temperature range, as a smaller part of the high temperature side of β_1 is depicted in the spectra with decreasing desorption temperature.

Another peculiar feature of the β_1 state is its appearance prior to the saturation of the β_2 state. As the desorption temperature reflects the activation energy of desorption and therefore the molecule–surface binding energy, low–energy states (here β_1) should be occupied only once the high energy states (here β_2) are filled. Although the β_1 state is only partially seen in the TPD spectra (see figure 5.1a), it has a higher intensity than β_2 up to about 0.04 L. This may be explained by

²In the present thesis one spectrum was recorded prior to every TPD series, in which the crystal was only exposed to residual gas (RG) during the cooling down process. This spectrum is always referred to as “0 L” and/or “RG” (residual gas).

(a) CO TPD exposure series, $\beta = 4.31 \text{ K / s}$.

(b) Plot of the coverage versus the CO exposure.

Figure 5.1: Series of CO TPD spectra from a rutile $\text{TiO}_2(011)-(2 \times 1)$ film with increasing CO exposure, film thickness $\approx 24 \text{ MLE}$; $T_{ad} = 100 \text{ K}$.

a significantly higher amount or a better accessibility of β_1 adsorption sites.

The desorption energies of the states were calculated to be 42-37 kJ/mol (β_2) and ≤ 29 kJ/mol (β_1) via the Redhead approximation (1st order kinetics, $\nu = 10^{13} \text{ s}^{-1}$, $\beta = 4.3 \text{ K/s}$), however, due to the incomplete peak only the maximum desorption energy can be calculated for β_1 . The area of each desorption spectrum is plotted against the corresponding CO exposure in figure 5.1b. This reveals that the coverage is already constant after an initial CO exposure of about 0.3 L. Additionally, the fact that CO desorption starts immediately after turning on the heating indicates that no saturation is attained at $T_{ad} = 100 \text{ K}$.

A comparison with the well-known CO / Re(10 $\bar{1}$ 0) system enabled the amount of adsorbed CO molecules to be quantified. CO induces several coverage-dependent superstructures on the Re(10 $\bar{1}$ 0) surface [81]. For the presently used calibration, the p(1x2) superstructure was produced by exposing the Re surface to 3 L CO at 500 K³ and controlled by means of LEED. The crystal was then positioned in front of the mass spectrometer nozzle and a CO TPD spectrum was recorded (with the same surface-nozzle distance, heating rate and detector sensitivity that were used for the CO / rutile(011) / Re measurements). The p(1x2) superstructure is caused by adsorption of 0.5 ML C + O, which yields a CO coverage of 0.25 ML for molecular CO. On the Re(10 $\bar{1}$ 0) surface, a coverage of $\Theta = 1$ (ML) is defined such that every Re atom of the topmost row carries one CO molecule leading to a ratio of one CO molecule per Re unit mesh⁴. Consequently, a coverage of $\Theta = 1$ corresponds to 8.13×10^{18} CO molecules/m². The CO TPD spectra reveal 2×10^{18} a.u. (0.25 ML CO / Re(10 $\bar{1}$ 0)) and 7.7×10^5 a.u. (0.74 L CO / rutile(011)), respectively. Assuming a flat rutile film of the nominal (011) orientation, this amount corresponds to about 0.4 CO molecules per rutile(011)-

³Recipe taken from reference [81].

⁴Refer to section 2.3.2 for information on the structure of the Re(10 $\bar{1}$ 0) surface.

(2x1) unit mesh⁵. However, as pointed out above, there is some evidence that the film is not flat⁶, i.e., it has a larger surface area than a flat film. This increased surface area, on the other hand, reduces the nominal CO coverage of 0.4 CO molecules per unit mesh even further.

According to the latest model for the rutile(011)-(2x1) surface ([19, 20], see figure 2.11), one unit mesh contains two well shielded titanium atoms on the top rows and two slightly shielded Ti atoms in the troughs. It is commonly accepted that metal cations in the surface can behave as Lewis acidic sites, which accept lone pair electrons from adsorbed CO molecules [19]. Furthermore, Linsebigler *et al.* amongst others [2, 82] ascribe the CO TPD state from rutile (110) to CO desorption from the five-fold coordinated titanium centers in the (110) surface (“Ti(V)”). In their CO/rutile(110) studies, Linsebigler *et al.* determined the CO saturation coverage to $2.5 \times 10^{18} \text{ m}^{-2}$ ($T_{ad} = 105 \text{ K}$), resulting in roughly 0.5 CO molecules per (110) unit mesh [2].

Dohnálek *et al.* investigated the interaction of CO with a stoichiometric rutile(110) surface at 32 K [21] and found that the CO desorption state above 100 K (the same that was reported by Linsebigler *et al.*) only represents 0.5 ML⁷. As every second Ti(V) center is occupied and the nearest-neighbour Ti(V) sites are filled, strong repulsion between the adsorbed CO molecules results in a significant decrease of the desorption temperature from 135 K (0.5 ML CO) to 60 K (1.0 ML CO). A similar behaviour was reported by Tracy *et al.* for the CO binding energy on Pd(100). At coverages $> 0.5 \text{ ML}$, the binding energy decreased almost discontinuously (by about 0.35 eV) due to the loss of registry between the overlayer and substrate [83]. The critical distance between the CO molecules was found to be

⁵Area(rutile(011)-(2x1)) = $5.453 \times 10^{-10} \text{ m} \times 9.168 \times 10^{-10} \text{ m} = 5 \times 10^{-19} \text{ m}^2$ [51].

⁶Additional LEED spots due to facet surfaces and STM images, which show island growth (see section 4.3 for details).

⁷1 ML on rutile(110) is defined in a way that every Ti(V) center in the Ti rows carries one CO molecule.

around 3.9 Å on Pd(100), which is comparable to the distance between the Ti(V) centers on the rutile(110) surface ($d_{\text{Ti(V)}} = 2.95 \text{ \AA}$). For $\text{CO}/\text{Ti}^{4+} > 1$, Dohnálek *et al.* found a low-temperature TPD state at 52 K, which was ascribed to CO adsorption on the oxygen rows. These results yield a saturation coverage of one CO molecule per Ti(V) center for the rutile(110) surface, reflecting, however, adsorbed CO in quite different binding environments.

In contrast to rutile(110), the rutile(011)-(2x1) unit mesh contains four five-fold coordinated titanium centers. Since the titanium atoms forming the top rows of the rutile(011)-(2x1) surface are well shielded by oxygen atoms, they are considered to be rather inert [19], leaving behind merely two suitable Ti(V) centers in the unit cell. Accordingly, our estimated coverage corresponds to only 0.2 CO molecules per (suitable) titanium atom in the surface, which seems to be quite a low coverage in light of the aforementioned saturation of the monolayer, especially when compared to the results on the rutile(110) surface (1 CO/Ti(V)). Additionally, the sudden onset of the CO desorption at 100 K, which strongly suggests a pronounced β_1 state well below 100 K, supports the assumption that the monolayer is not saturated at all at temperatures $T \geq 100 \text{ K}$.

As mentioned above, the CO interaction with the rutile (110) surface was, amongst others, studied by Linsebigler *et al.* and Dohnálek *et al.* The $\text{CO}/\text{TiO}_2(110)$ TPD spectra from a fully oxidized surface exhibit a CO desorption state with a slightly coverage-dependent peak maximum at 170–135 K for coverages of 0 to 0.5 ML. The peak maximum strongly decreases from 135 to 60 K as the coverage reaches 0.5 to 1.0 ML, owing to strong repulsive interactions between the adsorbed CO molecules [21, 2].

If the present TPD spectra are compared with the data from rutile(110), it is obvious that the β_2 state observed on the epitaxial (011) rutile film (see figure 5.1) shows exactly the same behaviour and desorption temperature as the CO

desorption state from rutile(110). However, a detailed comparison has to consider also the peculiar morphology of our $\text{TiO}_2(011)$ films: As discussed in section 4.3, the epitaxial films on $\text{Re}(10\bar{1}0)$ exhibit a three-dimensional growth mode leading to a film with islands having (011)-(2x1) facets on top and on two sides and (110) facets on the other sides [16]. Based on the facts that the epitaxial rutile films exhibit (110) facets and the β_2 state features the same behaviour as the CO desorption state from the rutile (110) titanium(V) centers, the β_2 state is ascribed to the CO adsorption on the Ti(V) centers of the rutile(110) facets.

The β_1 state and its peculiar behaviour was already discussed earlier in this section, but it becomes more reasonable as the β_2 state is identified with CO desorption from the rutile(110) facets: We know that the rutile film is dominated by a (011)-(2x1)-oriented surface fraction but exhibits a minor amount of rutile(110) facets. Furthermore, the (011)-(2x1) surface covers the top and half of the sides of the individual crystallites, while the (110) facets are only at the sides, which provides both a higher amount and an easier accessibility of the (011)-(2x1) areas. Additionally, the five-fold coordinated Ti sites in the (011)-(2x1) surface are more shielded than the Ti atoms in the (110) surface. According to Gong *et al.* [19] they are considered to be quite unreactive and should, consequently, provide binding sites with a lower binding energy. Therefore, the β_1 state is believed to be due to CO adsorption at the fivefold-coordinated titanium atoms in the troughs of the rutile(011)-(2x1) surface. The decrease of the peak intensity with increasing CO coverage can be explained by a decrease in the adsorption/desorption temperature due to repulsive interactions between the adsorbed CO molecules in these sites. The β_1 intensity starts to increase immediately after the β_2 peak maximum has reached a constant position ($T_{max}(\beta_2) = 150 \text{ K}$). According to Dohnálek *et al.* [21], the CO desorption energy from rutile(110) starts to decrease strongly at this point and it may tentatively be assumed that the increase of the β_1 intensity for CO exposures above 0.1 L is actually made up

by the low-energy part of the β_2 state⁸. This behaviour is even more pronounced on rutile films with a thickness of 12 MLE, as displayed in figure 5.2.

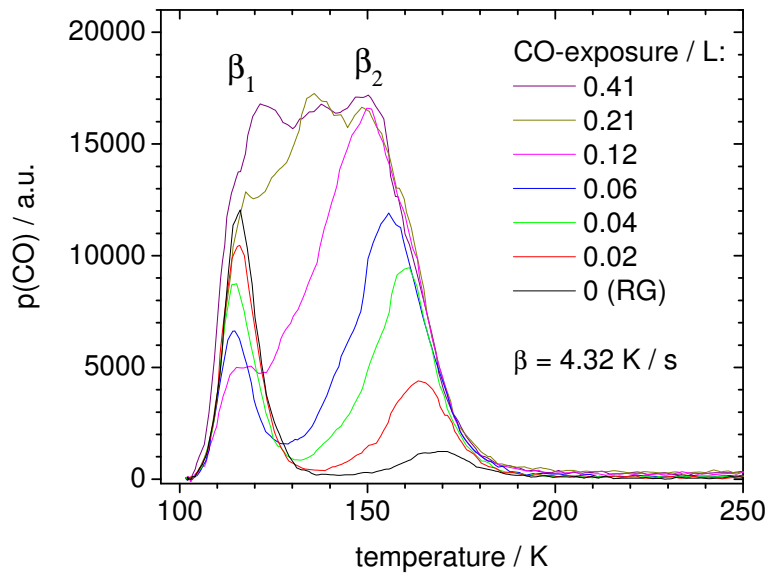


Figure 5.2: CO TPD series on a 12 MLE rutile(011)-(2x1) film with increasing CO doses. The β_1 intensity decreases with increasing CO exposure. Furthermore, it appears prior to the saturation of the β_2 state.

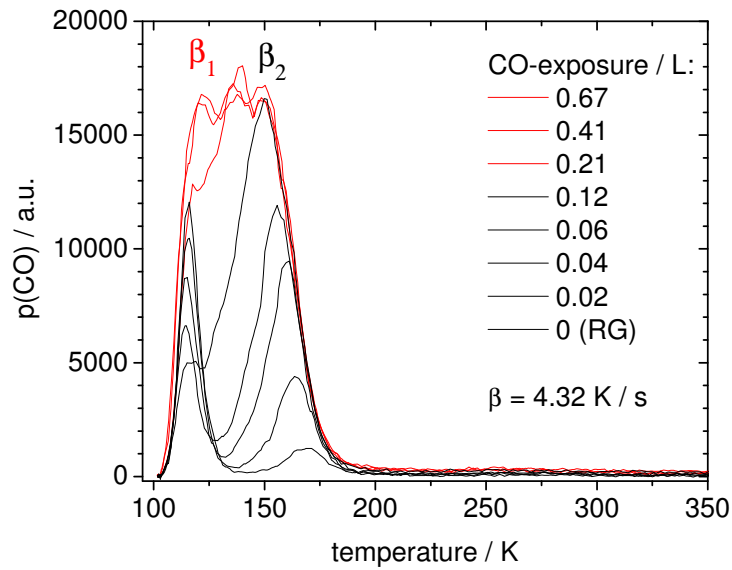
⁸The original spectra of Dohnálek *et al.* are presented in the appendix (figure .1) for comparison.

5.1.2 Influence of the surface roughness on the CO adsorption behaviour

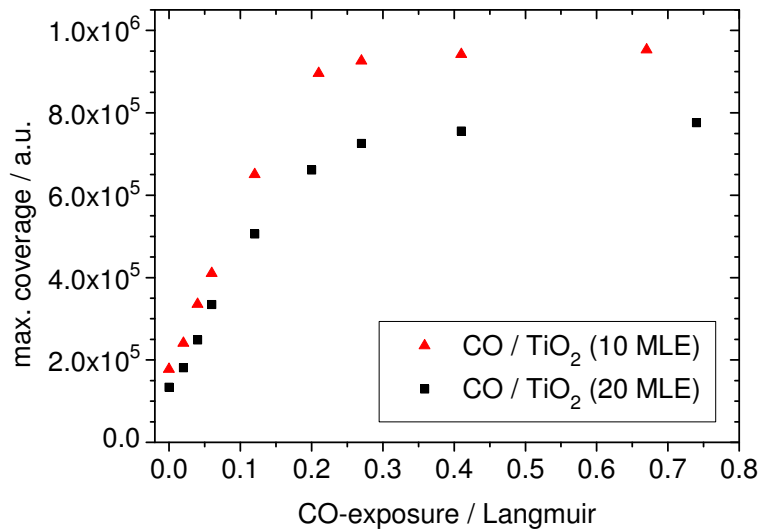
According to our observations (see section 4.3), thin films (thickness ≈ 12 MLE) exhibit a rougher surface than thicker films⁹. In order to further explore the influence of the film roughness on the CO adsorption, CO was also adsorbed on a *thin* rutile film (thickness ≈ 12 MLE) to compare the TPD spectra with the CO/rutile (24 MLE) spectra presented in the foregoing section. Films of 12 MLE thickness show intense running LEED spots and therefore exhibit the most pronounced faceting. Otherwise, the TPD experiment was carried out in exactly the same way as with the 24 MLE film. The resulting desorption spectra are depicted in figure 5.3a. They are very similar to the ones from the 24 MLE film except the obvious fact that the 12 MLE film shows a higher coverage-to-exposure ratio, as compared in figure 5.3b. The CO coverage of the thin film (12 MLE) is 25 % higher at 0.7 L exposure than that of the thick film (20MLE), which demonstrates that CO is an appropriate probe molecule to monitor surface roughness. In this peculiar case, it underlines the three-dimensional growth character of the rutile films.

The β_1 state exhibits the same behaviour both regarding the intensity decrease with increasing CO coverage and the early appearance. A coloured CO TPD series is depicted in figure 5.2 to illustrate these features.

⁹The running LEED spots indicate that faceted surfaces reach the highest intensity at a rutile film thickness of about 12 MLE. At lower thicknesses, the facets are too small to yield intense LEED spots and at higher thicknesses, the rutile islands agglomerate and the facets start to get smaller. The reflexes due to facets disappear at a film thickness of approximately 35 MLE.



(a) CO TPD exposure series on rutile(011)-(2x1)(12 MLE).



(b) Plot of the coverage over the CO exposure for two rutile films with different thickness.

Figure 5.3: a) Series of CO TPD spectra from a rutile $\text{TiO}_2(011)-(2 \times 1)$ film with increasing CO exposure, film thickness ≈ 12 MLE; $T_{ad} = 100$ K. b) Comparison of the coverages plotted over the initial CO exposure for a thin (12 MLE) and a thick (24 MLE) rutile film.

5.1.3 The influence of the thermal treatment of the TiO₂ films on the CO adsorption

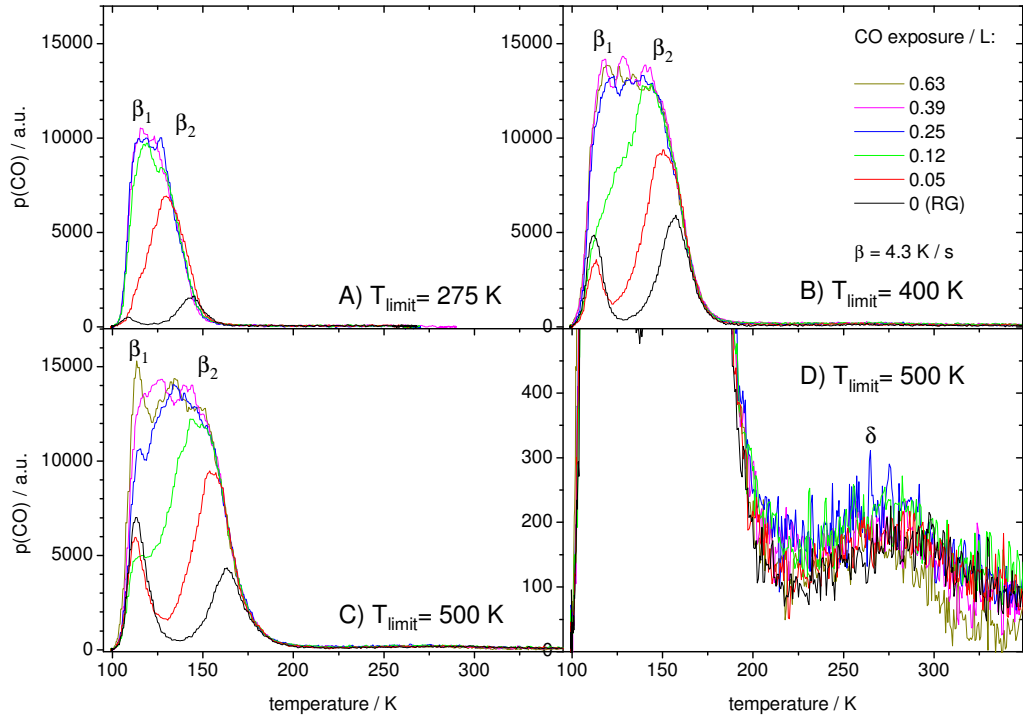
The present section summarizes several experiments that concerned the influence of thermal treatment of the rutile films and the presence of water on the surface on the CO adsorption. These experiments finally yielded the suitable maximum temperature of 430 K for the TPD spectra in the previous sections and contributed significantly to the interpretation of the CO desorption states from the epitaxial rutile films discussed in the foregoing sections.

In the first TPD experiments that were carried out within the present thesis the surface was only heated up to 275 K during the TPD experiments ($T_{ad} = 100$ K)¹⁰. This temperature was chosen both to avoid the reduction of the oxide surface¹¹ and to mimic room temperature conditions. Figure 5.4A shows the resulting CO TPD series from a 240 MLE thick rutile film. In (B) and (C), T_{limit} was chosen as 400 and 500 K, respectively. The 275 K series looks very different compared to the 400 and 500 K series. While almost complete desorption takes place below 150 K in (A), considerable desorption intensity was recorded from 150 K to 175 K in (B) and (C). In (A), β_1 and β_2 are not distinguishable at all, while they are much more separated in (B) and (C). From 400 K (B) to 500 K (C), the desorption temperatures increase only slightly. By enlarging the 500 K series (C), as done in figure 5.4D, an additional very weak desorption state at about 272 K (δ) becomes visible. Longer annealing at 400 K or 500 K did not yield further changes in the respective desorption spectra.

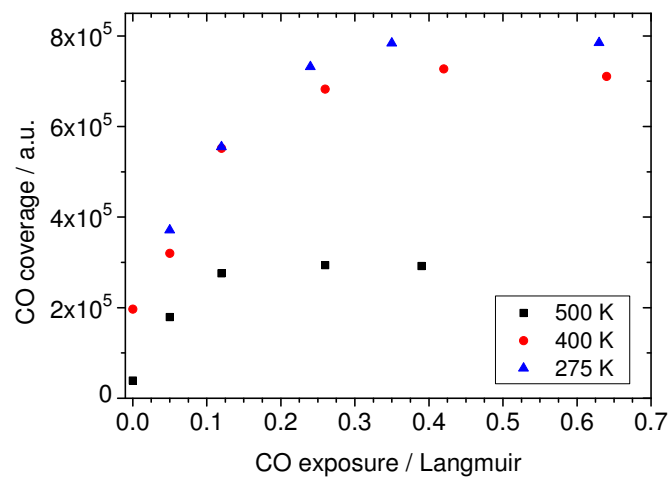
¹⁰The limiting temperature is defined as the maximum temperature that the substrate was heated up to in every TPD run and once prior to the first run. The heating was switched off immediately after reaching T_{limit} . The crystal was then cooled down by means of liquid nitrogen and exposed to CO at a substrate temperature of 100 K.

¹¹During the author's diploma thesis [18] the rutile films were found to be reduced by repeated heating to 600 K. The adsorption of CO on the oxygen vacancies yielded an additional TPD state at around 300 K, which could be titrated with oxygen.

5.1 CO interaction with $\text{TiO}_2(011)-(2 \times 1)$

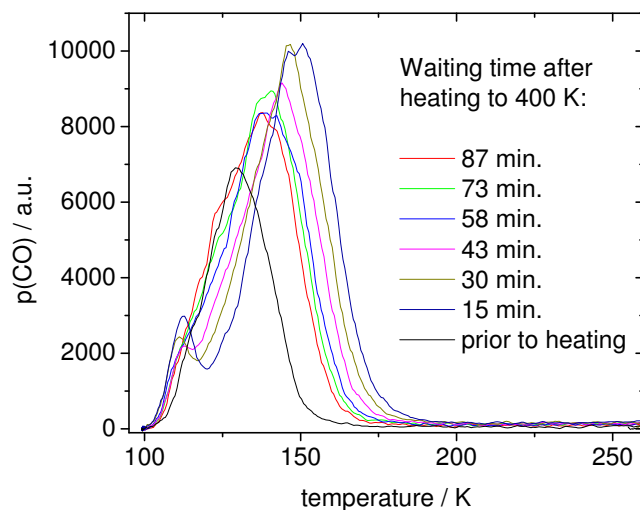


(a) Different series of CO TPD spectra that show the influence of the limiting temperature on the CO adsorption.

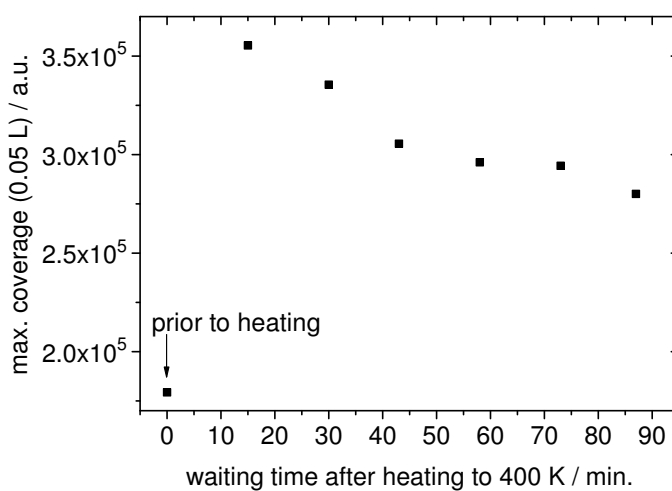


(b) Comparison of the CO coverages.

Figure 5.4: Influence of the heating temperature on the CO TPD spectra.



(a) CO TPD after heating to 400 K.



(b) Coverage of CO TPD spectra at 0.05 L.

Figure 5.5: Check for the reversibility of the changes, which occur to the TPD spectra after heating. For the depicted spectra, the sample was heated to 400 K once. The subsequent spectra were taken to a maximum temperature of 260 K. The CO exposure was always 0.5 L ($T_{ad} = 100 \text{ K}$).

5.1 CO interaction with TiO₂(011)-(2x1)

	$T_{limit} =$	275 K	400 K	500 K
β_1	T_{max} / K	115 – 108	117 – 112	114 – 113
	ΔE_{des}^* (Redhead) / kJ mol ⁻¹	30.5 – 28.6	31.0 – 29.7	30.2 – 29.9
β_2	T_{max} / K	144 – 127	157 – 142	163 – 145
	ΔE_{des}^* (Redhead) / kJ mol ⁻¹	38.4 – 33.8	42.0 – 37.9	43.7 – 38.7
δ	T_{max} / K	–	–	272
	ΔE_{des}^* (Redhead) / kJ mol ⁻¹	–	–	74.1

Table 5.1: Influence of the limiting temperature T_{limit} on the CO TPD states on epitactic rutile(011) films; film thickness ≈ 24 MLE; adsorption temperature $T_{ad} = 100$ K; heating rate $\beta = 4.3$ K/s; $\nu = 10^{13}$ s⁻¹.

By assuming first-order desorption kinetics (molecular desorption), the respective desorption energies were calculated using the Redhead formalism. The peak maxima and the Redhead desorption energies are summarized in table 5.1.

The CO yield of each spectrum is plotted against the initial CO exposure in figure 5.4b for the three different conditions (heating to 275, 400 and 500 K, respectively). The coverage (= integral) was observed to increase considerably from the 275 K to the 400 K series.

In order to further understand the change in the desorption behaviour after heating the surface to 400 K, the sample was heated to 400 K only once prior to the first TPD run. The subsequent desorption spectra were taken only up to 260 K ($T_{limit} = 260$ K). For each spectrum of this series, the surface was exposed to 0.05 L CO at 100 K. The respective desorption spectra are plotted in figure 5.5a. Figure 5.5b shows the integral of each spectrum versus the waiting time¹².

It is apparent that the desorption state(s) move(s) to lower energies with increasing waiting time; thus, the change that occurs via heating to 400 K appears to be reversible. Since the right edge of the desorption spectra in figure 5.4B,C does

¹²The *waiting time* is here defined as the elapsed time since the sample was heated to 400 K.

not change at all for subsequent spectra, it is very unlikely that the surface is altered further with every heating cycle. Every heating cycle and the following cooling process results in the same initial conditions. With this knowledge, it seems likely that another gas present in the chamber adsorbs on the surface occupying the CO adsorption sites and/or changes the chemical behaviour of the surface. As there are no changes after heating up to 300 K, this gas has to desorb between 300 and 400 K. The only gas that meets all these conditions is water vapour (see section 5.2), which is always present in the UHV chamber in small amounts.

Another experiment was carried out to obtain more information about the tem-

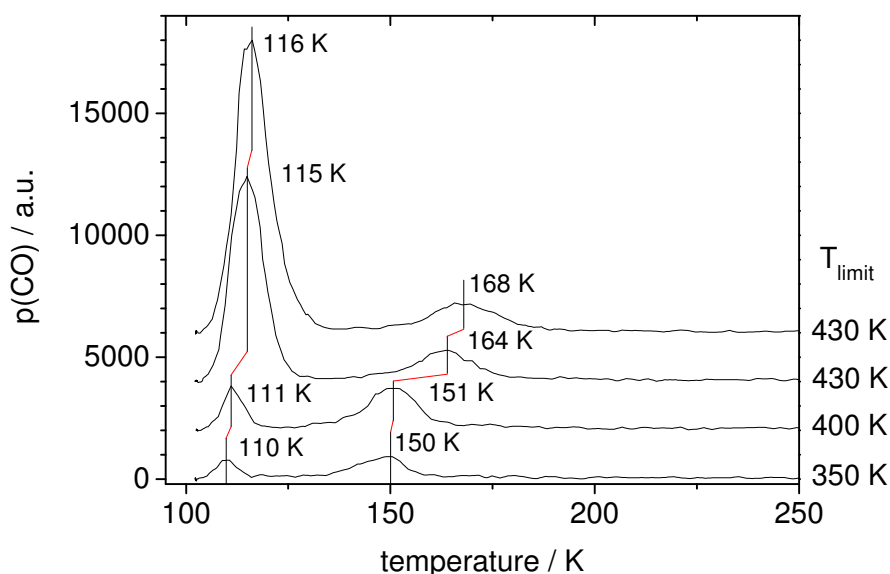


Figure 5.6: CO TPD spectra from a $\text{TiO}_2(011)-(2 \times 1)$ film; T_{limit} was increased stepwise; CO-exposure: 0 L (only from the residual gas); $\beta = 4.3$ K/s.

perature dependence of CO adsorption/desorption and the responsible H_2O adsorption/desorption state. For this experiment, only CO from the residual gas was allowed to adsorb on the surface to prevent a high CO background pres-

sure¹³. The maximal temperature (T_{limit}) was increased stepwise in every TPD run. Initially, the water adsorption sites with adsorption temperatures above 290 K were saturated with H₂O from the residual gas. The respective CO desorption spectra are shown in figure 5.6. Heating to 350 K yields a difference only in the β_1 and β_2 peak intensities. The most prominent change occurs after heating to 400 K. The intensity of the β_2 state stays almost constant, while the β_1 intensity increases significantly. Furthermore, the peak maxima change their positions from 111 to 115 K for β_1 and from 151 to 164 K for β_2 . As the β_2 intensity stays constant and the same conditions were applied as in the previous spectra, the changes have to be attributed to a modification in the chemical behaviour of the oxide surface. This would also explain the sudden increase of the β_1 intensity, in that the increase of the adsorption temperature enables a higher amount of CO molecules to adsorb at the surface at $T_{ad} = 100$ K.

5.1.4 CO adsorption on rutile(011)-(2x1) films pre-covered with H₂O

The CO adsorption on H₂O-precovered rutile films was studied to verify the preceding conclusions about the influence of co-adsorbed water on the CO TPD spectra. The rutile film was exposed to increasing doses of water vapour at 110 K prior to CO adsorption. Afterwards, 0.05 L CO were exposed to the precovered surface at 100 K. The sample was heated up to 550 K for every spectrum in order to avoid water enrichment. The respective TPD series is shown in figure 5.7 (only plotted up to 400 K), demonstrating a very similar behaviour to the spectra plotted in figure 5.5 and 5.6. Water exposures up to 0.2 L only yield a decrease of the temperature of the CO desorption maximum. Higher water coverages additionally result in a lower CO peak intensity. These results prove the effect of water pre-adsorption onto the rutile films on the CO desorption

¹³The UHV system had a base pressure of approximately 2×10^{-10} mbar.

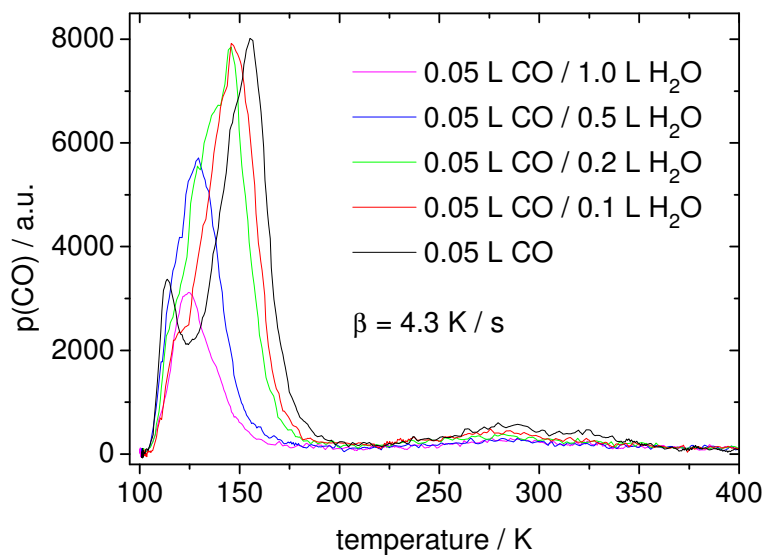


Figure 5.7: CO TPD spectra from H₂O / rutile(011)-(2x1); $\beta = 4.3 \text{ K/s}$.

behaviour.

Again, the δ state is clearly visible. It is very likely that it corresponds to CO-desorption from oxygen vacancies, which are produced by heating to 550 K in this case, either by reducing the surface or by removing the water molecules adsorbed on the oxygen vacancies.

5.1.5 CO-induced work function change ($\Delta\Phi$) on rutile(011)-(2x1)

The work function change ($\Delta\Phi$) during CO adsorption was studied by means of the self-compensating Kelvin probe method. For the measurement, the surface was exposed to a constant pressure of CO. The induced work function change was plotted against the exposure time. Figure 5.8 shows the graph for a rutile film, which was heated to 320 K prior to CO adsorption and then exposed to 1×10^{-8} mbar CO. The CO valve was opened at $t = 0$ s and closed at $t = 340$ s (marked by the dotted lines).

The work function started to decrease immediately after the CO valve was opened

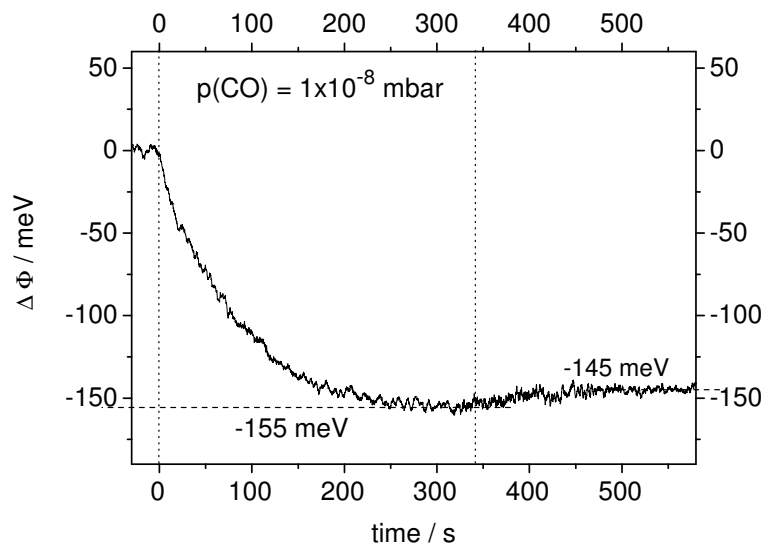


Figure 5.8: Work function change induced by adsorption of CO on rutile (011)-(2x1).

and stayed constant after about 250 s (= 2.5 Langmuir). The maximal work function change was $\Delta\Phi = -155$ meV. After closing the CO valve, the work function increased slightly by 10 meV, thus indicating a small amount of reversible CO adsorption. According to Göpel and Henzler [84], the decrease of the work

function due to CO adsorption indicates that CO acts as an electron donor. As the electron density is higher on the C atom in carbon monoxide, the decrease of the work function supports the suggestion that CO adsorbs on the rutile surface via the carbon atom end.

5.1.6 LEED observations

Adsorption of CO on rutile $\text{TiO}_2(011)-(2 \times 1)$ at 95 K did not yield any changes in the LEED pattern apart from an increase of the diffuse background leading to the conclusion that CO neither changes the inherent surface order nor forms a phase with long range order in the studied coverage interval (0.1 - 1.0 L). As the rutile(011)-(2x1) surface is not saturated with CO at all at 100 K, this finding is not surprising and does not allow conclusions regarding the CO influence/order at saturation.

5.1.7 Conclusions – CO interaction with epitactic rutile(011)-(2x1) films

The interaction of carbon monoxide with epitaxial rutile $\text{TiO}_2(011)-(2 \times 1)$ films was studied by means of TPD, $\Delta\Phi$ and LEED.

CO was exposed to rutile films with two different thicknesses (12 MLE and 24 MLE), which constitute also different degrees of surface roughness (see section 4.3), at 100 K. In both cases complete desorption takes place below 180 K. The TPD spectra show two desorption states with maxima at 116 K (β_1) and 169 - 150 K (β_2), which both represent weakly chemisorbed CO. The maximum CO yield corresponds to only 0.4 (24 MLE) and 0.5 (12 MLE) CO molecules per rutile $\text{TiO}_2(011)-(2 \times 1)$ unit mesh, respectively, if a flat film is assumed. These low maximum CO coverages already indicate that no saturation of the monolayer

is reached at 100 K¹⁴.

THE ORIGIN OF THE β_2 STATE – The CO adsorption on the thermodynamically most stable (110) surface was already extensively investigated previously [22, 21, 14]. The TPD spectra of CO adsorbed on a ‘nearly perfect’ rutile (110) single crystal show one single desorption state with a maximum at 170 to 135 K after CO adsorption at 105 K. This state is ascribed to vertically adsorbed CO molecules at the fivefold-coordinated titanium atoms of the rutile(110) surface [22, 82]. On ‘pre-annealed’ films, a second desorption state appears around 300 K, which can be titrated with oxygen and is explained by CO adsorption on oxygen vacancies¹⁵. CO adsorption at 32 K revealed that only half of the Ti(V) centers can be saturated at 100 K, as the desorption energy decreases by 65 K from $\Theta = 0.5$ to 1.0 due to strong repulsive interactions between the adsorbed CO molecules [21].

The desorption temperature of the main CO TPD state on rutile(110) fits very well with the β_2 state. The peak shows the same behaviour regarding increasing CO exposures. Since the rutile films also exhibit (110) oriented facets, it is very likely that the β_2 state is due to CO desorption from the Ti(V) centers of the rutile(110) facets.

THE δ STATE – Furthermore, the desorption temperature of the δ state coincides well with the CO desorption from oxygen vacancies on rutile (110). The δ state is only visible after annealing of the surface to around 500 K, which suggests that the respective adsorption sites are either produced by surface reduction due to the heating or, alternatively, by removal of co-adsorbed molecules (other than CO) at around 500 K. Therefore, the δ state is ascribed to CO desorption from

¹⁴In this case, saturation is defined in a way that every suitable Ti(V) center in the surface is bound to one CO molecule. As discussed before (see section 5.1.1), the rutile(011)-(2x1) unit mesh contains two suitable Ti(V) centers.

¹⁵The oxygen vacancies on rutile(110) are produced by removing bridging oxygen atoms.

oxygen vacancies in the rutile(110) facets of the films.

THE ORIGIN OF THE β_1 STATE – Even if only CO from the residual gas is allowed to adsorb (“0 L”), the β_1 state already coexists with the β_2 state, although the two states have a temperature difference of 53 K at 0 L. Furthermore, the β_1 state has a higher intensity after exposing small amounts of CO, while its intensity decreases at higher exposures. These phenomena can be explained by the morphology of the rutile films. As already discussed in detail, the films provide 3-dimensional islands with (011)-surfaces on top and additional (011) and (110) facets at the sides. The coexistence of the β_1 state at low coverages indicates that the amount of β_1 adsorption sites is significantly higher than the amount of β_2 sites and/or that the β_1 sites are more easily accessible. The initially decreasing intensity with increasing CO exposure can be explained by a decrease of the desorption temperature at higher CO coverages. The results of the temperature dependent studies (see figure 5.6) support these suggestions. In this case, the desorption of water resulted in a desorption temperature increase of 4 K for the CO β_1 maximum, which led to a significant increase in the β_1 intensity. By taking into account all the obtained information, the β_1 state is ascribed to CO desorption from the rutile(011)-(2x1) surface and facets. The desorption maximum appears to be below 100 K for higher coverages.

CO ADSORPTION SITES ON RUTILE(011) – According to recent studies [20, 19], the rutile(011)-(2x1) surface provides two inequivalent types of both two-coordinate oxygen atoms and five-coordinate titanium atoms. In the rutile(011)-(2x1) surface, the Ti(V) atoms at the top are shielded by two bridging oxygen atoms, while the Ti(V) centers at the sides of the valleys are less shielded. The surface was considered to be rather inert with respect to the adsorption of small probe molecules by Gong *et al.* [19]. Although this was only calculated for defect-free flat surfaces, the tendency seems to be right for CO adsorption. We ascribe the β_1 state to molecular adsorption of CO on the Ti(V) centers in the valleys of

5.1 CO interaction with TiO₂(011)-(2x1)

	β_1	β_2	δ
T_{max} / K	≤ 116	169 – 150	275
ΔE_{des}^* (Redhead) / kJ mol ⁻¹	≤ 29	42 – 37	70
T_{limit} / K	430	430	500
CO adsorption site	Ti(V) in the valleys of rutile(011)-(2x1)	Ti(V) centers, rutile(110)	oxygen vacancies, rutile(110)
desorption kinetics	1 st order, molecular	1 st order, molecular	1 st order, molecular
references	[19]	[21, 22, 14]	[22, 14, 85]

Table 5.2: Summary of the CO interaction with epitaxial rutile (011)-(2x1) films grown on a Re(10 $\bar{1}$ 0) single crystal surface. $\nu = 10^{13} \text{ s}^{-1}$.

the rutile(011)-(2x1) surface via the carbon atom. This assumption is supported by the work function decrease due to CO adsorption, which shows that CO acts as an electron donor [84].

The results regarding the CO interaction with epitaxial rutile(011)-(2x1) films grown on a Re(10 $\bar{1}$ 0) single crystal surface are summarized in table 5.2.

INFLUENCE OF WATER – The results on the influence of the preparation conditions, the temperature dependence and the H₂O co-adsorption already give some insight into the interaction of water with the rutile(011)-(2x1) films. The water desorption states up to 350 K seem to mainly occupy or block the CO adsorption sites of the β_1 and β_2 state, while the water desorption states around 400 K change the chemical behaviour of the oxide surface, which results in a significant shift of the CO desorption temperatures. Heating to 500 K either reduces the surface or removes water from the oxygen vacancies of the rutile(110) facets. The interaction of water with the rutile films will be discussed in detail in the following chapter.

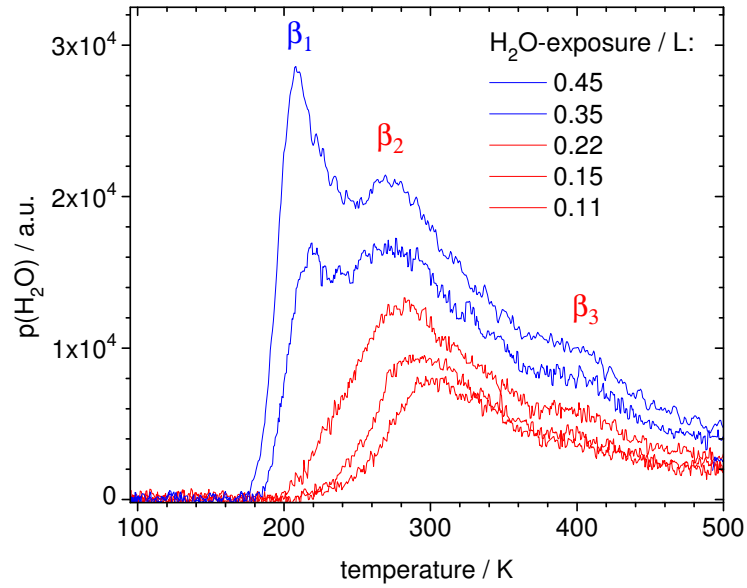
5.2 Water interaction with TiO₂(011)-(2x1)

Main points of interest in the interaction of water with rutile surfaces concern both the photocatalytic properties of titanium dioxide and its activity in the low-temperature CO oxidation reaction. In this latter reaction, water may play a decisive role, either as a reactant, inhibitor or as a catalyst itself, at least under practical catalytic conditions. These real conditions mainly consist of atmospheric pressure and the presence of ambient air, which does not exclusively contain the reactants but also water vapour. Due to the always ubiquitous water vapour it is indispensable to study how water vapour in the air around a catalyst will interact with the surface. Furthermore, as pointed out in section 5.1, water influences the CO adsorption behaviour on rutile surfaces significantly.

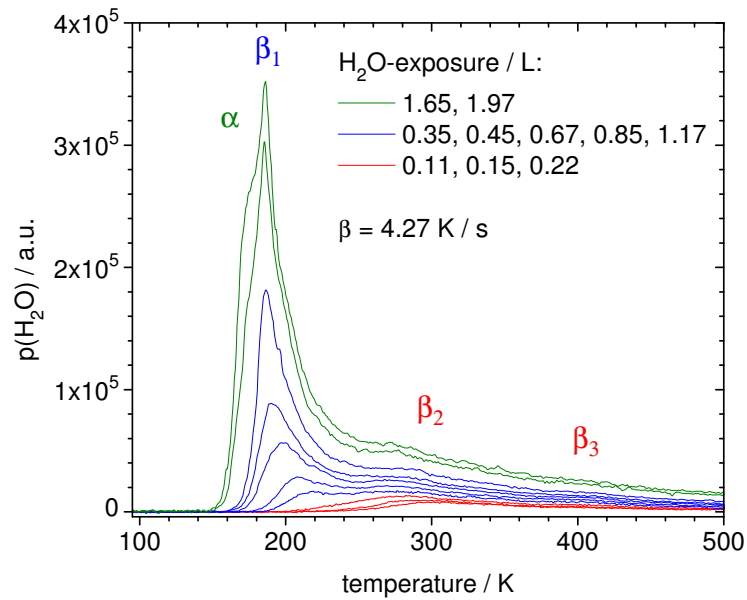
As a substrate, rutile TiO₂(011)-(2x1) films with a thickness of ca. 24 MLE were used in most of the measurements. The water was dosed via a bakeable leak valve by filling the ambient from a liquid water reservoir, which was heated in order to enhance vapourization. The water in the reservoir was purified by several freeze-pump-thaw cycles. The water exposures given in the text were determined by integration of the dosing pressure versus exposure time plot of the respective TPD spectrum.

5.2.1 TPD of H₂O from TiO₂(011)-(2x1): The origin of the various desorption states.

In the TPD experiments, the rutile film was cooled to 95 K and then exposed to increasing doses of H₂O. Thermal desorption was performed by heating the film at a constant rate of 4.3 K/s up to 550 K. Thereafter the sample was allowed to cool by means of liquid nitrogen, which took 15 minutes to reach 95 K again. A series of corresponding desorption spectra (18 amu) is shown in figure 5.9. The spectra exhibit at least four different desorption states with desorption maxima



(a) 0.11 - 0.45 L



(b) 0.11 - 1.97 L

Figure 5.9: Series of H_2O TPD spectra from a 24 MLE thick rutile film with increasing H_2O exposure; heating rate $\beta = 4.3 \text{ K/s}$; $T_{ad} = 95 \text{ K}$.

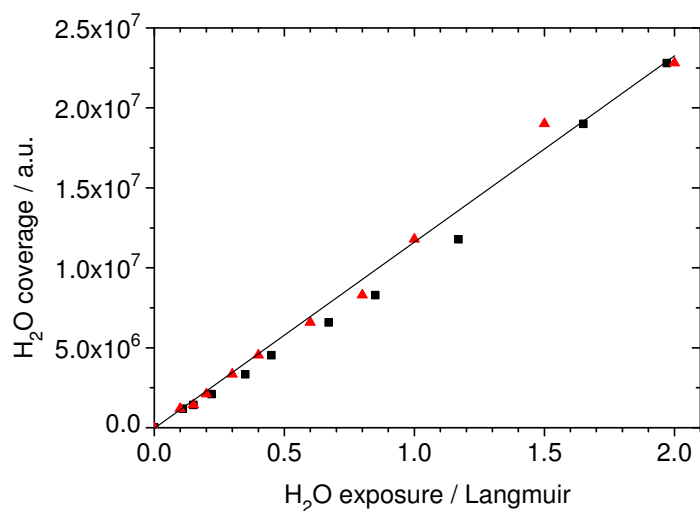


Figure 5.10: Plot of the TPD H₂O yield against the initial H₂O exposure; $\beta = 4.3$ K/s; $T_{ad} = 95$ K; triangles: exposure determined from the pressure meter reading, squares: exposure determined from the pressure versus time plot during exposure.

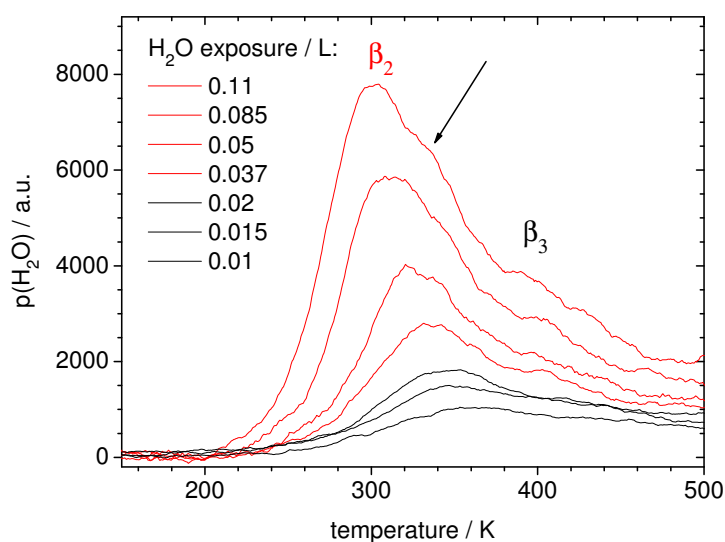


Figure 5.11: Series of H₂O TPD spectra from a 24 MLE thick rutile(011)-(2x1) film with CO exposures of 0.01 to 0.11 L; the arrow marks the weak desorption shoulder at around 340 K; the spectra have been smoothed via adjacent averaging; $\beta = 4.3$ K/s; $T_{ad} = 95$ K.

at 405 K (β_3), 300-271 K (β_2), 220-186 K (β_1) and < 186 K (α). In figure 5.10, the H_2O yield of each spectrum is plotted against the corresponding H_2O exposure. The linear relation of the exposure indicates a constant sticking probability from 0.1 to 2.0 L exposure. The α state, which we ascribe to multilayer desorption, starts to appear after a water exposure of about 1.65 L. The three β states presumably reflect H_2O desorption from the energetically heterogeneous monolayer. The estimated Redhead desorption energies are listed in table 5.4 on page 111. A more detailed inspection of the region between the β_2 and the β_3 state as well as between β_1 and β_2 reveals two weak shoulders at about 220 and 340 K. The shoulder at 340 K is better visible in TPD spectra with very low exposures (0.01 – 0.11 L), as shown in figure 5.11. Previous studies in another recipient that were performed with a 35 ML thick film revealed more pronounced desorption states at 340 and 400 K. The respective desorption spectra are depicted in figure 5.12.

A comparison with our spectra on epitaxial rutile(011)-(2x1) films with H_2O desorption spectra from rutile(110) and (100) bulk single crystals [25] reveals immediately that the observed desorption states are much broader and overlap more strongly with the TiO_2 thin films. It is very likely that this is due to the rough morphology of the rutile films, which yields plenty of energetically slightly different adsorption sites, whereas the experiments on rutile(110) and (100) have been carried out on the comparatively flat surfaces of rutile single crystals [25]. This assumption is supported by Zehr *et al.* [24], who studied the influence of oxygen-induced surface roughening on the water adsorption on rutile(110). These authors demonstrated that high exposures of oxygen prior to the water adsorption induce a significant broadening and, to some extent, also a splitting of the water desorption states. The same effect, namely the generation of energetically more ill-defined states, resulted from sputtering and preheating of the rutile crystals.

According to Zehr *et al.*, water adsorption on vacuum annealed rutile(110) at

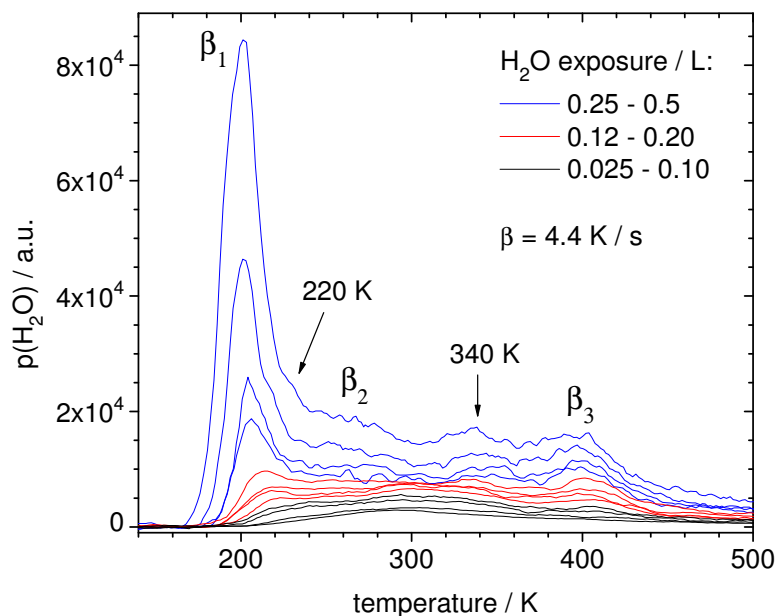


Figure 5.12: Series of H₂O TPD spectra on a 36 MLE thick rutile film that was prepared and studied in another recipient (the TPD intensities differ systematically from the other spectra). The spectra were smoothed via adjacent averaging prior to plotting. The temperature measurement is not as reliable as in the other spectra. $\beta = 4.4$ K/s; $T_{ad} = 127$ K.

110 K yields four different desorption states at around 500, 262, 171 and 149 K, which are assigned to dissociative H₂O adsorption on oxygen vacancies (500 K state, occurs only on reduced surfaces), molecular water bound to the Ti(V) centers on the (110) surface via the oxygen atom (262 K state) and molecular water bound to the bridging oxygen atoms of the surface via the hydrogen atoms (171 K state) [24]. The 149 K state is induced by condensed water that forms ice layers on the monolayer.

The H₂O TPD spectra on rutile(100) [25] exhibit some differences with respect to the (110) spectra, which are manifested mainly in the number of monolayer TPD states and the amount of desorbing water above 300 K. The H₂O spectra reflecting the monolayer coverage obtained from the rutile(100) surface exhibit

two desorption states below 300 K (at 165 K and 245 K) and one broad state between 300 and 350 K ($T_{ad} = 140$ K) [25]. The broad desorption state between 300 and 350 K is ascribed to dissociative adsorption at the fivefold-coordinated titanium centers of the (100) surface. According to Henderson *et al.* [25], a desorption temperature of 290 K could possibly be chosen as a benchmark for TPD spectra to distinguish between molecular and dissociative water adsorption on TiO_2 single-crystal surfaces.

A comparison of the spectra from rutile(110) and (100) in reference [25] with our thermal desorption (TD) data reveals various similarities. The β_1 state, which was ascribed to molecular adsorption of water via hydrogen-bonds to the bridging oxygen atoms of the (110) and (100) surface, is more pronounced on our rutile(011)-(2x1) films (if one compares the β_1/β_2 ratio on the three surfaces). Apart from that, the β_1 state appears at 186 K, which is close to the respective state on rutile(110) at 171 K [24] and on rutile(100) at 165 K [25]¹⁶. The good agreement with respect to the desorption temperature between the states on the different rutile surfaces suggests that the β_1 state on rutile(011)-(2x1) also reflects the desorption of molecular water, which is bound to the oxygen atoms of the (011)-(2x1) surface via H-bonds (the specific binding sites will be discussed in more detail later in this section). Due to the film morphology (discussed in section 4.3), it is likely that the β_1 state also contains contributions from water adsorbed on the (110) and the (100) oriented surface patches of our films.

The β_2 state at 271 K state has a relatively low intensity compared to the respective TPD states on rutile(110) and (100) [25]. However, the already mentioned study of Zehr *et al.* revealed that the water TPD states on rutile(110) become significantly less resolved when the surface is cooled down in oxygen¹⁷ instead of

¹⁶Please note that a quantitative comparison between the desorption temperatures is not possible due to the heating rate dependence of the peak maxima.

¹⁷ $p(\text{O}_2) = 7.5 \times 10^{-7}$ Torr $\cong 1 \times 10^{-6}$ mbar.

vacuum after annealing to 850 K [24]. The spectra obtained after annealing do not longer allow a distinction between the ice layer and β_1 , the valley between β_1 and β_2 has almost evened out and the β_2 state is significantly broadened by a pronounced high-temperature tail ($\theta = 2.9$ ML H_2O) [24]. According to Henderson, these changes are due to oxygen-induced surface roughening [25]. The rutile films, which are studied in this thesis, were grown in an oxygen atmosphere of $p(\text{O}_2) = 1 \times 10^{-6}$ mbar at 900 K and then cooled to about 500 K in oxygen. The STM images presented in section 4.3 reveal that the rutile(011)-(2x1) films exhibit a very rough morphology. Therefore it is not surprising that they interact with water vapour in a similar way as rough rutile(110) surfaces.

Nevertheless, the intensity of the β_2 state on rutile(011)-(2x1) films is still lower than on bulk rutile(110) surfaces. From the CO TPD spectra we already know that the rutile(110) facets of the rutile films have an influence on the CO spectra (see subsection 5.1.1) in that they show a significant amount of specific CO desorption contributions from rutile(110). Accordingly, the H_2O spectra should also exhibit TPD states stemming from rutile(110) patches. It is therefore likely that the β_2 state reflects water desorbing from Ti(V) centers of the (110) facets.

The most significant difference between the rutile(011)-(2x1) spectra and the literature reference spectra from rutile (110) and (100) is the weak, but clearly visible, β_3 state around 405 K. The co-adsorption behaviour of H_2O and CO was already discussed in section 5.1.4. The removal of water adsorbed between 300 and 350 K prior to a CO TPD experiment only yielded a small increase in the CO TPD intensity, whereas heating to 400 and 430 K led to a significant blueshift of the CO peak maxima. This shift may suggest that the H_2O adsorption states between 350 and 430 K induce a significant change in the electronic structure of the rutile surface. It is therefore not unlikely that the water species forming the β_3 state consist of dissociated $\text{H} + \text{OH}$. An inspection of “high-temperature” water states observed with the (110) surface at 500 K and the (100) surface between

300 and 350 K reveals that these states are both due to recombination of surface hydroxyls [86, 25, 26, 77, 87].

The interaction of water with a rutile(011)-(2x1) single crystal surface was already studied by means of STM and UPS by U. Diebold and her coworkers [28, 27]. Although their interpretations were based on the titanyl-model of the surface, which is now superseded, the experimental data can still be used as complementary information. Their UPS studies of water adsorbed on rutile(011)-(2x1) at 110 K yielded a small 3σ state at 11.4 eV that was ascribed to dissociatively adsorbed water. This state had a higher intensity at 0.3 L than the state ascribed to molecularly adsorbed water; from 0.6 L on, the molecular states became too strong for a proper identification [27]. The molecular UPS features disappeared around 200 K and the dissociated water features remained on the surface up to around 300 K [28, 27]. Adsorption at 300 K yielded STM images with additional bright spots on top of the zig-zag oxygen rows, which covered a maximum of 0.25 ML. These spots were assigned to hydroxyl groups.

The studies by Diebold *et al.* [28, 27] may support our assignment of the various H_2O TPD states. In previous work, long tails of water desorption up to 500 K have been observed on the rough rutile(110) surface [23, 24]. Therefore, our β_3 state could also be caused by the step and kink sites of the rough films as well. However, this cannot be compared in a satisfactory way as no low exposure spectra exist in the literature (to the author's knowledge), but the dissociative features obtained by Diebold and coworkers on a comparatively flat rutile(011)-(2x1) single crystal surface point out that the surface itself is responsible for some amount of dissociative adsorption [28, 27]. Furthermore, TPD spectra from a 36 MLE thick film (see figure 5.12) possess a more intense β_3 state although 36 MLE thick films possess a smoother morphology¹⁸.

¹⁸Rutile films with a thickness of ≥ 36 MLE did not show running LEED spots any more, which are indicative of facets.

The studies on a 36 MLE thick film show a resolved desorption state at ≈ 340 K (see figure 5.12). On a 24 MLE thick film this 340 K state is only visible as a small shoulder in the TPD spectra (see figure 5.11). Water TPD spectra on rutile(100) [25] also show such a desorption state between 300 and 350 K, which is caused by recombination of hydroxyl groups with hydrogen. According to x-ray diffraction (XRD) data on our rutile films, about 2% of the rutile film grows with a (100) orientation (film thickness $\approx 500 \text{ \AA} \cong 200$ MLE) [16]. A rough calculation of the ratio between the area of the 340 K state and the total desorption intensity of the 0.5 L spectrum in figure 5.12 reveals a proportion of about 1.5% for the 340 K state. This value fits very well with the (100) surface contribution of 2% that was obtained from XRD. Therefore, the 340 K state/shoulder is assigned to dissociatively adsorbed water on the Ti(V) centers of the (100) surface¹⁹.

The other weak shoulder at 220 K was also visible as a desorption state on water TPD spectra obtained from rutile(100) [88] and is therefore ascribed to molecular adsorption of water on the Ti(V) centers of rutile(100).

The water TPD states and their proposed origins are summarized in table 5.4 on page 111.

5.2.2 LEED – H₂O / TiO₂(011)-(2x1)

The adsorption of water on rutile at 300 K did not yield any changes in the LEED pattern of the rutile film. Water adsorption at 100 K only resulted in an increase of the diffuse background, no ordered phase could be observed. However, after exposing a 24 MLE thick rutile film to 1×10^{-8} mbar water at 174 K for about 60 s (exposure ≈ 0.6 L), a (1x2) LEED superstructure appeared (see figure 5.14b). The missing spots in $(h = n \pm \frac{1}{2}, k = 0)$ positions (related to the Re pattern) characteristic for the clean TiO₂(011)-(2x1) surface remained invisible

¹⁹The structure of the rutile(100) surface is depicted in figure 2.9 on page 20.

5.2 Water interaction with $\text{TiO}_2(011)-(2 \times 1)$

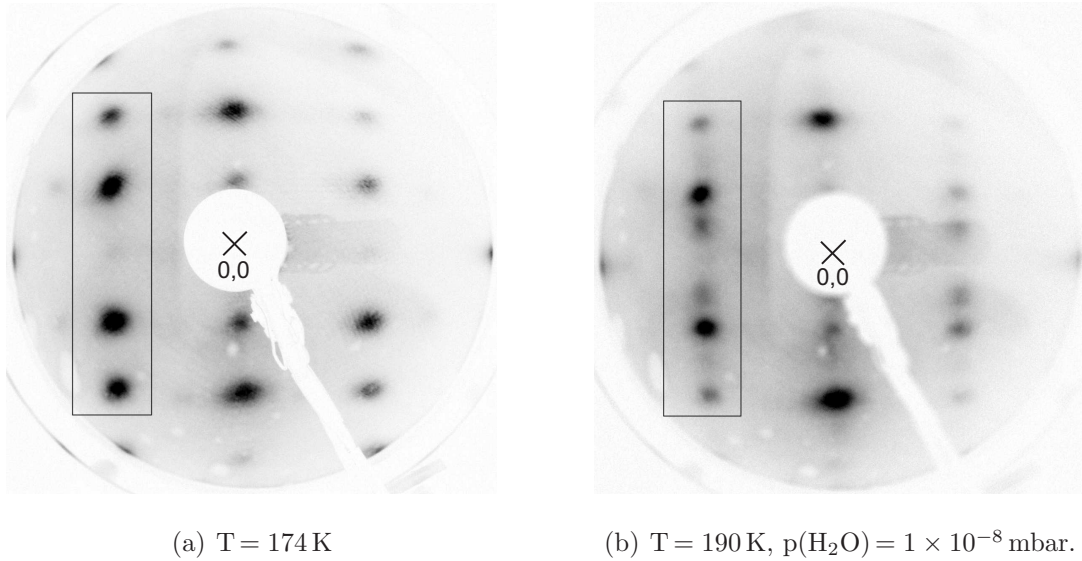


Figure 5.13: LEED patterns of a 24 MLE thick rutile(011)-(2x1) film; electron beam energy = 35 eV; a) pure rutile film at 174 K; b) (1x2) superstructure on rutile, $p(\text{H}_2\text{O}) = 1 \times 10^{-8}$ mbar, $T = 190 \text{ K}$; the rectangular boxes mark the region of the patterns that was taken for figure 5.14 ($h = -1, k = (-2) - (+2)$).

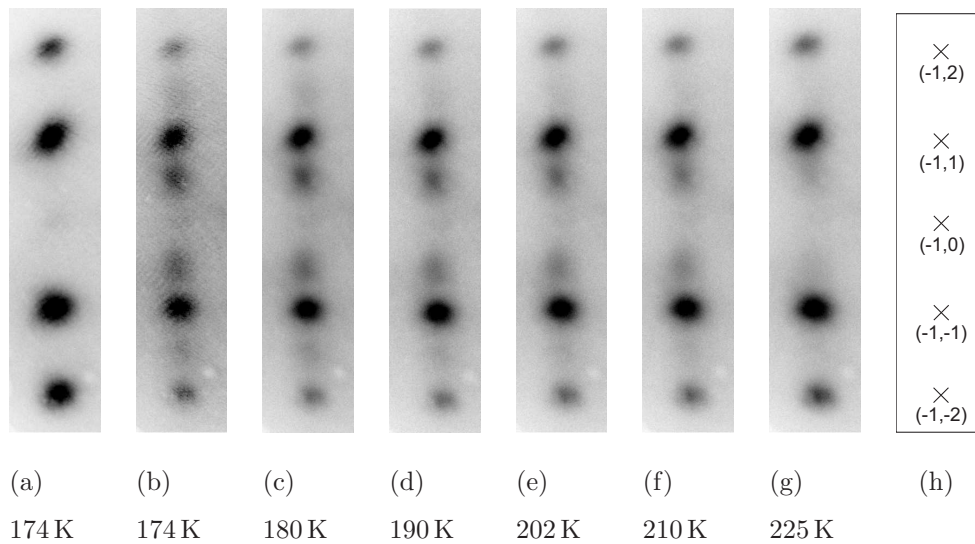


Figure 5.14: $(1 \times 2)\text{H}_2\text{O}$ superstructure on rutile $\text{TiO}_2(011)-(2 \times 1)$ at different temperatures; a) only residual gas, b) – f) $p(\text{H}_2\text{O}) = 1 \times 10^{-8}$ mbar, g) $p(\text{H}_2\text{O}) = 3 \times 10^{-9}$ mbar; h) spot designation; electron beam energy = 35 eV.

for normal electron beam incidence. Apparently, the adsorbed H₂O molecules do not alter the glide mirror symmetry of the (011) rutile lattice. The superstructure did not disappear after closing the water supply. Figure 5.13 shows the LEED pattern of the rutile film at $T = 174$ K (a) and the H₂O-induced (1x2) superstructure at $T = 190$ K (b), both taken at 35 eV electron energy. The rectangular boxes mark the region of the pattern that was taken for a comparison of the structure at different temperatures. This temperature dependence is shown in figure 5.14. In the respective experiment, the water pressure of 1×10^{-8} mbar was kept constant while the LEED patterns were monitored, the reason being partial electron beam induced H₂O desorption. From time to time the H₂O flux was turned off to make sure that the H₂O-induced superstructure persisted also without a constant water supply. The (1x2) superstructure spots reached their highest intensity between 180 and 190 K (see figures 5.13 and 5.14c). However, the respective intensity decreased significantly from 200 to 210 K and went to almost zero at 225 K. This temperature dependence strongly suggests that the ordered H₂O phase is associated with the β_1 H₂O TPD state.

We remark here that the respective H₂O phase showed the best long-range order around $T = 200$ K when the TiO₂ sample was allowed to slowly warm up from 100 K to room temperature in an ambient that contained a fairly large H₂O partial pressure. This may be taken as a hint that some thermal activation is necessary for forming the superstructure. Another clear information obtained from our experiment is that the (1x2) superstructure only forms at temperatures $T \geq 170$ K. At this temperature, the α -TPD state is no longer present on the surface, which means that condensing H₂O molecules cannot perturb the development of the long-range order of the first H₂O monolayer.

With respect to the interpretation of the LEED pattern, a (1x2) superstructure means that water binds onto the surface with a (1x2) periodicity related to the rutile(011)-(2x1) substrate and does not lift its inherent (1x2) reconstruc-

tion. This implies that the lattice vector of the overlayer is twice as large as the substrate vector in $[100]$ direction (perpendicular to the troughs), but has the same length as the substrate vector in the perpendicular direction (parallel to the rows) (see figures 2.10 and 2.11). This means, on the other hand, that the water structure is repeated every second rutile row. According to unpublished information by A. Selloni and U. Diebold, STM images of the “ β_1 state” show features in the trenches of rutile(011)-(2x1) without a visible (1x2) periodicity. This could either suggest that water adsorbs with a different geometry in every second trench or that the observed (1x2) superstructure is caused by only half of the population of the β_1 state. The latter explanation would also account for the narrow temperature range in which the superstructure is visible. Considering all available information concerning the β_1 state, we suppose that it is caused by adsorption of molecular water that couples to the oxygen atoms of the troughs of the (011)-(2x1) surface via the hydrogen atoms. Furthermore, it is very likely that half of the β_1 state population induces a (1x2) superstructure on the film by filling every second trough.

5.2.3 Water-induced work function change on rutile(011)-(2x1)

The water-induced work function change was studied by means of the self-compensating Kelvin probe method. A 24 MLE thick rutile film was exposed to 2×10^{-8} mbar water vapour at 100 K. The resulting work function change was recorded and plotted against the deposition time in figure 5.15. The water supply was opened at 0 s and closed at 750 s (marked by the vertical dotted lines in figure 5.15). The overall work function change added up to $\Delta\Phi = -1020$ meV after 1100 s.

Additionally, the pressure was recorded during the experiment and the exposure was calculated from the integral of the pressure versus time plot. The details

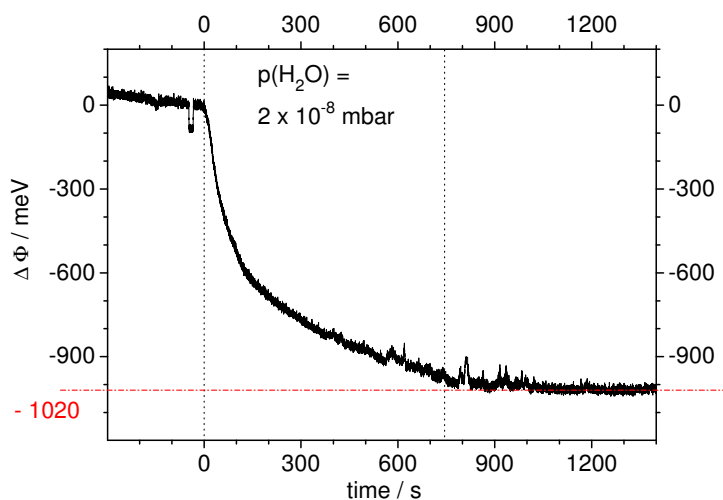
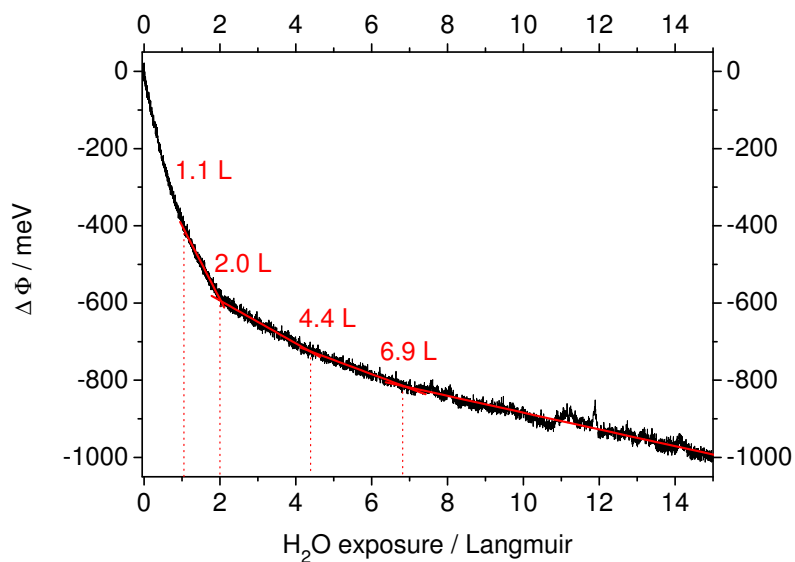


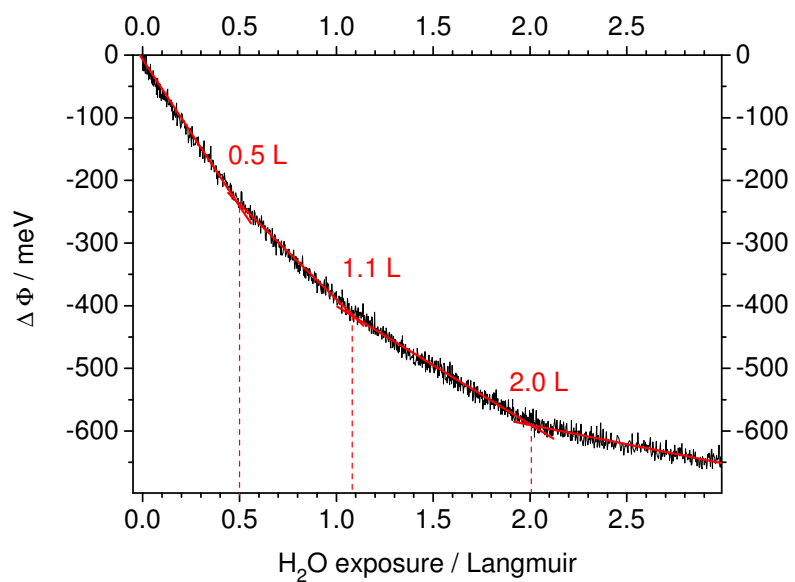
Figure 5.15: Work function change induced by H₂O adsorption on rutile(011)-(2x1) (overview).

of the work function change versus water exposure relation are shown in figures 5.16a (0 – 15 L) and b (0 – 3 L). A pronounced change of the slope is immediately apparent at 2.0 L H₂O exposure. Furthermore, careful inspection of the $\Delta\Phi$ exposure relation reveals slight discontinuities of the slope at 0.5, 1.1, 4.4 and 6.9 L. The slope was linearly fitted within these regions and listed in table 5.3 together with the absolute $\Delta\Phi$ for the respective region. On the basis of the associated exposures, the different regions were tentatively attributed to the water TPD states discussed in subsection 5.2.1. At any rate, however, the most pronounced change in the work function – exposure relation occurs at 2.0 L, where the slope decreases by 70%. As the exposure of 2.0 L coincides well with the formation of the α state, we associate the break at 2 L H₂O exposure with the completion of the monolayer. The subsequent filling of the α state (beginning multilayer region) does no longer give rise to such a strong surface potential change.

The first discontinuity at 0.5 L can probably be attributed to the saturation of the β_3 and β_2 state. Between 0.5 and 1.1 L mainly the β_1 state should be responsible



(a) 0 – 15 L



(b) 0 – 3 L

Figure 5.16: Work function change induced by H_2O adsorption on rutile $(011)-(2 \times 1)$ plotted against the H_2O exposure, film thickness ≈ 24 MLE, $T_{ad} = 100$ K.

for the work function change. At exposures > 1.0 L, the α state starts to form and the work function change between 1.1 and 2.0 L is probably composed of the β_1 state and parts of α . The further changes at 4.4 and 6.9 L could be due to the completion of the first and the second multilayer.

These assignments are consistent with data from De Valentin *et al.*, who measured the water-induced work function change on rutile(011)-(2x1) via UPS and obtained a change of about -1.2 eV from 0 to 1.0 L with a relatively sharp break at 0.4 L [27]. This break was ascribed to the change from dissociative to molecular adsorption.

The information on the water-induced work function change is summarized in table 5.3. The fact that the results from the $\Delta\Phi$ experiment, which is a non-destructive method, are consistent with the TPD desorption states indicates that the TPD experiments are reversible and do not destroy or alter the surface and/or the adsorbed water molecules.

exposure region / Langmuir	$\Delta\Phi$ slope / meV Langmuir ⁻¹	absolute $\Delta\Phi$ / meV	corresponding TPD state(s)
0 – 0.5	-468 ± 4	-240	β_2, β_3
0.5 – 1.1	-303 ± 4	-360	β_1
1.1 – 2.0	-189 ± 2	-174	$\beta_1 (+\alpha)$
2.0 – 4.4	-55 ± 1	-129	$\alpha - 1^{st}$ multilayer
4.4 – 6.9	-37 ± 1	-92	2^{nd} multilayer
6.9 – 16	-21 ± 1	-196	

Table 5.3: Work function change induced by the adsorption of water on a 24 MLE thick rutile(011)-(2x1) film at 100 K.

5.2.4 Conclusions –

H_2O interaction with epitactic rutile(011)-(2x1) films

The interaction of water with epitaxial rutile(011)-(2x1) films grown on a $\text{Re}(10\bar{1}0)$ single crystal surface was studied by means of TPD, $\Delta\Phi$ and LEED.

TPD spectra of water adsorbed on a 24 MLE thick rutile film at 95 K exhibit three resolved desorption states at ≈ 405 K (β_3), 300 – 271 K (β_2) and 220 – 186 K (β_1) and one state below 186 K (α), which is due to an ice layer formed on top of the monolayer at sufficiently low temperatures. In the following, the origins of the various H_2O binding states will be discussed:

THE β_1 STATE – The β_1 state possesses the by far highest intensity. Due to its similarities with the respective desorption states from rutile(110) and (100) single crystal surfaces [25, 24] and in view of UPS studies from water adsorbed on a rutile(011)-(2x1) single crystal surface [27, 28], the β_1 state can be clearly ascribed to molecular water bound to the oxygen atoms of the (011) surface via hydrogen bonds.

An interesting result of the present work is that – in the absence of multilayers (α) – water forms a (1x2) LEED superstructure on the rutile(011)-(2x1) surface²⁰ after a water exposure of ≥ 0.6 L at 174 K. The superstructure spots are most intense between 180 and 190 K and disappear around 225 K and are clearly associated with the β_1 state (see figure 5.14 on page 102). The respective adsorbed H_2O molecules do not lift or alter the inherent (2x1) reconstruction of the rutile (011) surface. Due to the narrow temperature range, in which the superstructure is visible, we conclude that it may be induced by half of the β_1 state population by filling every second trough of the rutile(011)-(2x1) surface.

THE β_2 STATE – Compared to the respective desorption states observed on ru-

²⁰The (1x2) refers to the rutile(011)-(2x1) reflexes.

tile(110) and (100) surfaces [25], the β_2 state at 300 – 271 K observed with our rutile films possesses a considerably lower intensity. This could be due to the rough film morphology, since a decreased intensity was observed at rough rutile single crystal surfaces as well [23, 24]. Another quite reasonable possibility is that the β_2 state indicates water desorption from patches of minority surface orientations present in the thin films, namely rutile(110) facets, which showed a significant influence already on the CO TPD spectra presented in the last section. Due to the existence of (110) facets and according to UPS studies, which revealed that molecular water leaves the (011)-(2x1) surface around 200 K [27], the β_2 state is assigned to molecular water adsorption at the Ti(V) centers of rutile(110) facets via the oxygen atom.

THE ORIGIN OF THE β_3 STATE – The main difference between the TPD spectra obtained from the rutile(011)-(2x1) films and the (110) and (100) surfaces is the existence of the β_3 state at ≈ 405 K, which is exclusively observed on the (011)-(2x1) surface. The CO/H₂O co-adsorption experiments and the temperature-dependent studies described in the subsections 5.1.3 and 5.1.4 revealed that the β_3 state has a strong influence on the CO desorption energies, in that it induces a significant temperature redshift of the CO TPD states, despite the very low water coverage above 350 K. Previous studies on a 36 MLE thick rutile film showed a more intense β_3 state, which is probably due to a higher ratio between (011)-(2x1) and (110) facets. Combined with the STM studies of De Valentin *et al.* [27] we strongly suggest that the β_3 state is induced by dissociatively adsorbed water on the rutile(011)-(2x1) surface. Due to its minor intensity we were unable to determine its desorption reaction order noting that one expects a second-order kinetics if the recombination of isolated H atoms and OH groups is the rate-limiting step. Furthermore, the STM images published by De Valentin *et al.* indicated that the hydroxyl groups are located on top of the oxygen rows [28, 27]. According to Henderson [25], the relative proximity (d) between the

fivefold coordinated surface titanium atoms (or rather the oxygen atom of the adsorbed water molecule) and undercoordinated oxygen atoms is critical when arguing whether or not a TiO_2 surface dissociates water. Dissociative adsorption occurs on rutile(100) ($d = 2.8 \text{ \AA}$) while molecular adsorption takes place on rutile(011) ($d = 3.2 \text{ \AA}$) [25]. Two shoulders at around 200 and 340 K are very likely due to contributions from water adsorbed on (100) facets on the film.

The TPD states of water on rutile(011)-(2x1) films are listed in table 5.4 together with the respective Redhead desorption energies and the proposed adsorption sites.

WATER-INDUCED WORK FUNCTION CHANGE – The work function change ($\Delta\Phi$) measurements revealed an overall change of $\Delta\Phi = -1 \text{ eV}$ due to the adsorption of 16 L H_2O . The main change, however, already occurred within the first 2 L of water adsorption ($\Delta\Phi(0 - 2 \text{ L}) = -774 \text{ meV}$). The plot exhibits a marked change after 2 L and minor changes after 0.5, 1.1, 4.4 and 6.9 L (see figure 5.16 in subsection 5.2.3). These changes can be attributed to the different H_2O TPD states. The strong change in the $\Delta\Phi$ slope from 189 to 55 meV/L at 2 L is a good indicator for the saturation of all monolayer states ($\beta_3, \beta_2, \beta_1$) and the onset of pure multilayer growth (α). The further changes at 4.4 and 6.9 L could be due to the completion of the first and the second multilayer. The information on the water-induced work function change is summarized in table 5.3 in subsection 5.2.3.

	α	β_1	β_2	β_3	220 K	340 K
T_{max} / K	≤ 186	220 – 186	300 – 271	405	≈ 220	≈ 340
$\Delta E_{des}^* (\text{RH}) / \text{kJ mol}^{-1}$	≤ 46	55 – 46	76 – 69	103	≈ 55	≈ 87
adsorption site	multilayer, ice	oxygen atoms of rutile(011)-(2x1) and partly (110) and (100)	Ti(V) centers of rutile(110)	rutile(011)-(2x1) maybe Ti(V) or oxygen vacancies	Ti(V) of rutile(100)	Ti(V) of rutile(100)
desorption kinetics	0^{th} order,	1^{st} order, molecular	1^{st} order, molecular	2^{nd} order, dissociative	1^{st} order, molecular	2^{nd} order, dissociative
references	[24, 23]	[24, 25, 27]	[24, 25, 23]	[27, 28, 25]	[25]	[25]

Table 5.4: Summary of the H_2O desorption states from a 24 MLE thick rutile(011)-(2x1) film; RH = Redhead, $\nu = 10^{13} \text{ s}^{-1}$.

5.3 Interaction of carbon dioxide with rutile(011)-(2x1) surfaces

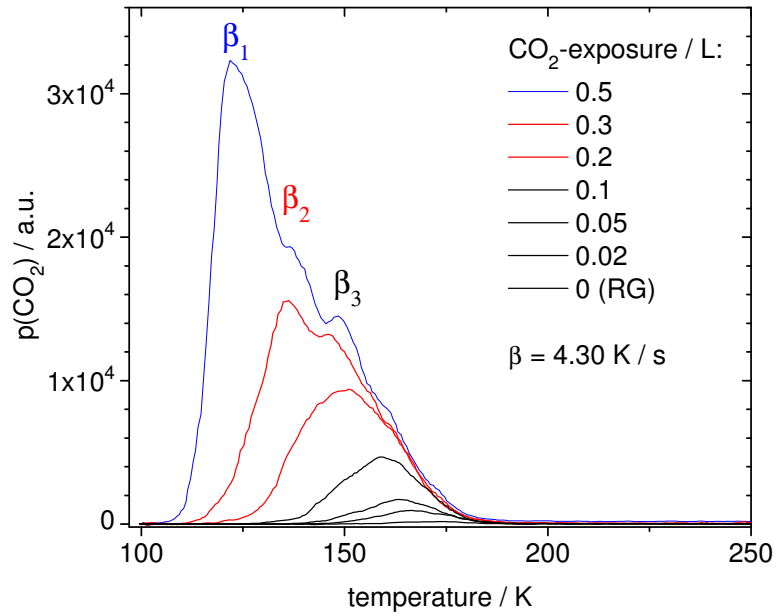
In this thesis, the CO₂ interaction with bare rutile(011)-(2x1) films is mainly studied in order to examine the differences in the adsorption between CO and CO₂, which is especially interesting, since CO₂ represents the product of the low-temperature CO oxidation. A comprehensive review about the surface chemistry of carbon dioxide was published by Freund and Roberts [89].

5.3.1 TPD of CO₂ from TiO₂(011)-(2x1)

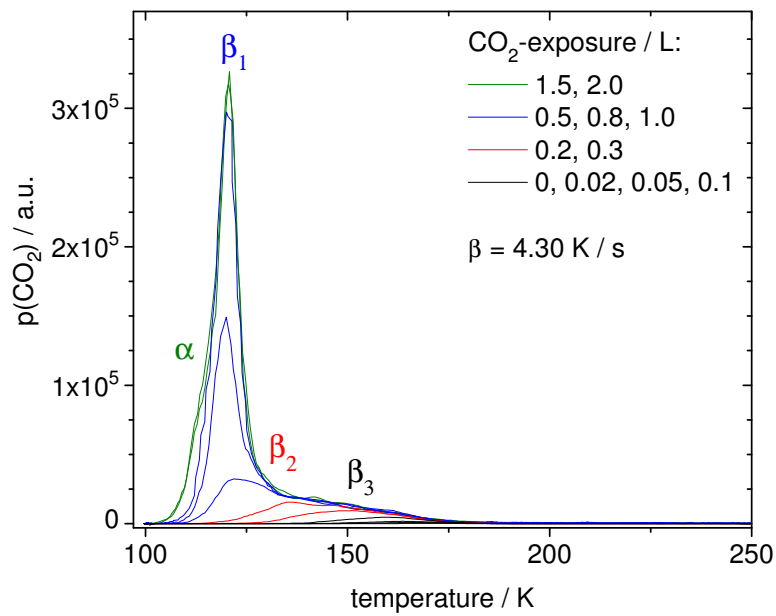
The CO₂ spectra (44 amu) were taken in the same way as the CO spectra (see section 5.1.1). Again, a 24 MLE thick rutile film was used as a substrate sample. Two different experiments were carried out. In the first one, the crystal was only heated to 290 K to mimic room temperature conditions. In the second one, it was heated to 410 K in order to remove residual water from the surface. Representative spectra are shown in figure 5.18 and 5.17, whereby the CO₂ exposure was varied from 0 to 2 L.

The TD curves obtained in the $T_{limit} = 410$ K series exhibit four desorption states located between 166 and 148 K (β_3), 136 K (β_2), between 122 and 120 K (β_1) and < 120 K (α). Figure 5.17a depicts the spectra after CO₂ exposures of 0 to 0.5 L and figure 5.17b the complete exposure series from 0 to 2.0 L.

At low exposures ≤ 0.1 L, the spectra exclusively contain the β_3 state between 166 (0.02 L) and 148 K (0.5 L), which saturates after exposures of about 0.3 L. The β_2 state shows only up as a small shoulder at 136 K and is visible only after exposures of 0.3 and 0.5 L. Larger CO₂ exposures (≥ 0.5 L) make the β_1 state appear, which possesses the highest intensity and saturates after a CO₂ exposure of about 1 L; its desorption temperature shifts only very slightly (by ca. 2 K) if

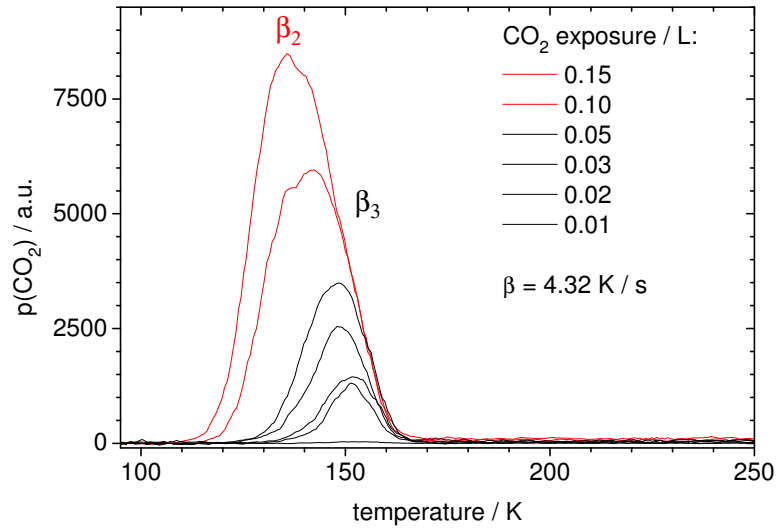


(a) 0 - 0.5 L, $T_{limit} = 410 \text{ K}$.

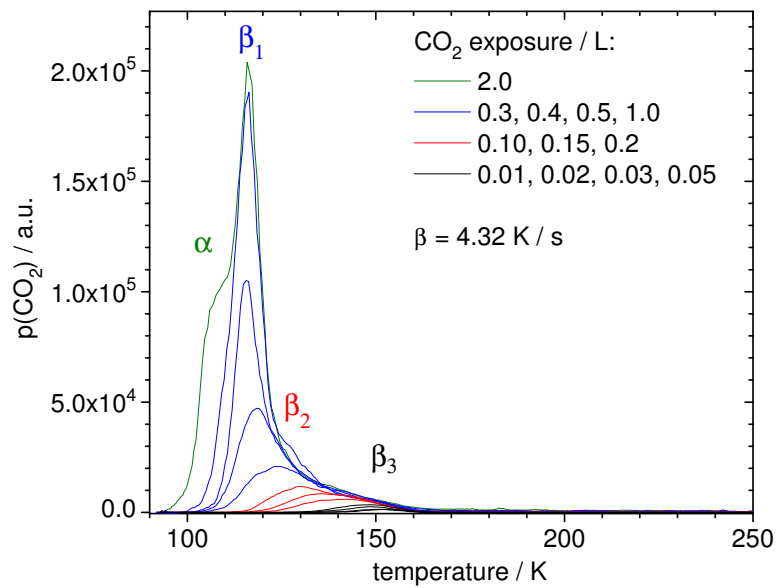


(b) 0 - 2.0 L, $T_{limit} = 410 \text{ K}$.

Figure 5.17: Series of CO₂ TPD spectra from a 24 MLE thick rutile(011)-(2x1) film with increasing CO₂ exposures; $T_{ad} = 100 \text{ K}$; $T_{limit} = 410 \text{ K}$.



(a) 0.01 - 0.15 L, $T_{limit} = 290$ K.



(b) 0.01 - 2.0 L, $T_{limit} = 290$ K.

Figure 5.18: Series of CO₂ TPD spectra from a 24 MLE thick rutile(011)-(2x1) film with increasing exposures; $T_{ad} = 95$ K; $T_{limit} = 290$ K.

the exposure is increased from 0.5 to 1.0 L. The required exposure of about 1 L for saturation of β_1 is compatible with the completion of a CO₂ monolayer.

The $T_{limit} = 290$ K series exhibits some minor derivations. The first difference is a general redshift of the peak maxima, which now appear between 152 (0 L) and 140 K (0.15 L) (β_3), 136 (0.1 L) and 123 K (0.3 L) (β_2), 119 (0.3 L) – 116 K (2.0 L) (β_1) and ≈ 108 L (α). However, the main difference is the missing CO₂ desorption intensity for $T > 163$ K in the 290 K series while in the 410 K series the CO₂ desorption persisted beyond 160 K up to 185 K.

The interaction of CO₂ with rutile(110) single crystal surfaces has been studied previously by Henderson and yielded two desorption states at 137 K and 166 K, respectively, after CO₂ adsorption at 118 K [26]. Comparative experiments on vacuum-annealed and nearly perfect (110) surfaces as well as co-adsorption experiments with water vapour suggested that the 137 K state reflects CO₂ molecules adsorbed at the Ti(V) centers of the (110) surface via the C-atom, while the 166 K state is induced by CO₂ adsorption on oxygen vacancies [26]. An additional desorption state at 200 K was attributed to bicarbonate formation and appeared after co-adsorption of water and CO₂ at 110 K on a vacuum annealed surface. Apart from this latter desorption state, CO₂ adsorbs in a similar way on various oxide surfaces of TiO₂ [26, 90, 91] and ZnO [92]. CO₂ TPD spectra from these surfaces usually exhibit two different states slightly above and below 150 K, whereby the state beyond 150 K is ascribed to CO₂ adsorption at oxygen vacancies or other defect sites (induced by sputtering, for example) and the state below 150 K is assigned to linear or slightly bended CO₂ adsorbed on the defect-free surface.

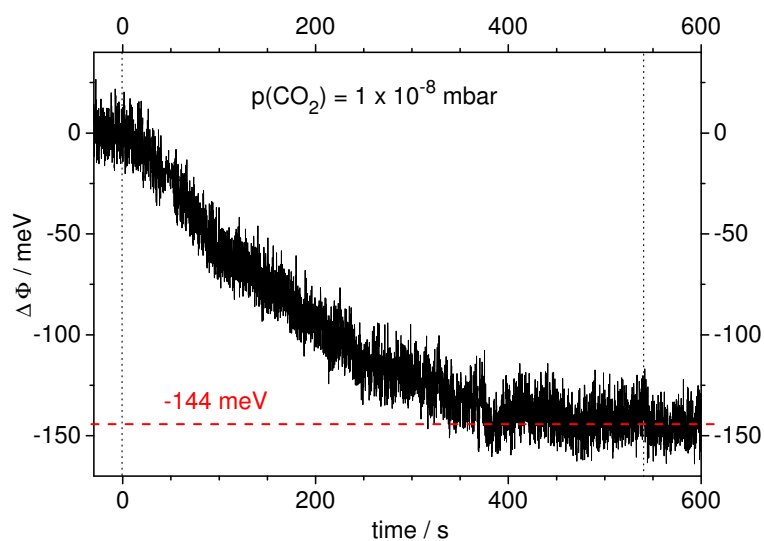
The weak β_2 state observed in both of our TPD series (290 K and 410 K) coincides with the 137 K state reported for rutile(110) [26], which suggests that it reflects CO₂ adsorption on the Ti(V) centers of the rutile(110) facets. The β_1 state,

which represents the largest contribution to the TPD spectra, is then presumably induced by CO₂ molecules that are adsorbed on rutile(011)-(2x1) parallel to the surface, perhaps in the trenches of the respective surface. However, without additional vibrational spectroscopy the local adsorption geometry cannot be determined with certainty. Compared to the adsorption behaviour of CO₂ on TiO₂(110) and ZnO(0001) mentioned above, the β_3 state is most likely due to CO₂ adsorption on defect sites. These defects can consist of oxygen vacancies or may represent low-coordinated sites at kinks and steps. This is also consistent with the increase of the β_3 state with increased T_{limit} , as the water molecules, which co-adsorb on these sites due to the unavoidable water partial pressure of the vacuum recipient, are removed upon heating to 410 K and the adsorption sites are therefore at the disposal of the CO₂ molecules.

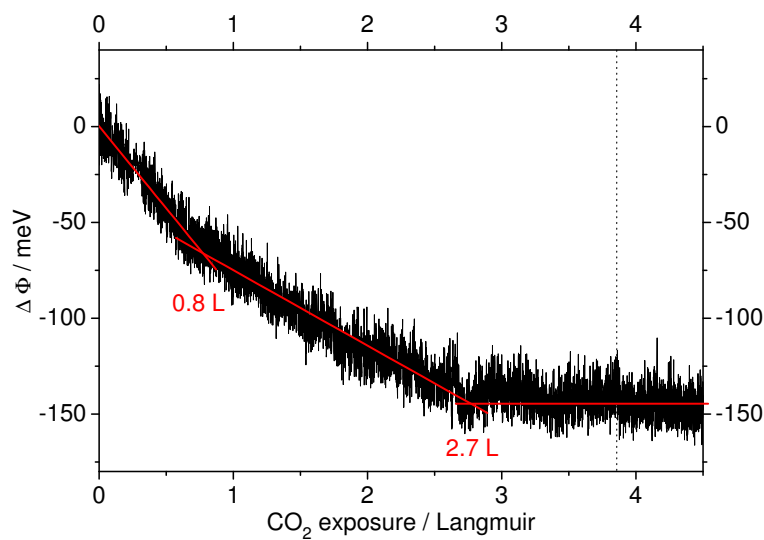
5.3.2 CO₂-induced work function change

The CO₂-induced work function change of a 24 MLE thick rutile(011)-(2x1) film has been measured at $T = 100$ K and is depicted in figure 5.19a as a function of CO₂ exposure time. The dotted vertical lines mark the opening and the closing of the CO₂ valve, respectively. Between these lines, a CO₂ pressure of $p(\text{CO}_2) = 1 \times 10^{-8}$ mbar was exposed to the rutile film surface. The work function decreases for 400 s and stays constant after this time. The total CO₂-induced work function change adds up to $\Delta\Phi(\text{CO}_2) = -144 \pm 10$ meV.

Integration of the CO₂ dosing pressure after the exposure time followed by division by the relative sensitivity factor of 1.4 for CO₂ (compared to 1 for the ionization of N₂) yields the CO₂ dose in mbar/s. The work function change is plotted against this dose (expressed in Langmuir) in figure 5.19b. The dotted vertical line again marks the switch off point of the CO₂ flow. The decrease is linear within the first 0.8 L with a gradient of -86 ± 1 meV L⁻¹ and from 0.8 to 2.7 L with a smaller gradient of -39 ± 1 meV L⁻¹. After 2.7 L, the work function



(a) Plot of the CO₂ induced work function change versus the exposure time.



(b) CO₂ induced work function change plotted against the CO₂ dose in Langmuir. The red lines indicate the average slope of the plot.

Figure 5.19: CO₂-induced work function change on a 24 MLE thick rutile(011)-(2x1) film. $T_{ad} = 100$ K.

stays constant.

Compared to the work function change induced by CO and H₂O, the CO₂-induced work function change of -144 meV is relatively low and indicates a weak interaction of the CO₂ molecules with the rutile surface, which is consistent with the TPD spectra that do not reveal special desorption features compared to other oxide surfaces either. The decrease indicates that CO₂ acts as a weak electron donor to the rutile film [84].

5.3.3 Conclusions –

CO₂ interaction with epitaxial rutile(011)-(2x1) films

The CO₂ adsorption on 24 MLE thick rutile films was studied by means of TPD and work function change measurements. The TPD spectra exhibit three desorption states above 100 K that do not differ significantly from CO₂ desorption states that have been reported for rutile TiO₂(110) single crystal surfaces [26, 90, 91].

THE β_3 STATE at 166 – 148 K, which saturates after CO₂ exposures of 0.3 L in the $T_{limit} = 410$ K series, is assigned to CO₂ adsorption on defect sites (oxygen vacancies and low-coordinated atoms at kink and step sites).

THE β_1 STATE at 122 – 120 K is the most intense CO₂ desorption state. It appears first after 0.5 L CO₂ exposure and saturates after 1 L. A small shoulder is visible at its high-temperature side at 136 K (β_2), which is consistent with the CO₂ desorption state observed on rutile(110) that was assigned to horizontal CO₂ adsorption at the Ti(V) centers of the (110) surface [26]. The β_1 state is assigned to horizontal CO₂ adsorption on rutile(011)-(2x1).

The CO₂ desorption states obtained from a 24 MLE thick rutile film are listed with the respective Redhead desorption energies and the presumed adsorption sites in table 5.5.

CO₂ induces only a very weak work function change of -144 meV on rutile(011)-(2x1), which indicates a weak electron donating interaction with the surface.

5.3 Interaction of carbon dioxide with rutile(011)-(2x1) surfaces

	α	β_1	β_2	β_3
T_{max} / K	< 120	122 – 120	136	166 – 148
ΔE_{des}^* (Redhead) / kJ mol ⁻¹	< 30	30	34	41 – 37
CO adsorption site	multi-layer	Ti(V) in the valleys of rutile(011)-(2x1)	Ti(V) centres, rutile(110)	oxygen vacancies, kinks and steps
desorption kinetics	0 th order molecular	1 st order, molecular	1 st order, molecular	1 st order, molecular
references			[26, 90, 91]	[26, 93, 90, 91]

Table 5.5: Summary of the CO₂ interaction with epitaxial rutile (011)-(2x1) films grown on a Re(10 $\bar{1}$ 0) single crystal surface. $\nu = 10^{13} \text{ s}^{-1}$.

6 Chemical reactivity of rutile(011)-(2x1) films covered with gold: Adsorption of CO, CO₂ and H₂O

6.1 The interaction of the Au/TiO₂ films with carbon monoxide

6.1.1 TPD of CO from Au/TiO₂(011)-(2x1)

In order to mimic model catalyst surfaces, the prepared rutile films were partially covered with gold by vapour deposition from a home-made Au evaporator (see section 3.3). The evaporation rate was kept constant by choosing a constant Au source temperature. A temperature control of the Au source was provided by a thermocouple (type D, W-3% Re/W-25% Re) mounted directly to the gold supply; usually, a constant thermovoltage of 21.55 mV (= 1443 K) was chosen. The distance between the evaporator and the sample was about 10 cm in order to achieve a homogeneous Au deposition. With a constant gold flux given, the deposition *time* is a reliable (although only relative) measure for the actual gold coverage θ_{Au} , provided the gold condensation coefficient does not depend on

θ_{Au} . Without a quantitative determination of the Au surface concentration (for example, by STM imaging), absolute values of θ_{Au} cannot be given. However, some preliminary experiments with a quartz microbalance and Auger electron–spectroscopy revealed a nominal Au deposition rate of about 0.5 MLE per minute. After a defined Au deposition, the sample was cooled to 100 K and exposed to various amounts of carbon monoxide, before the TPD experiment was started. Figure 6.1 presents a series of CO TPD spectra taken from model catalysts with different initial gold coverages (indicated by the Au deposition time).

After 15 s Au evaporation (figure 6.1a), the low–temperature part of the CO TPD spectrum ($T \leq 175$ K) appears to be almost identical to the CO desorption spectra from bare rutile films (see figure 5.1 on page 73). The only difference consists in a broad additional desorption state (γ) around 230 K leading to the situation that CO desorption intensity appears at temperatures of more than 300 K. This additional γ state (which apparently constitutes the influence of the Au deposit) gains intensity in the spectra obtained from the samples with gold deposition times of 30 and 60 s, its maximum shifts downwards to 222 and 210 K at CO saturation, respectively. The 30 and 60 s spectra still feature a considerable amount of CO desorption intensity above 300 K. After 180 s, the γ state has gained even more intensity and is shifted to 196 K at saturation. This continuous redshift of the CO TPD maximum causes a complete CO desorption below 300 K now. At 600 and 1200 s, the γ state moves even further towards the low temperature side (186 and 180 K), CO desorption is well completed below 300 K.

The temperature progression of the γ peak maximum is plotted against the Au evaporation time in figure 6.2, whereby the temperature of the peak maximum (T_{max}) was determined from the spectrum with the highest CO exposure of each series. The total redshift of the maximum of the γ state adds up to 50 K from 15 s to 1200 s Au deposition time ($\theta_{Au} = 0.1 - 10$ MLE).

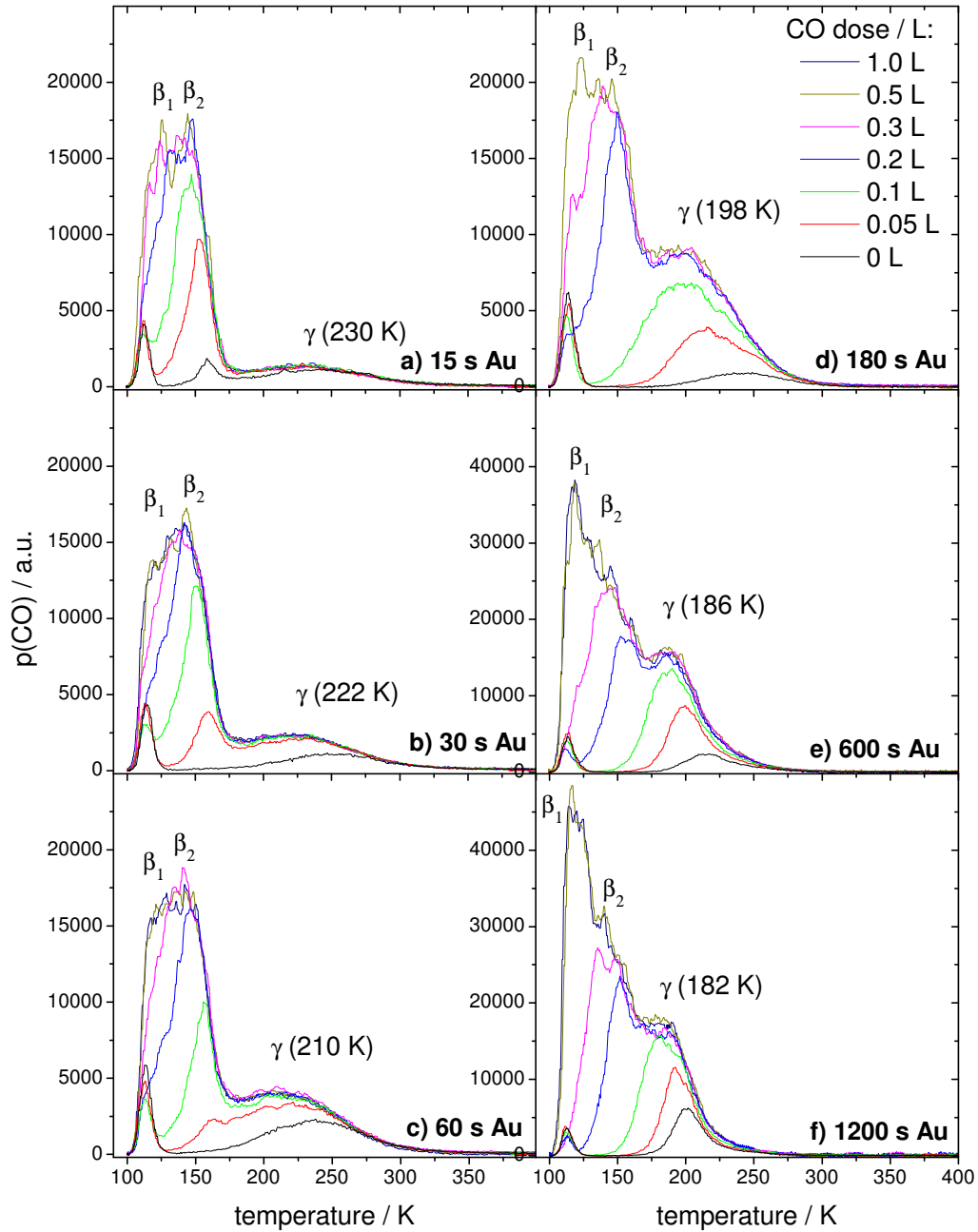


Figure 6.1: CO TPD spectra taken from Au/rutile(011)-(2x1)/Re($10\bar{1}0$) model catalysts covered with different amounts of gold. The amount of deposited gold is expressed in terms of the gold deposition time. Rutile film thickness ≈ 24 MLE, $T_{ad} = 100$ K, $T_{limit} = 400$ K, $\beta = 4.3$ K/s.

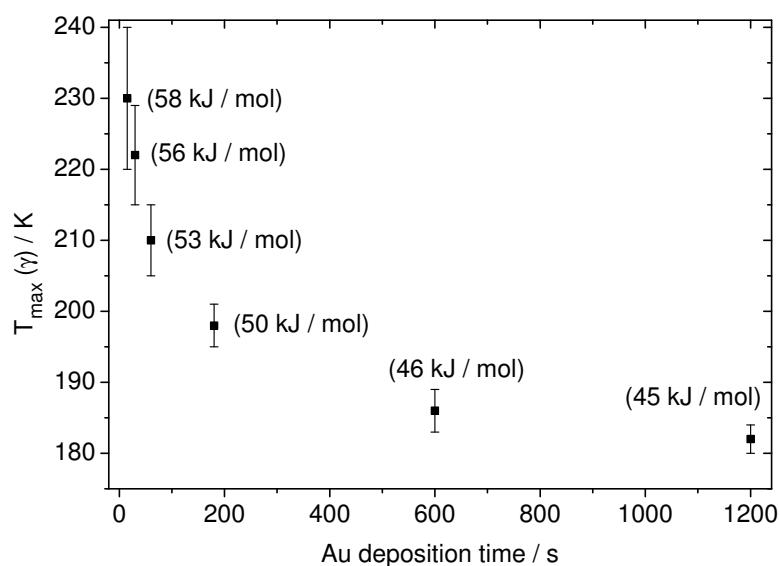


Figure 6.2: Progression of the peak maximum of the γ state plotted versus the Au deposition time (with the respective Redhead desorption energies in brackets, $\nu = 10^{13} \text{ s}^{-1}$).

Besides the considerable redshift of the γ peak maximum with increasing Au coverages, another property of γ is remarkable, too, especially with regard to the interaction of CO with catalyst surfaces at room temperature. Meant is the amount of CO that exists on the surface at a given temperature. For three such temperatures, namely 100, 200 and 300 K, this residual CO coverage is plotted versus the gold deposition time (figure 6.3). The residual coverage was determined from the 0.5 L spectrum of each series; values were taken for 100, 200 and 250 K. At 300 K, the respective CO coverage is insignificant, although not zero. Figure 6.3 reveals an unambiguous trend:

The overall CO coverage of the samples, which can be inferred from the 100 K graph, increases by a factor of 2.8 when going from the “15 s” ($\theta_{\text{Au}} \approx 0.1 \text{ MLE}$) to the “1200 s” ($\theta_{\text{Au}} \approx 10 \text{ MLE}$) surface. The CO yield seems to saturate around 1200 s for CO adsorption at 100 K. The 200 K graph exhibits a coverage maximum for the sample that contains an amount of Au that is equivalent to 180 s

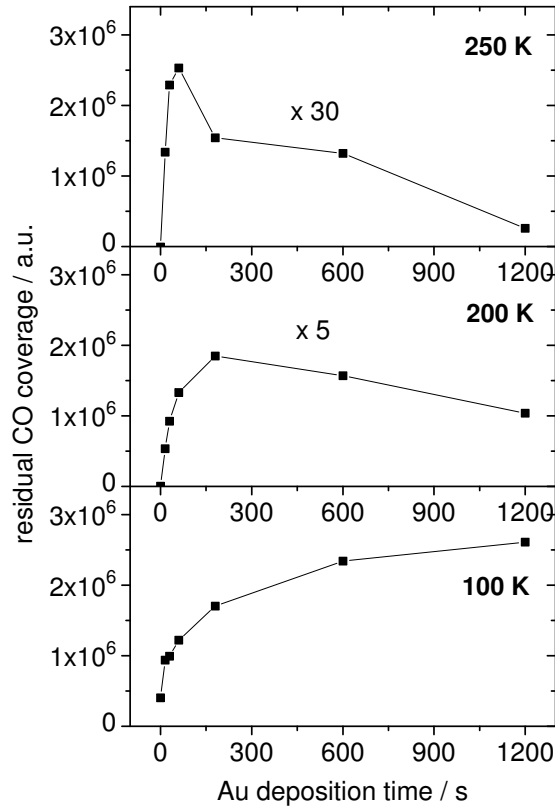


Figure 6.3: Residual CO coverage at 100, 200 and 250 K (from bottom to top) plotted versus the Au deposition time for 0.5 L spectra.

deposition time ($\theta_{Au} \approx 1.5$ MLE). Here, the remaining CO coverage rises strongly from 15 to 180 s and decreases slowly after 180 s. At 250 K, the graph reveals a CO coverage maximum after 60 s ($\theta_{Au} \approx 0.5$ MLE) Au deposition time.

The situation can be summarized as follows. Deposition of Au onto epitaxial rutile(011)-(2x1) films causes an additional broad CO desorption state (γ), whose desorption maximum (and, hence, whose adsorption energy) varies significantly with the Au precoverage. Plots of the remaining CO coverage on the sample at 100, 200 and 250 K versus the Au deposition time yield CO coverage maxima for samples with different amounts of deposited gold (depending on the chosen tem-

perature). Lower Au coverages cause a larger amount of more strongly adsorbed CO, while samples with higher Au coverages lead to an increase in the amount of adsorbed CO at 100 K, but a decrease in the strongly bound CO species.

The width of the γ state indicates that a variety of adsorption sites with slightly different properties contribute to this state. A closer look on the TPD spectra of figure 6.1 reveals indeed that the γ state consists at least of two different maxima, located approximately at 180 K and 195 K (for the 1200 s series).

For a better understanding of the CO binding situation on the TiO₂ + Au surfaces, it is worth to examine the detailed preparation conditions of the Au covered samples: First, Au is deposited onto the rutile surfaces that are kept at 300 K. Then, the sample is cooled to 100 K by means of liquid nitrogen, a process that lasts ca. 15 minutes. In order to remove spurious contaminants (mainly CO that degases from the warm Au source during the Au deposition), the crystal is then once heated up to 400 K and cooled to the adsorption temperature of 100 K before the CO exposure is performed and the TPD series is started. Note that the crystal is heated to 400 K in every TPD spectrum ($T_{limit} = 400$ K) of the subsequent series. During the first heating process to 400 K directly after the gold deposition at 300 K and subsequent cooling to 100 K, a spectrum was recorded as well (CO exposure from the residual gas). This first spectrum is referred to as “virgin” in the following. The next spectrum (again CO exposure from the residual gas) takes place on the pre-annealed surface and is therefore referred to as “pre-annealed”. This “pre-annealed” spectrum is identical with the “0 L” spectrum of each series in figure 6.1. These two subsequent spectra are depicted in figure 6.4 for increasing Au coverages (indicated by four different gold deposition times of 15, 30, 60 and 180 s) and underline that the pretreatment history of the samples has a major influence on the CO binding situation.

In contrast to the “pre-annealed” second spectra, the first “virgin” ones exhibit

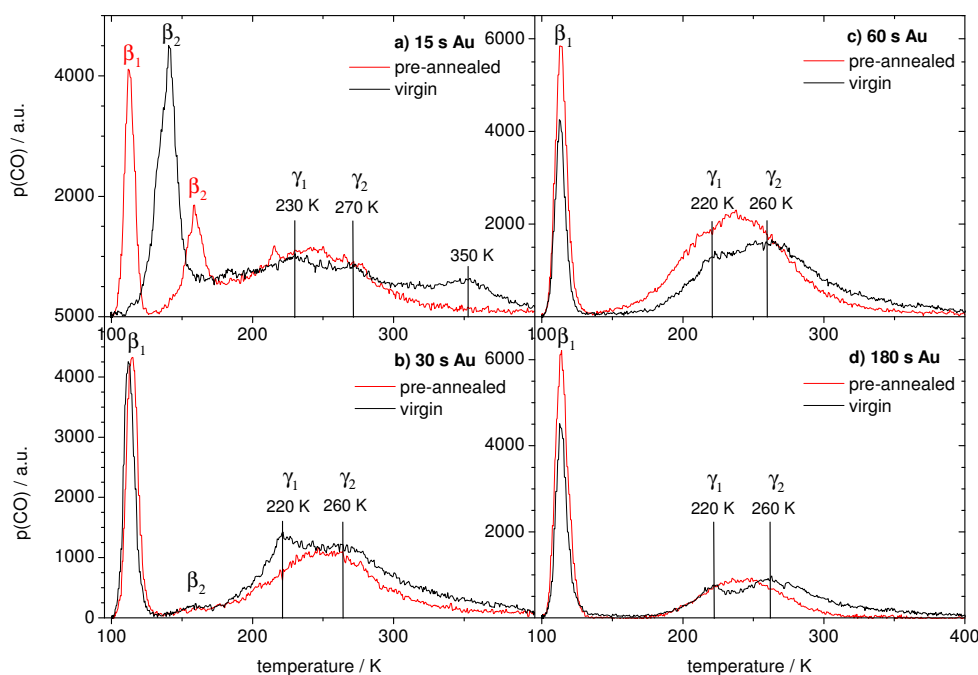


Figure 6.4: Comparison of the first “virgin” and the second “pre-annealed” spectra of the TPD series for rutile films covered with different amounts of gold (deposition times of 15, 30, 60 and 180 s). The “virgin” spectra were recorded directly after the Au deposition at 300 K and subsequent cooling to 100 K, the “pre-annealed” spectra were obtained after the “virgin” ones. The spectra that were recorded subsequent to the “pre-annealed” spectra did not exhibit further changes.

a gamma state, which consists of two resolved states with temperature maxima at around 220 (γ_1) and 260 K (γ_2). Furthermore, these virgin spectra show desorptive CO contributions up to 400 K. This comparison explicitly shows that Au-covered rutile samples result in the formation of more favourable CO binding sites, i.e., sites with higher binding energies. Subsequent annealing, however, has the effect that the favourable binding sites are reduced and are increasingly displaced by less favourable adsorption sites. The possible reason for this behaviour may be sought in thermally activated restructuring processes of the surfaces,

i.e., Au diffusion and agglomeration, sintering and related phenomena. Prior to the annealing process to 400 K the surface seems to provide two main kinds of adsorption sites, while a less defined distribution is available afterwards.

Processes of this kind are well-known from similar systems and have been described frequently in the literature (see, for example, [14, 94, 61, 95]). Usually, Au grows onto oxide surfaces according to a Volmer–Weber mechanism [7], i.e., does not really wet the surface, but exists as three-dimensional nuclei, which agglomerate with increasing deposition. In this way, a relatively inhomogeneous Au distribution results, providing a whole variety of differently coordinated adsorption sites for CO. These Au particles were found to sinter together when annealed to 770 K [14], which yields a decrease of one and two layer high particles in favour of higher particles. Besenbacher *et al.* observed sintering of Au particles (3% ML Au) on rutile(110) already at 68°C [61].

CO adsorption from a Au(110)-(1x2) reveals one desorption state above 100 K between 75 and 180 K with a maximum at $T_{max} = 145$ K ($\Delta E_{des}^*(Redhead) \approx 35$ kJ/mol) [96, 97]. On sputtered Au surfaces, this desorption state has its maximum at about 180 K [97]. These spectra from Au(110)-(1x2) bear some resemblance to the CO TPD spectra obtained from our Au/TiO₂ samples with relatively high Au coverages of 5 MLE (600 s deposition time) and 10 MLE (1200 s deposition time (see figures 6.1e,f). At these high nominal Au coverages, it is likely that the Au clusters have agglomerated sufficiently to reveal a similar surface as a sputtered gold single crystal.

The split γ state indicates that mainly two different kinds of adsorption site are induced by the gold deposition, which could be due to CO adsorption on Au particles of different size or to different adsorption sites on the same particles [98, 99]. The γ_2 state at 260 K may, for example, be induced by CO adsorption on the edges of the gold particles, while the γ_1 state reflects CO adsorbed on the

terraces of the Au particles [33, 100]. For high Au coverages the ratio between the edges and the terraces decreases and the maximum of the overall γ state shifts to lower temperatures.

The first TPD spectrum that was recorded directly after the first 15 s of Au deposition ($\theta_{Au} \approx 0.1$ MLE) even exhibits a small desorption state with a visible maximum at 350 K instead of a diffuse high-temperature tail (see figure 6.1a). This maximum could be due to adsorption at very small Au clusters or even single gold atoms. Another possibility is that OH groups play a role in the existence of the 350 K state, since the redshift of the β_2 maximum in figure 6.4a indicates that OH groups are present on the surface (see section 5.2). Matthey *et al.* deposited Au onto three different $\text{TiO}_2(110)$ surfaces, namely an oxidized, a reduced and a hydrated one (vacancies filled with hydroxyl groups) and observed that gold nanoclusters nucleate homogeneously on the terraces of the reduced and oxidized supports, whereas clusters form preferentially at the step edges on the hydrated $\text{TiO}_2(110)$ surface [101]. This may suggest that the weak CO desorption state at 350 K is induced by CO adsorption on gold clusters that are formed on step edges of the rutile film, while the γ_1 and γ_2 states may be assigned to CO adsorption on gold clusters deposited on the rutile terraces.

6.1.2 CO-induced work function change on Au/TiO₂

The work function change induced by CO adsorption on a sample, which consists of a 24 MLE thick rutile(011)-(2x1) film covered with 1200 s Au (the sample is identical with the 1200 s one that was investigated by CO TPD in figure 6.1), was again studied by the self-compensating Kelvin probe method. For the measurement, the catalyst was exposed to 1×10^{-8} mbar CO at a substrate temperature of 100 K. The results are presented in figure 6.5. In (a), $\Delta\Phi$ is plotted against the CO exposure time, the CO valve was opened at 0 s and closed at 925 s (marked by the vertical dotted lines). The overall work function change adds up

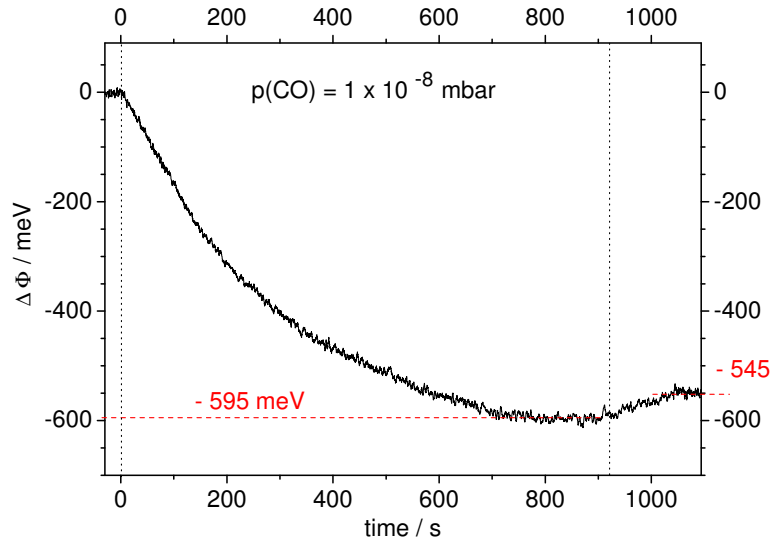
to $\Delta\Phi = -595$ meV after 700 s. Closing the CO valve after 925 s results in a $\Delta\Phi$ increase of 50 meV, thereby indicating partially reversible CO adsorption. Figure 6.5b shows the plot of $\Delta\Phi$ versus the CO exposure. The work function change is constant after a CO exposure of about 5.5 L. If the reversible part of the work function change is subtracted, the overall work function change adds up to $\Delta\Phi = -545$ meV, which is reached after a CO exposure of 4 L (the value of -545 meV is marked by the horizontal dotted line in figure 6.5). The $\Delta\Phi$ decrease is linear with exposure during the first 1.3 L without any breaks or bends.

A comparison to the CO-induced work function change on bare rutile(011)-(2x1) films of the same thickness reveals that the change on the partially Au-covered TiO₂ surfaces is by a factor of 4 higher than on the bare TiO₂ films (see subsection 5.1.5)¹. This agrees well with the CO yield obtained with the “1200 s Au” sample in TPD (see figure 6.3), which is by a factor of 4 higher than the CO yield from the 24 MLE rutile film in subsection 5.1.1.

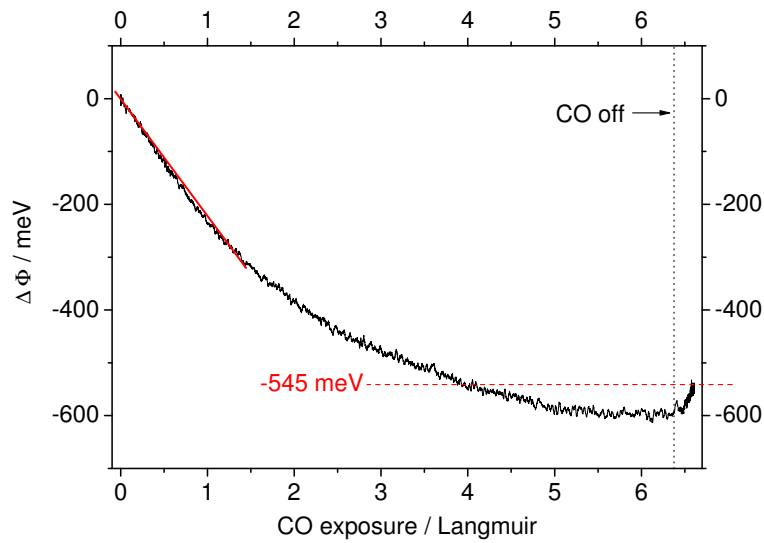
According to Göpel’s model for the interaction of small gas molecules with oxide surfaces [84], the decrease of the work function due to CO adsorption indicates that CO acts as an electron donor. The Au deposition onto the rutile surface does not seem to change this behaviour. A negative work function change of almost -1 eV is reported for the CO adsorption on Au(110)-(1x2) at 28 K [96]. CO adsorption on Au(332) [102] and (100) [103] surfaces yielded comparable values.

Since no significant deviations are observed when the CO induced work function change on the gold-covered sample is compared to both the $\Delta\Phi$ studies on the bare rutile films (presented in section 5.1.5) and the studies on Au single crystal surfaces reported in the literature [96, 102, 103], it is likely that the $\Delta\Phi$ data of CO adsorbed on a gold covered rutile(011)-(2x1) film mainly reflect the increase of the CO uptake with increasing Au coverage, which is consistent with

¹ $\Delta\Phi(\text{CO}/\text{TiO}_2) = -155$ meV, $\Delta\Phi(\text{CO}/\text{Au}/\text{TiO}_2) = -595$ meV.



(a) Plot of the CO-induced work function change against the exposure time.



(b) CO-induced work function change plotted versus the CO exposure. The horizontal line marks the $\Delta\Phi$ value of -545 meV and the vertical line the closing of the CO valve.

Figure 6.5: CO-induced work function change ($\Delta\Phi$) on a 24 MLE thick rutile(011)-(2x1) film covered with 1200 s Au; $T_{ad} = 100$ K.

the increased CO yield that was obtained in the TPD spectra (see figure 6.3).

6.2 Interaction of water with Au/TiO₂

The TPD spectra of water adsorbed on an Au-covered model catalyst (60 s Au deposition time) do not exhibit significant differences compared to the spectra obtained from bare rutile films (see section 5.2). The spectra show a more pronounced α^* state with a better resolved peak maximum at 173 K after an H₂O exposure of 2 L, which is – in the bare rutile spectra – only visible as a shoulder (see figure 5.9b). We recall that the α state has been assigned to the growth of ice layers (multilayer regime) on rutile(011)-(2x1).

Figure 6.6 presents co-adsorption experiments of water and CO on a rutile(011)-(2x1) film covered with 0.5 MLE gold (Au deposition time = 60 s). The upper graph shows the desorption of H₂O, the lower one the desorption of CO. To obtain these data, CO was adsorbed onto an H₂O pre-covered surface at 100 K. The amount of preadsorbed H₂O was between 0.1 L and 2 L, i.e., sufficient to cover the whole submonolayer and monolayer regime. The two masses (18 amu and 28 amu) were recorded simultaneously. A comparison of the spectra demonstrates that water occupies or blocks the CO adsorption sites on the rutile surface first before the CO adsorption sites on Au are occupied. The 1 L H₂O TPD spectrum, which corresponds to the H₂O monolayer desorption states on rutile, induces a strong decrease in the CO desorption states (β_1, β_2 , compare subsection 5.1.1) from rutile(011)-(2x1) and leaves the contributions from CO adsorbed on Au (γ , compare to figure 6.1) almost unchanged. The adsorption of 2 L water results in a separate H₂O state at 173 K (α^*) and induces a decrease of the high-temperature side of the CO/Au-desorption state. The low-temperature side of the CO desorption state is less intense as well, which is most likely due to the complete occupation of the CO adsorption sites on rutile by water molecules. The CO

intensity drop on the high-temperature side around 200 K is very likely induced by the adsorption of water molecules on the Au particles [104], since it yields a decrease in the γ state, which was assigned to the CO adsorption on Au.

Summarized, the deposition of Au onto epitaxial rutile(011)-(2x1) films does not lead to especially attractive new binding sites for water molecules. On the contrary, water adsorbs only very weakly on the Au-induced adsorption sites, which exhibit the highest binding energy for CO adsorption. The associated H₂O TPD state is in the range of water condensation with a desorption maximum at 173 K. The respective Redhead desorption energy is determined to $\Delta E_{\text{des}}^* = 43 \text{ kJ mol}^{-1}$ ($T_{\text{max}} = 173 \text{ K}$, $\beta = 4.33 \text{ K/s}$, $\nu = 10^{13} \text{ s}^{-1}$).

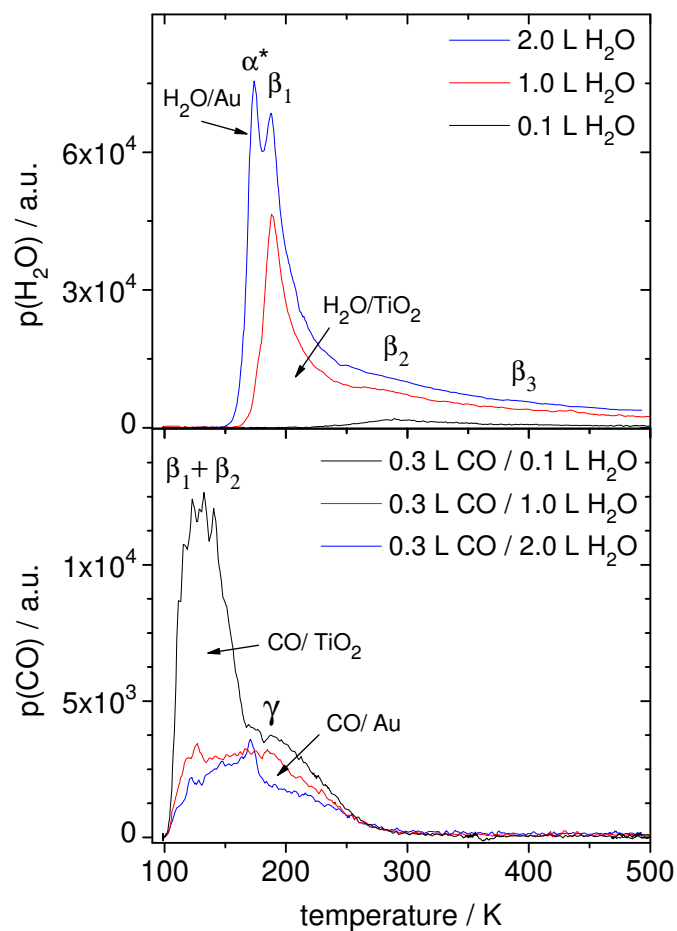


Figure 6.6: Water (top) and CO (bottom) TPD spectra after CO adsorption onto a water pre-covered Au/TiO₂/Re model catalyst at 100 K. $\beta = 4.33 \text{ K} / \text{s}$.

6.3 CO₂ interaction with Au/TiO₂

The CO₂ TPD spectra obtained for the adsorption of CO₂ on a gold covered rutile(011)-(2x1)/Re(10 $\bar{1}$ 0) sample (Au coverage \approx 5 MLE, deposition time = 600 s) at 100 K are depicted in figure 6.8. They do not exhibit significant changes compared to the spectra obtained from the bare rutile(011)-(2x1) film discussed in section 5.3, merely the total CO yield differs slightly. This is shown in figure 6.7, which compares the CO yields obtained from the bare rutile film as well as from the Au covered sample. CO₂ adsorbs on Au(110)-(1x2) exclusively below 100 K, which does not seem to be very different for the Au-covered rutile film [96]. The maximum CO₂ yield obtained from the Au-covered film (600 s

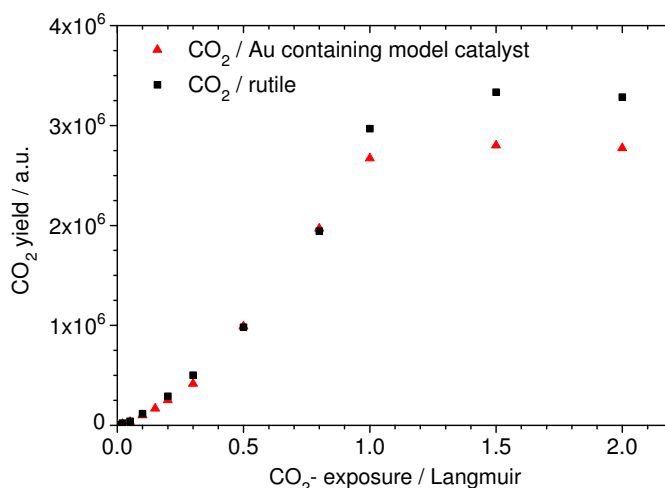
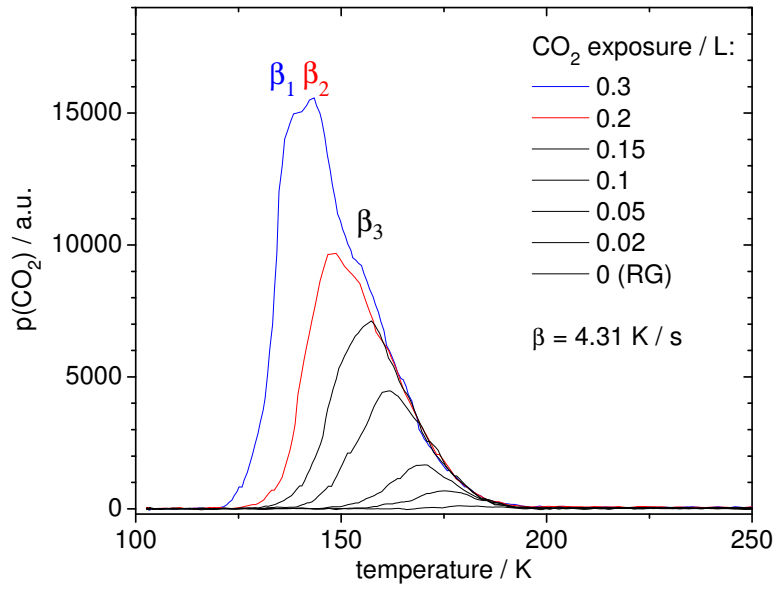
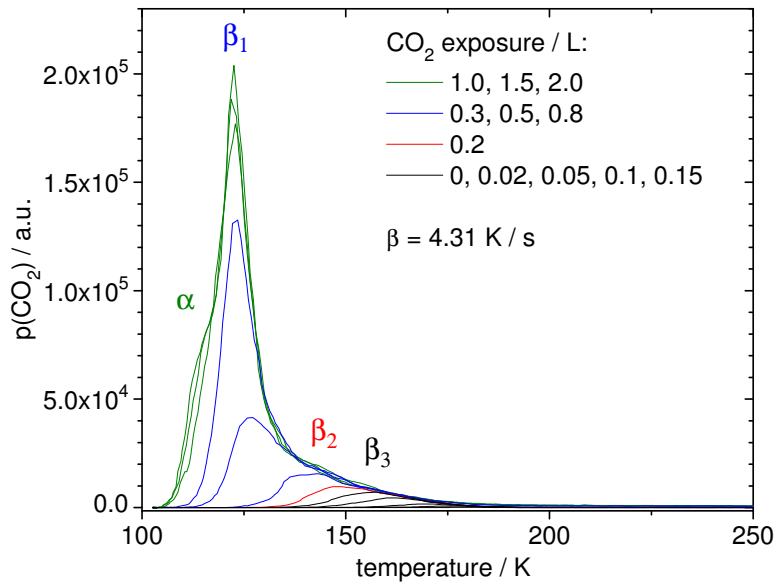


Figure 6.7: Plot of the CO₂ yields obtained from a 24 MLE thick bare rutile(011)-(2x1) film (squares) and a Au covered model catalyst.

Au, 5 MLE) is merely 20 % lower than the CO₂ yield from the bare rutile film, whereby differences become apparent only for exposures above 1 L. Qualitatively, these data show that for a TiO₂ surface, which was exposed to an Au flux for 600 s and therefore exhibits a nominal gold coverage of ca. 5 MLE, only a minor fraction of the rutile film is actually covered with gold since it is very unlikely



(a) 0 – 0.3L



(b) 0 – 2L

Figure 6.8: CO₂ TPD series obtained from a gold covered Au/rutile(011)-(2x1)/Re(10 $\bar{1}$ 0) model catalyst. $T_{ad} = 100$ K.

that CO₂ adsorbs on the gold particles with exactly the same adsorption energy as on the rutile film.

Of course, another possibility is that the CO₂ adsorbate on rutile(011)-(2x1) does not reach monolayer saturation at 100 K and consequently the obtained CO yield for the bare film depicted in figure 6.7 does not represent a completely covered monolayer. In this latter case, the comparison of the CO₂ yields is not very revealing regarding the ratio of Au-covered to bare rutile film.

At any rate, the CO₂ exposure of 1 to 1.5 L required to saturate the CO₂ uptake on a bare 24 MLE thick rutile(011)-(2x1) film seems to be in a reasonable range to assume monolayer saturation, especially when compared to the required H₂O exposure of about 1.5 L for saturation of the water monolayer on rutile(011)-(2x1) and the very low CO exposure of about 0.4 L that is definitely not sufficient for the saturation of a monolayer on rutile(011)-(2x1). Qualitatively, it is obvious that a considerable part of the rutile surface is not covered after depositing Au onto the surface for 600 s under the applied conditions. This part accounts for up to 80 % of the surface.

Preliminary experiments with a quartz microbalance and Auger electron-spectroscopy, respectively, revealed that the Au deposition rate amounts to about 0.5 MLE² per minute. This deposition rate would yield a nominal coverage of 5 MLE Au for the model catalysts used in the CO₂ desorption experiments. If we assume that these 5 MLE cover only 20 % of the rutile surface, the average gold cluster had an approximate height of 25 layers. Although this is certainly only a crude estimate, it nevertheless indicates that gold exhibits a 3-dimensional cluster growth mode on the rutile films. This conclusion is consistent with the currently existing growth models for Au on oxide surfaces (see, for example, [76, 7]), where

²One MLE is here defined as the amount of gold, whose weight is attributed to one layer of gold (111) by the quartz microbalance and which induces a sudden change in the slope of the Auger progression for Au deposition on Re(10 $\bar{1}$ 0).

the large differences in the surface free energies between the metal and the oxide prevent pronounced wetting. An exception is perhaps the growth of Au on very thin TiO_x films grown on a Mo(112) substrate, which was recently reported to proceed layer-by-layer [105].

6.4 Conclusions – The influence of gold on the adsorptive properties of CO , CO_2 and H_2O on epitaxial rutile films

Partially gold-covered rutile films were prepared by vapour deposition of Au onto epitaxial rutile(011)-(2x1) films grown onto a rhenium($10\bar{1}0$) surface.

The adsorption of CO_2 as well as H_2O at 100 K is not markedly influenced by the presence of Au. Merely the obtained gas yields in the desorption spectra are smaller and saturate after lower exposures.

The H_2O desorption state associated with desorption from the gold clusters appears at 173 K, which is comparable to H_2O desorption from single crystalline Au surfaces [104].

The CO_2 TPD spectra from Au/ TiO_2 do not exhibit additional desorption states above 100 K. This is not surprising, since CO_2 desorption from Au(110)-(1x2) occurs below 100 K [96].

Summarized, the deposition of gold onto rutile(011)-(2x1) films does not result in the creation of especially attractive new binding sites for CO_2 and H_2O ; the respective TPD spectra only exhibit contributions that are also observed on the single components.

In contrast to that, the CO interaction with rutile(011)-(2x1) films is influenced

significantly by the deposition of gold. CO TPD spectra of partially gold-covered rutile films with nominal coverages of $\theta_{Au} = 0.1 - 10$ MLE exhibit a broad additional desorption state (γ), whose maximum shifts from 230 K to 180 K with increasing gold coverage. These high binding energies were neither observed on pure titania nor on gold samples.

For high gold coverages above 5 MLE the spectra reveal some resemblance to desorption spectra obtained from sputtered gold surfaces [96]. Unannealed “virgin” surfaces with gold coverages ≤ 1.5 MLE reveal a split γ state at around 220 K (γ_1) and 260 K (γ_2). Spectra of samples with very low Au coverages of 0.1 MLE and hydroxyl groups present on the surface even exhibit a resolved desorption state at 350 K.

These desorption contributions may be assigned to CO desorption from the terraces (γ_1) and the borderline (γ_2) of the gold particles as well as from small Au particles grown on step edges of the rutile film (350 K state).

7 Summary

The present thesis is concerned with the influence of Au on the adsorptive properties of CO, CO₂ and H₂O on epitaxial rutile(011)-(2x1) films grown onto a Re(10 $\bar{1}$ 0) single crystal. The rutile films exhibit a Stranski–Krastanov growth mode and possess rutile(011)-(2x1) (on top) islands with (011)-(2x1) and (110) oriented facets at the sides. Partially Au-covered samples were prepared by vapour deposition of Au onto the titania films. Au exhibits a 3-dimensional growth mode (Volmer–Weber) and forms clusters on the rutile surface.

TPD spectra of CO adsorbed on rutile at 100 K show two desorption states (β_1 and β_2) below 180 K, which are assigned to molecular CO adsorption at the Ti atoms of rutile(011)-(2x1) (β_1) and rutile(110) (β_2), respectively, and cause an integral work function change of $\Delta\Phi = -155$ meV.

CO₂ adsorbs only weakly on rutile, too. The respective desorption states at 120 K (β_1), 136 K (β_2) and 148 K (β_3) are associated with CO₂ desorption from the Ti atoms of rutile(011)-(2x1) (β_1) and rutile(110) (β_2), respectively, as well as defect sites and step edges (β_3). The related work function change amounts to $\Delta\Phi = -144$ meV.

H₂O binds more strongly to the rutile(011)-(2x1) films with three resolved monolayer desorption states at 186 K (β_1), 271 K (β_2) and 405 K (β_3) and one multilayer state below 186 K (α) for exposures above 1 L. The interaction of H₂O with rutile(011)-(2x1) differs from that with rutile(110) and (100) mainly by the exis-

tence of the β_3 state at 405 K, which is ascribed to dissociative H₂O adsorption on minority sites, while β_1 and β_2 indicate molecular H₂O adsorption. The β_1 state induces a (1x2) LEED superstructure thereby pointing to long range order within the adsorbed H₂O molecules. The desorption states are reflected as slope changes in the work function change measurements, the total $\Delta\Phi$ amounts to -1 eV for 15 L H₂O exposure.

Whereas the Au clusters on the rutile films ($\theta_{Au} < 1$ ML) hardly influence the adsorptive properties of CO₂ and H₂O, the situation differs markedly for CO: The presence of Au apparently creates new favoured binding sites for CO, which are manifested in an additional broad TPD state γ that shifts from 230 K to 180 K with increasing gold coverage ($\theta_{Au} = 0.1 - 10$ MLE). Unannealed surfaces with low Au content ($\theta_{Au} < 1.5$ MLE ≈ 0.4 ML) exhibit a split γ state at 220 K (γ_1) and 260 K (γ_2) indicating CO species that experience an elevated adsorption energy at or near the gold particles. The respective CO molecules bind either at sites on TiO₂ close to the Au clusters or on the edges of the clusters itself (γ_2). For higher Au coverages, this contribution decreases and the γ_1 intensity increases, which is probably induced by CO adsorption onto the flat terraces of the gold particles. For high coverages ($\theta_{Au} > 5$ MLE ≈ 0.5 ML), the spectra reveal a distinct resemblance to spectra obtained from sputtered Au(110)-(1x2) surfaces. The CO-induced work function change of $\Delta\Phi = -595$ meV for saturation mainly reflects the increased CO uptake of the Au/TiO₂ samples.

The influence of Au especially on the adsorptive properties of CO was explored through a series of systematic gas adsorption studies on carefully prepared and characterized bare and Au-covered rutile films. In contrast to the numerous studies on rutile single crystal surfaces in the current literature, the Au/rutile samples applied in this thesis stand out due to their closer proximity to the practice-oriented polycrystalline and powder catalysts and provide a first step to surmount the materials gap in heterogeneous catalysis.

8 Zusammenfassung

In der vorliegenden Arbeit wurde der Einfluss von Gold auf die Adsorptionseigenschaften von CO, CO₂ und H₂O auf epitaktischen Rutil(011)-(2x1)-Filmen untersucht, die auf einem Rhenium(10 $\bar{1}$ 0)-Einkristall präpariert wurden. Die Rutilfilme weisen einen Stranski-Krastanov-Wachstumsmechanismus auf; nach Abschluss einer vollständigen Titandioxidlage auf der Re(10 $\bar{1}$ 0)-Oberfläche wachsen dreidimensionale Inseln auf der Zwischenlage, die auf der Oberfläche und an zwei Seitenflächen Rutil(011)-(2x1)- und an den anderen beiden Seitenflächen (110)-orientiert sind. Partiiell goldbedeckte Filme wurden durch Gasphasenabscheidung von Au auf die Rutilfilme erzeugt. Au wächst auf Rutil(011)-(2x1) in einem dreidimensionalen Wachstumsmodus auf (Volmer-Weber), das heißt, die Oberfläche wird von Gold nicht benetzt, sondern es bilden sich individuelle Gold-Cluster, die bei höheren Schichtdicken agglomerieren.

TPD-Spektren weisen nach CO-Adsorption auf Rutilfilmen bei 100 K zwei Desorptionszustände unterhalb von 180 K auf (β_1 und β_2), die der molekularen CO-Adsorption an den Titanatomen der Rutil(011)-(2x1) (β_1) und der Rutil(110) (β_2) Facetten zugeschrieben werden und eine Austrittsarbeitsänderung von $\Delta\Phi = -155$ meV verursachen.

Auch CO₂ adsorbiert nur schwach an den Rutilfilmen. Die entsprechenden Desorptionszustände bei 120 K (β_1), 136 K (β_2) und 148 K (β_3) werden auf molekulare CO₂-Adsorption an den Titanatomen der Rutil(011)-(2x1) Facetten (β_1) sowie der (110) Facetten (β_2) und auf die Adsorption an Fehlstellen und Stufen-

plätzen (β_3) zurückgeführt. Die zugehörige Austrittsarbeitsänderung beträgt $\Delta\Phi = -144 \text{ meV}$.

Die Adsorption von Wasser führt zu drei aufgelösten Desorptionszuständen bei 186 K (β_1), 271 K (β_2) und 405 K (β_3), die die Adsorption von Wasser innerhalb der Monolage reflektieren, und einem Multilagenzustand unterhalb von 186 K. Damit unterscheidet sich die Wasseradsorption an Rutil(011)-(2x1) von der Adsorption an Rutil(110) und (100)-Orientierungen hauptsächlich durch den β_3 Zustand bei 405 K, der einer dissoziativen Adsorption von Wasser zugeschrieben wird, während β_1 und β_2 molekularer Adsorption zugeschrieben werden. Der β_1 -Zustand induziert eine (1x2)-LEED-Überstruktur, die auf eine Fernordnung innerhalb der H_2O -Moleküle hindeutet. Die TPD-Zustände äußern sich in den Austrittsarbeitsänderungs-Dosis-Verläufen als Steigungsänderungen; der $\Delta\Phi$ -Sättigungswert bei 100 K beträgt -1 eV für 15 L H_2O .

Während die Adsorptionseigenschaften von CO_2 und H_2O durch die Abscheidung von Gold ($\theta_{\text{Au}} < 1 \text{ ML}$) auf den Rutilfilmen kaum beeinflusst werden, ist die Situation bei CO anders:

Hier werden durch die Gegenwart von Gold offenbar neue günstige Bindungsplätze geschaffen, die sich in den CO-TPD-Spektren durch einen breiten zusätzlichen Desorptionszustand γ äußern, der sich mit zunehmenden Goldbedeckungen von 230 K zu 180 K verschiebt ($\theta_{\text{Au}} = 0.1 - 10 \text{ MLE}$). Ungetemperte Oberflächen mit niedrigem Au-Gehalt ($\theta_{\text{Au}} < 1.5 \text{ MLE} \approx 0.4 \text{ ML}$) weisen einen zweigeteilten γ Zustand bei 220 (γ_1) und 260 K (γ_2) auf, der auf unterschiedlich gebundene CO-Spezies an Goldpartikeln zurückgeführt wird. Die entsprechenden CO Moleküle adsorbieren entweder an TiO_2 -Adsorptionsplätzen nahe den Au-Clustern oder aber auf Randplätzen auf den Au-Clustern (γ_2). Für höhere Au-Bedeckungen nimmt dieser Beitrag ab und die γ_1 Intensität nimmt zu, die vermutlich auf die CO-Adsorption auf den Terrassen der Au-Cluster zurückzuführen ist. Bei hohen Goldbedeckungen ($\theta_{\text{Au}} > 5 \text{ MLE} \approx 0.5 \text{ ML}$) nähert sich der γ Zustand

der Bindungssituation an, wie sie für die CO-Adsorption an gesputterten Goldoberflächen beobachtet wurde. Die CO-induzierte Austrittsarbeitsänderung von $\Delta\Phi = -595 \text{ meV}$ bei Sättigung reflektiert die zunehmende CO-Aufnahme der goldbedeckten Filme.

Durch eine Reihe von systematischen Gas-Adsorptionsmessungen an sorgfältig präparierten und charakterisierten reinen und partiell goldbedeckten Rutilfilmen ist es gelungen, einen Einfluss präadsorbierter Gold-Teilchen auf die Bindungseigenschaften insbesondere von CO herauszuarbeiten. Gegenüber den vielen in der Literatur publizierten Resultaten, die an kompakten Rutil-Einkristallobersflächen erhalten wurden, zeichnen sich die in dieser Arbeit verwendeten Proben, die aus dünnen epitaktischen Rutilfilmen bestanden, durch eine größere Nähe zu den praxisrelevanten polykristallinen und Pulverkatalysatoren aus und bieten demzufolge einen ersten Schritt hin zur Überwindung der im Eingangsteil dieser Arbeit konstatierten Materiallücke.



Bibliography

- [1] N. N. GREENWOOD and A. EARNSHAW, *Chemie der Elemente*, VCH, Weinheim, 1 edition, 1990.
- [2] A. LINSEBIGLER, G. LU, and J. T. YATES JR., *Chem. Rev.* **95**, 735 (1995).
- [3] A. GOETZBERGER, B. VOSS, and J. KNOBLOCH, *Sonnenenergie, Photovoltaik*, Teubner Studienbücher Physik, Stuttgart, 2 edition, 1997.
- [4] M. HARUTA, S. TSUBOTA, T. KOBAYASHI, H. KAGEYAMA, M. GENET, and B. DELMON, *J. Catal.* **144**, 175 (1993).
- [5] B. HAMMER and J. K. NORSKOV, *Nature* **376**, 238 (1995).
- [6] Z. LIU and M. VANNICE, *Catal. Lett.* **43**, 51 (1997).
- [7] C. LEMIRE, R. MEYER, S. K. SHAIKHUTDINOV, and H. J. FREUND, *Surf. Sci.* **552**, 27 (2004).
- [8] T. V. W. JANSSENS, A. CARLSSON, A. PUIG-MOLINA, and B. S. CLAUSEN, *J. Catal.* **240**, 108 (2006).
- [9] D. L. SMITH, *Thin-Film Deposition – Principles & Practice*, 1995.
- [10] T. V. ASHWORTH and G. THORNTON, *Thin Solid Films* **400**, 43 (2001).

- [11] N. McCAVISH and R. BENNETT, *Surf. Sci.* **546**, 47 (2003).
- [12] A. B. BOFFA, H. C. GALLOWAY, P. W. JACOBS, J. J. BENTEZ, J. D. BATTEAS, M. SALMERON, A. T. BELL, and G. A. SOMORJAI, *Surf. Sci.* **326**, 80 (1995).
- [13] X. LAI, Q. GUO, B. K. MIN, and D. W. GOODMAN, *Surf. Sci.* **487**, 1 (2001).
- [14] Z. ZHAO, T. DIEMANT, D. ROSENTHAL, K. CHRISTMANN, J. BANS-MANN, H. RAUSCHER, and R. J. BEHM, *Surf. Sci.* **600**, 4992 (2006).
- [15] S. SCHUBERT, *Wachstum von Rutil(110) auf Re(0001) und Adsorption von Gold auf Rutil(011)-(2x1)/Re(10 $\bar{1}$ 0)*, PhD thesis, Freie Universität Berlin, 2009 - to be published.
- [16] D. ROSENTHAL, I. ZIZAK, N. DAROWSKI, T. T. MAGKOEV, and K. CHRISTMANN, *Surf. Sci.* **600**, 2830 (2006).
- [17] D. ROSENTHAL, *Wachstum und Struktur von Titandioxid auf den Übergangsmetalloberflächen Re(10 $\bar{1}$ 0) und Ru(0001)*, PhD thesis, Freie Universität Berlin, 2007.
- [18] W. KUDERNATSCH, Wachstum und chemische Charakterisierung von epitaktischen Titanoxidfilmen auf einer Rhenium(10 $\bar{1}$ 0)-Oberfläche, Master's thesis, Freie Universität Berlin, 2005.
- [19] X.-Q. GONG, N. KHORSHIDI, A. STIERLE, V. VONK, C. ELLINGER, H. DOSCH, H. CHENG, A. SELLONI, Y. HE, O. DULUB, and U. DIEBOLD, *Surf. Sci.* **603**, 138 (2009).
- [20] X. TORRELLES, G. CABAILH, R. LINDSAY, O. BIKONDOA, J. ROY, J. ZEGENHAGEN, G. TEOBALDI, W. A. HOFER, and G. THORNTON, *Phys. Rev. Lett.* **101**, 185501/1 (2008).

- [21] Z. DOHNÁLEK, J. KIM, O. BONDARCHUK, J. M. WHITE, and B. D. KAY, *J. Phys. Chem. B* **110**, 6229 (2006).
- [22] A. LINSEBIGLER, G. LU, and J. T. YATES JR., *J. Chem. Phys.* **21**, 9438 (1995).
- [23] M. B. HUGENSCHMIDT, L. GAMBLE, and C. T. CAMPBELL, *Surf. Sci.* **302**, 329 (1994).
- [24] R. T. ZEHR and M. A. HENDERSON, *Surf. Sci.* **602**, 1507 (2008).
- [25] M. A. HENDERSON, *Langmuir* **12**, 5093 (1996).
- [26] M. A. HENDERSON, *Surf. Sci.* **400**, 203 (1998).
- [27] C. DI VALENTIN, A. TILOCCA, A. SELLONI, T. J. BECK, A. KLUST, M. BATZILL, Y. LOSOVYJ, and U. DIEBOLD, *J. Am. Chem. Soc.* **127**, 9895 (2005).
- [28] T. BECK, A. KLUST, M. BATZILL, U. DIEBOLD, C. D. VALENTIN, A. TILOCCA, and A. SELLONI, *Surf. Sci.* **591**, L267 (2005).
- [29] K. CHRISTMANN, *Introduction to Surface Physical Chemistry*, Steinkopf, Darmstadt, 1991.
- [30] R. MEYER, C. LEMIRE, S. K. SHAIKHUTDINOV, and H.-J. FREUND, *Gold Bull.* **37**, 72 (2004).
- [31] J.-D. GRUNWALDT, C. KIENER, C. WÖGERBAUER, and A. BAIKER, *J. Catal.* **181**, 223 (1999).
- [32] J.-D. GRUNWALDT, M. MACIEJEWSKI, O. S. BECKER, P. FABRIZIOLI, and A. BAIKER, *J. Catal.* **186**, 458 (1999).
- [33] M. MAVRIKAKIS, P. STOLTZE, and J. K. NORSKOV, *Catal. Lett.* **64**, 101 (2000).

BIBLIOGRAPHY

- [34] S. R. BAHN, N. LOPEZ, J. K. NORSKOV, and K. W. JACOBSEN, *Phys. Rev. B* **66**, 081405 (2002).
- [35] L. M. MOLINA and B. HAMMER, *Phys. Rev. Lett.* **90**, 206102 (2003).
- [36] E. BAUER, *Zeitschrift für Kristallographie* **110**, 372 (1958).
- [37] C. ARGILE and G. E. RHEAD, *Surf. Sci. Rep.* **10**, 277 (1989).
- [38] J. A. VENABLES, *Surf. Sci.* **299/300**, 798 (1994).
- [39] G. EHRLICH and F. HUDDA, *J. Chem. Phys.* **44**, 1039 (1966).
- [40] D. SCHWOEBEL and E. J. E. J. SIPSEY, *J. Appl. Phys.* **37**, 3682 (1966).
- [41] A. F. HOLLEMAN and E. WIBERG, *Lehrbuch der Anorganischen Chemie*, Walter de Gruyter, Berlin, New York, 100 edition, 1985.
- [42] E. RIEDEL, *Anorganische Chemie*, Walter de Gruyter, 4 edition, 1999.
- [43] L.-G. LIU, T. TAKAHASHI, and W. A. BASSETT, *J. Phys. Chem. Solids* **31**, 1345 (1970).
- [44] H. L. DAVIS and D. M. ZEHNER, *J. Vac. Sci. Technol.* **17**, 190 (1980).
- [45] R. DÖLL, L. HAMMER, K. HEINZ, K. BEDÜRFTIG, U. MUSCHIOL, K. CHRISTMANN, A. P. SEITSONEN, H. BLUDAU, and H. OVER, *J. Chem. Phys.* **108**, 8671 (1998).
- [46] F. A. GRANT, *Rev. Mod. Phys.* **31**, 646 (1959).
- [47] M. RAMAMOORTHY, D. VANDERBILT, and R. D. KING-SMITH, *Phys. Rev. B* **49**, 16721 (1994).
- [48] C. JANIAK, T. KLAPÖTKE, and H.-J. MEYER, *Moderne Anorganische Chemie*, Walter de Gruyter, 2003.

- [49] U. MÜLLER, *Anorganische Strukturchemie*, Teubner, Stuttgart, 3 edition, 1996.
- [50] L. E. FIRMENT, *Surf. Sci.* **116**, 205 (1982).
- [51] T. BECK, A. KLUST, M. BATZILL, U. DIEBOLD, L. DI VALENTIN, and A. SELLONI, *Phys. Rev. Lett.* **93**, 036104 (2004).
- [52] T. KUBO, H. ORITA, and H. NOZOYE, *J. Am. Chem. Soc.* **129**, 10474 (2007).
- [53] N. KHORSHIDI, C. ELLINGER, V. VONK, A. STIERLE, and H. DOSCH, Structure of the rutile TiO₂-(011) surface, in *ECOSS 25*, 2008.
- [54] N. KHORSHIDI, A. STIERLE, V. VONK, and C. ELLINGER, Structure of the rutile TiO₂(011)-(2x1) surface, in *DPG*, 2008.
- [55] D. R. LIDE, editor, *CRC Handbook of Chemistry and Physics, Internet Version 2005*, < <http://www.hbcpnetbase.com> >, 2005.
- [56] FLUCK and HEUMANN, *Periodensystem der Elemente*, Wiley-VCH Verlag GmbH, 3 edition, 2002.
- [57] M. WINTER, *WebElements* [<http://www.webelements.com/>], 2009.
- [58] <http://au-gold.info/energy.html>, 2009.
- [59] W. WEISS, M. RITTER, D. ZSCHERPEL, M. SWOBODA, and R. SCHLÖGL, *J. Vac. Sci. Technol. A* **16**, 21 (1998).
- [60] G. ERTL and J. KÜPPERS, *Low Energy Electrons and Surface Chemistry*, Weinheim, VCH, 2 edition, 1985.
- [61] F. BESENBACHER, J. V. LAURITSEN, and S. WENDT, *Nano Today* **2**, 30 (2007).

- [62] S. SCHWEDE, Rastertunnelmikroskopische Untersuchungen von Titandioxidfilmen auf einer sauerstoffbedeckten Rhenium($10\bar{1}0$)-Oberfläche, Master's thesis, Freie Universität Berlin, 2008.
- [63] D. BRIGGS and M. P. SEAH, *Practical Surface Analysis by Auger and X-ray Photoelectron Spectroscopy*, John Wiley & Sons, Chichester, New York, Brisbane, Toronto, Singapore, 1983.
- [64] C. J. POWELL and A. JABLONSKI, *NIST Electron Inelastic-Mean-Free-Path Database (Version 1.1)*, National Institute of Standards and Technology, 2000.
- [65] *Monograph 175, ITS-90*, National Institute of Standards and Technology (NIST).
- [66] L. DAVIS, N. MACDONALD, P. PALMBERG, G. RIACH, and R. WEBER, *Handbook of Auger Electron Spectroscopy*, Physical Electronics Industries, 1976.
- [67] P. REDHEAD, *Vacuum* **12**, 203 (1962).
- [68] A. M. DE JONG and J. W. NIEMANTSVERDRIET, *Surf. Sci.* **233**, 355 (1990).
- [69] D. R. SANDSTROM and S. P. WITHROW, *J. Vac. Sci. Technol.* **14**, 748 (1977).
- [70] J. LENZ, P. RECH, K. CHRISTMANN, M. NEUBER, C. ZUBRÄGEL, and E. SCHWARZ, *Surf. Sci.* **260/270**, 410 (1992).
- [71] J. LENZ, *Die geometrischen und elektronischen Strukturen der Adsorbatphasen von Sauerstoff auf der Rhenium($10\bar{1}0$)-Oberfläche*, PhD thesis, Freie Universität Berlin, 1994.

- [72] V. R. DHANAK, K. C. PRINCE, R. ROSEI, P. W. MURRAY, F. M. LEIBSLE, M. BOWKER, and G. THORNTON, *Phys. Rev. B* **49**, 5585 (1994).
- [73] B. HOLLAND and D. WOODRUFF, *Surf. Sci.* **36**, 488 (1973).
- [74] R. LAMBERT, *Surf. Sci.* **49**, 325 (1975).
- [75] K. SCHMIDT, Master's thesis, Freie Universität Berlin, 1992.
- [76] D. W. GOODMAN, *J. Catal.* **216**, 213 (2003), 40th Anniversary Commemorative Issue.
- [77] S. WENDT, R. SCHAUB, J. MATTHIESEN, E. VESTERGAARD, E. WAHLSTRÖM, M. RASMUSSEN, P. THOSTRUP, L. MOLINA, E. LÆGSGAARD, I. STENSGAARD, B. HAMMER, and F. BESENBACHER, *Surf. Sci.* **598**, 226 (2005).
- [78] O. DULUB, M. BATZILL, S. SOLOVEV, E. LOGINOVA, A. ALCHAGIROV, T. E. MADEY, and U. DIEBOLD, *Science* **317**, 1052 (2007).
- [79] M. BÄUMER, D. CAPPUS, H. KUHLENBECK, H.-J. FREUND, G. WILHELM, A. BRODDE, and H. NEDDERMEYE, *Surf. Sci.* **253**, 116 (1991).
- [80] D. CAPPUS, J. KLINKMANN, H. KUHLENBECK, and H. J. FREUND, *Surf. Sci.* **325**, L421 (1995).
- [81] C. PAULS, D. PRZYREMBEL, and K. CHRISTMANN, *J. Phys. Chem. B* **108**, 14749 (2004).
- [82] D. C. SORESCU and J. T. YATES, *J. Phys. Chem. B* **102**, 4556 (1998).
- [83] J. C. TRACY and P. W. PALMBERG, *J. Chem. Phys.* **51**, 4852 (1969).
- [84] M. HENZLER and W. GÖPEL, *Oberflächenphysik des Festkörpers*, Teubner, 1994.

- [85] W. GÖPEL, G. ROCKER, and R. FEIERABEND, *Phys. Rev. B* **28**, 3427 (1983).
- [86] C. MURYN, P. HARDMAN, J. CROUCH, G. RAIKER, G. THORNTON, and D. LAW, *Surf. Sci.* **251-252**, 747 (1991).
- [87] S. WENDT, J. MATTHIESEN, R. SCHAUB, E. K. VESTERGAARD, E. LAEGSGAARD, F. BESENBACHER, and B. HAMMER, *Phys. Rev. Lett.* **96**, 066107 (2006).
- [88] M. A. HENDERSON, *Surf. Sci.* **319**, 315 (1994).
- [89] H. J. FREUND and M. W. ROBERTS, *Surf. Sci. Rep.* **25**, 225 (1996).
- [90] T. L. THOMPSON, O. DIWALD, and J. T. YATES, *J. Phys. Chem. B* **107**, 11700 (2003).
- [91] S. FUNK, B. HOKKANEN, E. JOHNSON, and U. BURGHAUS, *Chem. Phys. Lett.* **422**, 461 (2006).
- [92] J. WANG, B. HOKKANEN, and U. BURGHAUS, *Surf. Sci.* **577**, 158 (2005).
- [93] M. A. HENDERSON, W. S. EPLING, C. L. PERKINS, C. H. F. PEDEN, and U. DIEBOLD, *J. Phys. Chem. B* **103**, 5328 (1999).
- [94] M. C. SAINT-LAGER, A. BAILLY, M. MANTILLA, S. GARAUDEE, R. LAZZARI, P. DOLLE, O. ROBACH, J. JUPILLE, I. LAOUFI, and P. TAUNIER, *Gold Bull.* **41**, 159 (2008).
- [95] Y. MAEDA, T. FUJITANI, S. TSUBOTA, and M. HARUTA, *Surf. Sci.* **562**, 1 (2004).
- [96] J. M. GOTTFRIED, *CO Oxidation over Gold – Adsorption and Reaction of Oxygen, Carbon Monoxide, and Carbon Dioxide on an Au(110)-(1x2) Surface*, PhD thesis, Freie Universität Berlin, 2003.

- [97] J. M. GOTTFRIED, K. J. SCHMIDT, S. L. M. SCHROEDER, and K. CHRISTMANN, *Surf. Sci.* **536**, 206 (2003).
- [98] S. K. SHAIKHUTDINOV, R. MEYER, M. NASCHITZKI, M. BAUMER, and H. J. FREUND, *Catal. Lett.* **86**, 211 (2003).
- [99] C. WINKLER, A. J. CAREW, S. HAQ, and R. RAVAL, *Langmuir* **19**, 717 (2003).
- [100] C. RUGGIERO and P. HOLLINS, *Surf. Sci.* **377-379**, 583 (1997), European Conference on Surface Science.
- [101] D. MATTHEY, J. G. WANG, S. WENDT, J. MATTHIESEN, R. SCHAUB, E. LAEGSGAARD, B. HAMMER, and F. BESENBACHER, *Science* **315**, 1692 (2007).
- [102] C. RUGGIERO and P. HOLLINS, *J. Chem. Soc. Faraday Trans.* **92**, 4829 (1996).
- [103] G. MCELHINEY and J. PRITCHARD, *Surf. Sci.* **60**, 397 (1976).
- [104] D. A. OUTKA and R. J. MADIX, *J. Am. Chem. Soc.* **109**, 1708 (1987).
- [105] M. CHEN, K. LUO, D. KUMAR, W. WALLACE, C.-W. YI, K. GATH, and D. GOODMAN, *Surf. Sci.* **601**, 632 (2007).

BIBLIOGRAPHY

List of Figures

2.1	Possible reaction pathways for the low-temperature CO oxidation over Au / TiO ₂ catalysts. Taken from [30].	7
2.2	The three basic growth mechanisms for thin films deposited from the gas phase [36].	12
2.3	Schematic diagram of processes and characteristic energies in nucleation and growth on surfaces. Taken from reference [38].	13
2.4	a) The rhenium lattice with its primitive unit cell; b) The Re(10 $\bar{1}$ 0) surface.	16
2.5	The tetragonal unit cell of rutile; red spheres: oxygen atoms, green spheres: titanium atoms.	18
2.6	The three most stable rutile surfaces.	18
2.7	Equilibrium shape of a macroscopic rutile crystal [47].	19
2.8	Rutile TiO ₂ (110); red spheres: oxygen atoms, green spheres: titanium atoms.	19
2.9	Model of the unrelaxed rutile(100) surface; red spheres: oxygen atoms, green spheres: titanium atoms.	20
2.10	Rutile TiO ₂ (011)-(1x1); the dotted line marks the glide mirror plane; red spheres: oxygen atoms, green spheres: titanium atoms.	21

LIST OF FIGURES

2.11	Ball and stick models of the rutile $\text{TiO}_2(011)-(2 \times 1)$ surface; blue spheres: oxygen atoms, red spheres: titanium atoms; a) 'titanyl' model from Beck <i>et al.</i> [51], b) 'microfaceting' model from Kubo <i>et al.</i> [52], c) new 'brookite(001)-like' model [19, 20], d) unreconstructed rutile(011) surface. Taken from reference [20].	22
3.1	The ultra-high vacuum recipient used in the present thesis.	28
3.2	Image of the off-axis sample holder at the end of the manipulator.	29
3.3	Picture of the inner parts of the gold evaporator that was used in the present thesis.	31
3.4	The five surface Bravais lattices: a) square, $a_1 = a_2$, $\alpha = 90^\circ$; b) primitive rectangular, $a_1 \neq a_2$, $\alpha = 90^\circ$; c) centered rectangular, $a_1 \neq a_2$, $\alpha = 90^\circ$; d) hexagonal, $a_1 = a_2$, $\alpha = 60^\circ$; e) oblique, $a_1 \neq a_2$, $\alpha \neq 90^\circ$ [60].	33
3.5	Examples for adsorbate superstructures; a) (2×2) , b) $c(2 \times 2)$ and $(\sqrt{2} \times \sqrt{2})R 45^\circ$, respectively; black circles: substrate atoms, red circles: adsorbate atoms/molecules.	34
3.6	Scattering of electrons on a one-dimensional chain of atoms.	34
3.7	Scheme of the relationship between LEED pattern and K space.	37
3.8	Schematics illustrating the basic operational principle and the primary components of an STM. Taken from reference [61].	39
3.9	Comparison of the thermoelectric voltage (upper plots) and the Seebeck-coefficient (lower plots) of type K and type C thermocouples [65, 69].	46
3.10	Comparison between the heating rate when the thermoelectric voltage U_{th} (a) and the temperature T (b) is controlled, respectively.	48
4.1	LEED pattern (55 eV) and STM picture ($I = 0.1$ nA, $U = 0.021$ V) of the clean rhenium($10\bar{1}0$) surface.	54

4.2	LEED pattern (electron energy = 55 eV) and STM images ($I = 0.3 \text{ nA}$, $U = 0.5 \text{ V}$) of the $(1 \times 3)2\text{O}$ superstructure on $\text{Re}(10\bar{1}0)$	55
4.3	Schemes of the three proposed surface models for the (1×3) oxygen superstructure on $\text{Re}(10\bar{1}0)$ taken from Jörg Lenz' PhD Thesis [71]; grey and white circles = rhenium atoms, black circles = oxygen atoms.	56
4.4	Auger electron-spectra of the bare rhenium($10\bar{1}0$) surface, the (1×3) oxygen phase and a 24 MLE thick rutile(011)-(2x1) film. The observed Auger signals can be assigned to rhenium (33, 168, 176 eV), oxygen (488, 510 eV) and titanium (386, 417 eV).	59
4.5	Development of the Auger intensities of the Re (33 eV) and the oxygen (510 eV) signal with increasing titania deposition time. Both plots exhibit breaks after a deposition time of $\approx 75 \text{ s}$	60
4.6	LEED patterns of the clean $\text{Re}(10\bar{1}0)$ surface, the $(1 \times 3)2\text{O}$ superstructure and the epitaxially grown TiO_2 film (thickness $\approx 24 \text{ MLE}$) taken at 40 eV.	62
4.7	STM images of a 'thin' (a,b, $I = 0.3 \text{ nA}$, $U = 1 \text{ V}$) and a 'thicker' (c,d, $I = 2 \text{ nA}$, $U = 2 \text{ V}$) rutile $\text{TiO}_2(011)-(2 \times 1)$ film; a,b: thickness $\approx 12 \text{ MLE}$; c,d: thickness $\approx 24 \text{ MLE}$	64
4.8	Auger electron-spectra of a bare rutile(011)-(2x1) film (thickness $\approx 24 \text{ MLE}$) and a partially gold-covered film (Au deposition time = 1200 s $\approx 10 \text{ MLE}$).	66
4.9	Scheme of the preparation procedure for the Au/rutile(011)-(2x1)/ $\text{Re}(10\bar{1}0)$ model catalysts that were prepared and studied in the present thesis.	67
5.1	Series of CO TPD spectra from a rutile $\text{TiO}_2(011)-(2 \times 1)$ film with increasing CO exposure, film thickness $\approx 24 \text{ MLE}$; $T_{ad} = 100 \text{ K}$	73

LIST OF FIGURES

5.2	CO TPD series on a 12 MLE rutile(011)-(2x1) film with increasing CO doses. The β_1 intensity decreases with increasing CO exposure. Furthermore, it appears prior to the saturation of the β_2 state. . .	78
5.3	a) Series of CO TPD spectra from a rutile TiO ₂ (011)-(2x1) film with increasing CO exposure, film thickness \approx 12 MLE; $T_{ad} = 100$ K. b) Comparison of the coverages plotted over the initial CO exposure for a thin (12 MLE) and a thick (24 MLE) rutile film. . .	80
5.4	Influence of the heating temperature on the CO TPD spectra. . .	82
5.5	Check for the reversibility of the changes, which occur to the TPD spectra after heating. For the depicted spectra, the sample was heated to 400 K once. The subsequent spectra were taken to a maximum temperature of 260 K. The CO exposure was always 0.5 L ($T_{ad} = 100$ K).	83
5.6	CO TPD spectra from a TiO ₂ (011)-(2x1) film; T_{limit} was increased stepwise; CO-exposure: 0 L (only from the residual gas); $\beta = 4.3$ K/s.	85
5.7	CO TPD spectra from H ₂ O / rutile(011)-(2x1); $\beta = 4.3$ K/s. . . .	87
5.8	Work function change induced by adsorption of CO on rutile (011)-(2x1).	88
5.9	Series of H ₂ O TPD spectra from a 24 MLE thick rutile film with increasing H ₂ O exposure; heating rate $\beta = 4.3$ K/s; $T_{ad} = 95$ K. . .	94
5.10	Plot of the TPD H ₂ O yield against the initial H ₂ O exposure; $\beta = 4.3$ K/s; $T_{ad} = 95$ K; triangles: exposure determined from the pressure meter reading, squares: exposure determined from the pressure versus time plot during exposure.	95
5.11	Series of H ₂ O TPD spectra from a 24 MLE thick rutile(011)-(2x1) film with CO exposures of 0.01 to 0.11 L; the arrow marks the weak desorption shoulder at around 340 K; the spectra have been smoothed via adjacent averaging; $\beta = 4.3$ K/s; $T_{ad} = 95$ K.	95

5.12	Series of H ₂ O TPD spectra on a 36 MLE thick rutile film that was prepared and studied in another recipient (the TPD intensities differ systematically from the other spectra). The spectra were smoothed via adjacent averaging prior to plotting. The temperature measurement is not as reliable as in the other spectra. $\beta = 4.4$ K/s; $T_{ad} = 127$ K.	97
5.13	LEED patterns of a 24 MLE thick rutile(011)-(2x1) film; electron beam energy = 35 eV; a) pure rutile film at 174 K; b) (1x2) superstructure on rutile, $p(\text{H}_2\text{O}) = 1 \times 10^{-8}$ mbar, $T = 190$ K; the rectangular boxes mark the region of the patterns that was taken for figure 5.14 ($h = -1, k = (-2) - (+2)$).	102
5.14	(1x2)H ₂ O superstructure on rutile TiO ₂ (011)-(2x1) at different temperatures; a) only residual gas, b) – f) $p(\text{H}_2\text{O}) = 1 \times 10^{-8}$ mbar, g) $p(\text{H}_2\text{O}) = 3 \times 10^{-9}$ mbar; h) spot designation; electron beam energy = 35 eV.	102
5.15	Work function change induced by H ₂ O adsorption on rutile(011)-(2x1) (overview).	105
5.16	Work function change induced by H ₂ O adsorption on rutile (011)-(2x1) plotted against the H ₂ O exposure, film thickness ≈ 24 MLE, $T_{ad} = 100$ K.	106
5.17	Series of CO ₂ TPD spectra from a 24 MLE thick rutile(011)-(2x1) film with increasing CO ₂ exposures; $T_{ad} = 100$ K; $T_{limit} = 410$ K.	113
5.18	Series of CO ₂ TPD spectra from a 24 MLE thick rutile(011)-(2x1) film with increasing exposures; $T_{ad} = 95$ K; $T_{limit} = 290$ K.	114
5.19	CO ₂ -induced work function change on a 24 MLE thick rutile(011)-(2x1) film. $T_{ad} = 100$ K.	117

6.1	CO TPD spectra taken from Au/rutile(011)-(2x1)/Re(10 $\bar{1}$ 0) model catalysts covered with different amounts of gold. The amount of deposited gold is expressed in terms of the gold deposition time. Rutile film thickness \approx 24 MLE, $T_{ad} = 100$ K, $T_{limit} = 400$ K, $\beta = 4.3$ K/s.	123
6.2	Progression of the peak maximum of the γ state plotted versus the Au deposition time (with the respective Redhead desorption energies in brackets, $\nu = 10^{13} s^{-1}$).	124
6.3	Residual CO coverage at 100, 200 and 250 K (from bottom to top) plotted versus the Au deposition time for 0.5 L spectra.	125
6.4	Comparison of the first “virgin” and the second “pre-annealed” spectra of the TPD series for rutile films covered with different amounts of gold (deposition times of 15, 30, 60 and 180 s). The “virgin” spectra were recorded directly after the Au deposition at 300 K and subsequent cooling to 100 K, the “pre-annealed” spectra were obtained after the “virgin” ones. The spectra that were recorded subsequent to the “pre-annealed” spectra did not exhibit further changes.	127
6.5	CO-induced work function change ($\Delta\Phi$) on a 24 MLE thick rutile(011)-(2x1) film covered with 1200 s Au; $T_{ad} = 100$ K.	131
6.6	Water (top) and CO (bottom) TPD spectra after CO adsorption onto a water pre-covered Au/TiO ₂ /Re model catalyst at 100 K. $\beta = 4.33$ K / s.	134
6.7	Plot of the CO ₂ yields obtained from a 24 MLE thick bare rutile(011)-(2x1) film (squares) and a Au covered model catalyst.	135
6.8	CO ₂ TPD series obtained from a gold covered Au/rutile(011)-(2x1)/Re(10 $\bar{1}$ 0) model catalyst. $T_{ad} = 100$ K.	136

.1 CO TPD spectra for various initial CO coverages (0, 0.18, 0.31, 0.50, 0.75, 0.84, 1.06, 1.50, 1.63) on TiO₂(110). CO was adsorbed at 32 K, and the sample was heated linearly at a rate of 1 K/s. The circles are placed on the 1.5 ML (dashed) curve at temperatures where 1 ML (open circle) and 0.5 ML (gray circle) remain. Figure taken from reference [21]. 167

.2 STM images of high amounts of Au deposited onto an epitaxial rutile(011)-(2x1) film. The clusters are hemispherically shaped with an average diameter of 70 Å and a height of 30 Å. The images were taken by S. Schwede. 168

LIST OF FIGURES

List of Tables

2.1	Physical properties of rhenium, titanium and gold; o = octahedral, sp = square-planar. Data taken from [42, 56, 41, 57, 58].	25
5.1	Influence of the limiting temperature T_{limit} on the CO TPD states on epitactic rutile(011) films; film thickness ≈ 24 MLE; adsorption temperature $T_{ad} = 100$ K; heating rate $\beta = 4.3$ K/s; $\nu = 10^{13} s^{-1}$. . .	84
5.2	Summary of the CO interaction with epitaxial rutile (011)-(2x1) films grown on a Re(10 $\bar{1}$ 0) single crystal surface. $\nu = 10^{13} s^{-1}$. . .	92
5.3	Work function change induced by the adsorption of water on a 24 MLE thick rutile(011)-(2x1) film at 100 K.	107
5.4	Summary of the H ₂ O desorption states from a 24 MLE thick rutile(011)-(2x1) film; RH = Redhead, $\nu = 10^{13} s^{-1}$	111
5.5	Summary of the CO ₂ interaction with epitaxial rutile (011)-(2x1) films grown on a Re(10 $\bar{1}$ 0) single crystal surface. $\nu = 10^{13} s^{-1}$. . .	120

LIST OF TABLES

A Additional information

Regarding section 5.1 – CO / rutile(011)-(2x1):

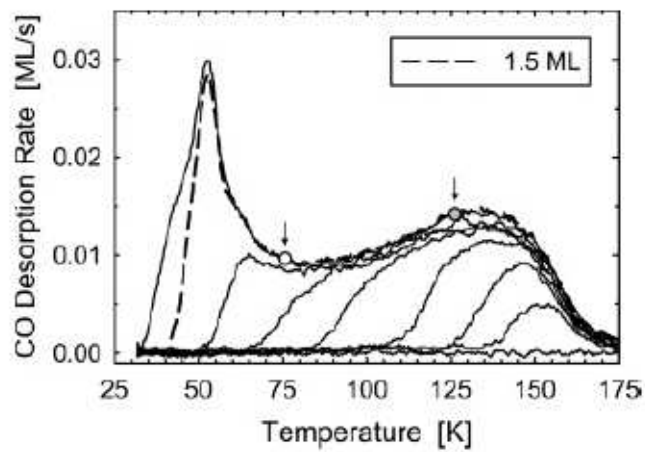
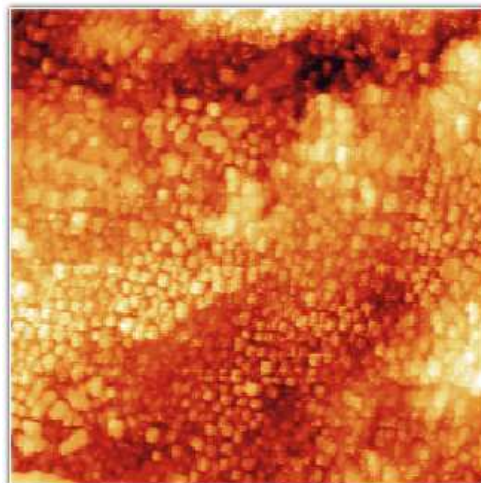
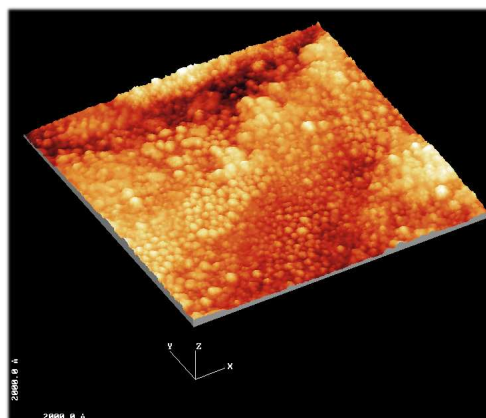


Figure .1: CO TPD spectra for various initial CO coverages (0, 0.18, 0.31, 0.50, 0.75, 0.84, 1.06, 1.50, 1.63) on $\text{TiO}_2(110)$. CO was adsorbed at 32 K, and the sample was heated linearly at a rate of 1 K/s. The circles are placed on the 1.5 ML (dashed) curve at temperatures where 1 ML (open circle) and 0.5 ML (gray circle) remain. Figure taken from reference [21].

Regarding section 4.4 – Preparation of partially Au-covered
rutile $\text{TiO}_2(011)-(2 \times 1)$ films



(a) $2000 \times 2000 \text{ \AA}$, top view



(b) $2000 \times 2000 \text{ \AA}$, contour plot

Figure .2: STM images of high amounts of Au deposited onto an epitaxial rutile(011)-(2x1) film. The clusters are hemispherically shaped with an average diameter of 70 \AA and a height of 30 \AA . The images were taken by S. Schwede.

B Acknowledgment – Danksagung

Ich danke Prof. Dr. K. Christmann für die Betreuung dieser Arbeit und die interessante und herausfordernde Themenstellung.

Prof. Dr. Eugen Illenberger danke ich für die Übernahme der Zweitbegutachtung.

Für finanzielle Unterstützung während der Erstellung der Dissertation im Rahmen eines Promotionsstipendiums danke ich der Studienstiftung des deutschen Volkes, ohne die der flexible Ablauf dieser Arbeit nicht möglich gewesen wäre.

Mein Dank für die Unterstützung in technischen Dingen geht an Rudolf Cames, Erwin Biller, Manfred Swoboda sowie an Peter Schwartze und die mechanische Werkstatt unter Horst Binkowski.

Ich danke den Mitgliedern der Arbeitsgruppen von Prof. Christmann und Prof. Illenberger für die angenehme Gesellschaft.

Mein größter Dank gilt Ilko und Elena.



C Curriculum Vitae



D Publications

In preparation

- *Interaction of H₂O with epitaxial rutile (011)-(2x1) films studied by TPD, LEED and $\Delta\Phi$*
W. Kudernatsch, S. Schubert and K. Christmann.
- *Gold single crystal surfaces and Au nanoparticles dispersed on titania surfaces as catalysts for the CO oxidation reaction*
W. Kudernatsch, S. Roth, S. Schwede, J.M. Gottfried and K. Christmann.

Conference and seminar contributions

1. *STM study of the structure and morphology of TiO₂ thin films epitaxially grown on Re(10 $\bar{1}$ 0)*
S. Schwede, S. Schubert, W. Kudernatsch and K. Christmann.
Verhandlungen der DPG, Dresden, March 2009.
2. *Interaction of CO, CO₂ and H₂O with Au/rutile TiO₂(011)-(2x1)/Re(10 $\bar{1}$ 0) model catalysts*
W. Kudernatsch and K. Christmann.
Seminar (Prof. Besenbacher), Århus, November 2008.
3. *Influence of Au on the adsorption behavior of CO, CO₂ and H₂O on epitaxial rutile films*
W. Kudernatsch, S. Schubert, S. Schwede and K. Christmann.
25th European Conference on Surface Science, Liverpool, August 2008.

-
4. *Rutilfilme auf Rhenium (0001) und Rhenium(10 $\bar{1}$ 0) Oberflächen: Wachstum, Struktur und chemische Eigenschaften*
S. Schubert, W. Kudernatsch and K. Christmann.
Tag der Chemie, Freie Universität Berlin, May 2008.
 5. *Interaction of CO, CO₂, O₂ and H₂O with Au/ Rutile TiO₂(011)-(2x1)/ Re(10 $\bar{1}$ 0) model catalysts*
W. Kudernatsch, K. Dumbuya, J. M. Gottfried, H.-P. Steinrück and K. Christmann.
Verhandlungen der DPG, Berlin, February 2008.
 6. *Adsorption of Au on Rutile TiO₂(011)-(2x1) and (110) films grown on Rhenium Host Surfaces*
S. Schubert, W. Kudernatsch, D. Rosenthal and K. Christmann
Verhandlungen der DPG, Regensburg, March 2007.
 7. *Growth of titania films on rhenium*
W. Kudernatsch
Seminar PCII (Prof. Steinrück), Erlangen, February 2007.
 8. *Tieftemperatur CO-Oxidation über Au/TiO₂ Modellkatalysatoren*
W. Kudernatsch
Doktorandenforum Natur+Wissenschaft der Studienstiftung des deutschen Volkes, Cologne, November 2006.
 9. *Growth, Structure and Chemical Properties of Epitaxial Titania Films on Rhenium Surfaces*
W. Kudernatsch, S. Roth, D. Rosenthal and K. Christmann.
24th European Conference on Surface Science, Paris, September 2006.
 10. *Growth, Structure and Chemical Properties of Epitaxial Titania Films on Rhenium Host Surfaces*

W. Kudernatsch, S. Roth, D. Rosenthal, K. Christmann, Z. Zhao, T. Diemant, B. Schumacher, R.J. Behm.

105. Bunsentagung, Erlangen, May 2006.

11. *Mechanism of the Low Temperature CO Oxidation over Metal Oxide Supported Au-Catalysts*

R. J. Behm, K. Christmann, T. Diemant, W. Kudernatsch, D. Rosenthal, R. Schlögl, S.L.M. Schröder, B. Schumacher and Z. Zhao.

105. Bunsentagung, Erlangen, May 2006.

12. *Structural and Chemical Analysis of Epitactic Rutile $TiO_2(011)$ Films Grown on $Re(10\bar{1}0)$*

W. Kudernatsch, D. Rosenthal and K. Christmann.

Verhandlungen der DPG, Dresden, March 2006.

13. *Growth of titanium oxides on metals - rutile(011) on rhenium($10\bar{1}0$)*

D. Rosenthal, W. Kudernatsch and K. Christmann.

23rd European Conference on Surface Science, Berlin, September 2005.

14. *Das Wachstum von Titanoxid auf einer $Re(10\bar{1}0)$ und einer $Ru(0001)$ Oberfläche*

D. Rosenthal, W. Kudernatsch, K. Christmann, H. Hoster, H. Rauscher und R.J. Behm.

Verhandlungen der DPG, Berlin, March 2005.